

Characterization and Modelling of the Emission Zone and Exciton Dynamics in Doped Organic Light-Emitting Diodes

Thèse N° 9697

Présentée le 20 septembre 2019

à la Faculté des sciences et techniques de l'ingénieur
Unité de rattachement pour scientifiques IMX
Programme doctoral en science et génie des matériaux

pour l'obtention du grade de Docteur ès Sciences

par

Markus REGNAT

Acceptée sur proposition du jury

Prof. C. Ludwig, président du jury
Prof. F. Nüesch, Prof. B. Ruhstaller, directeurs de thèse
Prof. S. Reineke, rapporteur
Dr C. Pflumm, rapporteur
Prof. M. K. Nazeeruddin, rapporteur

2019

Für meine Eltern ...
Für Natalia & Lisa ...

"Logik bringt dich von A nach B.
Deine Phantasie bringt dich überall hin."
— Albert Einstein

Acknowledgements

First of all I would like to thank my EPFL PhD supervisor Frank for his continuous support and interest in my work as well as for the inspiring exchange of ideas during this time.

Next I would like to express my sincere gratitude to Beat, who hired me in the first place at ZHAW and then supported, encouraged and trusted me for doing this PhD, as well as gave me the chance to present my results at several international conferences.

I also want to extend special thanks to Kurt for his guidance, and knowledge as well as frequent discussions and helpful suggestions which helped me to look at my research from a different perspective. His perfectionism encouraged me to go deeper into details and refine my scientific work practice.

I also want to thank all former and current colleagues at the ICP group at ZHAW and the Fluxim team for their support and contribution to my thesis: First, Jonas and Tilman for the collaborative and enjoyable atmosphere in our office and laboratory and their expertise with Matlab and OLED manufacturing. Second Simon and Sandra for their help and advice in setting up my measurement routines and Kurt for his support with Matlab code writing. Thanks also to Martin and Adrian for their support with Paios, to Stéphan, Lieven and Balthasar for the frequent discussions about the physics behind Setfos, to Sascha, Lidia and Oliver for including my extra wishes in the Setfos code and finally again to Simon, for his expertise and support with LaTeX.

Further I would like to thank Uros, Mojca, Marcin, Evelyne, Christoph and Kurt for fruitful scientific and non-scientific discussions during lunch time, tea/coffee breaks or at the weekly “Feierabendbier”, Alexandra for the help with administrative tasks and again Beat for the several invitations to social Fluxim events.

Ein ganz besonderer Dank geht an meine Eltern die mir es ermöglicht haben zu studieren und mich dabei von Anfang an so gut sie konnten unterstützt und gefördert haben und an meinen Bruder Stefan für das Korrekturlesen.

Para finalizar, el mayor de mis agradecimientos para mi mujer Natalia, que durante todo este tiempo ha estado a mi lado acompañándome en mis altibajos, posponiendo en muchas ocasiones importantes sus propios intereses para ayudarme y contribuyendo así considerablemente al éxito de esta tesis doctoral. Y para mi hija Lisa la alegría de nuestras vidas.

Elsau, 26.05.2019

Markus Regnat

Abstract

Only recently organic light-emitting diode (OLED) technology has successfully managed the transition from research labs into the consumer market, taking a 60% share of the global mobile display market in 2018. The latest discovery of thermally activated delayed fluorescence attracted a lot of attention in research and industry due to the potential to fabricate fluorescence-based OLEDs with high efficiencies comparable to the currently used phosphorescence-based OLEDs, but with the advantage of possibly cheaper and more sustainable emitter materials (no Ir-, Pt-complexes).

For achieving high efficiencies in OLEDs, a substantial number of layers and interfaces of the multilayer stack have to be optimized. A particularly important role is assigned to the emission layer within which light is generated by charge recombination and subsequent energy transfer and radiative decay of excitons. The understanding of charge recombination and exciton dynamics and the determination of the position of light generation are essential for the fabrication of modern OLEDs and are the goal of this thesis. Therefore two different OLED types, phosphorescence-based OLEDs and state-of-the-art TADF exciplex host OLEDs incorporating a fluorescent emitter, are studied by electro-optical characterization and device modelling.

In a first step the emission zones are determined and analyzed by angle-dependent steady-state measurements at different biases and optical simulations. In both OLED types split emission zones are obtained with densities of emissive excitons that decay away from both emission layer interfaces toward the center. For the phosphorescence-based OLEDs an additional bias-dependence of the split emission zone is observed, meaning that at low bias the main emission is located at the cathode side and shifts to the anode side for increasing bias. In a second step, with transient EL decay measurements and electro-optical simulations the split emission zones are correlated to an EL peak appearing after OLED turn-off. To study the influence of the emission zone and the exciton dynamics on the OLED efficiency an electro-optical device model is established to reproduce the experimentally obtained measurement data. As the model includes charge carrier dynamics, light outcoupling and time- and position-dependent exciton processes, such as the formation, diffusion, transfer, decay and quenching, the physical mechanisms in the OLEDs are elucidated. For the phosphorescence-based OLED a surprising current efficiency increase of up to 60% for increasing bias as well as a subsequent decrease is explained with the shift of the emission zone and its influence on exciton quenching and light outcoupling. Similarly, for the TADF exciplex host OLEDs a model parameter study illustrates promising EQE enhancement routes, which could lead to

Abstract

EQEs as high as 42%.

This thesis emphasizes the need of accurate knowledge of the emission zone and its bias-dependence due to its potentially strong influence on the OLED efficiency and its importance for the optimization of the OLED layer stack. In addition, this thesis shows that full electro-optical device modelling (including electrons, excitons and photons) combined with advanced electro-optical characterization techniques is crucial for elucidating the physical mechanisms in state-of-the-art OLEDs as well as for the prediction of promising routes for future efficiency enhancements.

Kurzbeschreibung

Erst in jüngster Zeit hat die organische Leuchtdioden (OLED) Technologie den Übergang von den Forschungslaboren in den Verbrauchermarkt erfolgreich gemeistert und erreicht einen Anteil von 60% am weltweiten Handy-Displaymarkt im Jahr 2018. Die aktuelle Entdeckung der thermisch aktivierten verzögerten Fluoreszenz (TADF) erregte in Forschung und Industrie große Aufmerksamkeit, da damit auf Fluoreszenz basierte OLEDs mit hohen Wirkungsgraden hergestellt werden können. Diese sind vergleichbar mit den derzeit verwendeten auf Phosphoreszenz basierten OLEDs, haben aber den Vorteil, dass in ihnen möglicherweise billigere und nachhaltigere Emmitter Materialien (keine Ir-, Pt-Komplexe) verbaut werden können.

Um hohe Wirkungsgrade in OLEDs zu erreichen muss eine erhebliche Anzahl von Schichten und Schnittstellen des Mehrschichtsystems einer OLED optimiert werden. Eine besonders wichtige Rolle kommt der Emissionsschicht zu, in der durch Ladungsrekombination und anschließende Energieübertragung und Strahlungsabbau von Exzitonen Licht erzeugt wird. Das Verständnis dieser Exzitonen-Dynamik und die Bestimmung der genauen Position der Lichterzeugung sind für die Herstellung hocheffizienter OLEDs unerlässlich und sind das Ziel dieser Arbeit. Dazu werden zwei verschiedene OLED-Typen - Phosphoreszenz basierte OLEDs und Fluoreszenz basierte TADF-Exciplex-Host OLEDs - durch elektro-optische Charakterisierung und Bauteilmodellierung untersucht.

In einem ersten Schritt werden dazu die Emissionszonen durch winkelabhängige Messungen bei verschiedenen angelegten Spannungen und optische Simulationen bestimmt und analysiert. Für die beiden untersuchten OLED-Typen lässt sich eine geteilte Emissionszone mit abnehmendem Emissionsprofil von beiden Seiten der Emissionsschicht zum Zentrum hin feststellen. Für die auf Phosphoreszenz basierten OLEDs ist zusätzlich eine Spannungsabhängigkeit der geteilten Emissionszone beobachtet worden, d.h. bei niedrigen Spannungen befindet sich die Hauptemission auf der Kathodenseite und verschiebt sich mit Erhöhen der Spannung auf die Anodenseite der Emissionsschicht. In einem zweiten Schritt konnten mit transienten Elektrolumineszenzmessungen und elektro-optischen Simulationen die vorher gemessenen geteilten Emissionszonen in Verbindung gebracht werden mit einem kurzzeitig auftretenden Lichtanstieg nach dem Ausschalten der OLED. Um den Einfluss der Emissionszone und der Exzitonen-Dynamik auf den OLED-Wirkungsgrad zu untersuchen ist ein elektro-optisches Bauteilmodell erstellt worden um die experimentell gewonnenen Messdaten nach zu simulieren. Da das Modell die Ladungsträgerdynamik, die Lichtauskopplung und die zeit- und positionsabhängigen Exzitonen-Prozesse wie Exzitonen-Bildung, -Diffusion, -Transfer, -Zerfall und -Auslöschung simulieren kann, konnten damit die physikalischen Mechanismen

in den untersuchten OLEDs erklärt werden. Bei den auf Phosphoreszenz basierten OLEDs konnte ein überraschender Anstieg der Lichtausbeute von bis zu 60% bei Erhöhung der angelegten Spannung zurückgeführt werden auf die Verschiebung der geteilten Emissionszone und ihrem Einfluss auf die Exzitonen Auslöschungsprozesse sowie auf die Lichtauskopplung. Bei den Fluoreszenz basierten TADF-Exciplex-Host OLEDs konnte mit einer Modellparameterstudie vielversprechende Verbesserungsmöglichkeiten aufgezeigt werden, die zusammengekommen einen Wirkungsgrad von bis zu 42% ermöglichen könnten.

Diese Arbeit betont somit die Notwendigkeit einer genauen Kenntnis der Emissionszone und deren Spannungsabhängigkeit aufgrund des potenziell starken Einflusses auf den Wirkungsgrad der OLED und ihrer Bedeutung für die Optimierung des OLED-Mehrschichtsystems. Darüber hinaus zeigt diese Arbeit, dass die vollständige elektro-optische Bauteilmodellierung (einschließlich Ladungsträgerdynamik, Exzitonen-Prozesse und Lichtauskopplung) in Kombination mit fortschrittlichen elektro-optischen Charakterisierungstechniken entscheidend für die Erklärung der physikalischen Mechanismen in OLEDs sowie zum Aufzeigen vielversprechender Wege für zukünftige Effizienzsteigerungen ist.

Contents

Acknowledgements	v
Abstract (English/Deutsch)	vii
List of figures	xi
List of tables	xiv
Aim and Structure of the Thesis	xvii
1 Introduction	1
1.1 Organic Optoelectronics	1
1.2 Organic Light-Emitting Diodes	6
1.2.1 Industrial implementation of OLEDs	6
1.2.2 Device architecture and working principle	7
1.2.3 Figures of merit	9
1.2.4 Electro-optical characterization	13
1.2.5 Exciton dynamics	16
1.3 Device Modelling	23
1.3.1 Electrical modelling of injection, drift and diffusion of charge carriers . .	23
1.3.2 Optical modelling of light outcoupling and emission zone	25
1.3.3 A comprehensive electro-optical device model	27
2 Emission Zone Analysis in Phosphorescence-based OLEDs	37
3 Emission Zone Influence on Exciton Quenching and Efficiency	55
4 Prediction of Efficiency Enhancement in TADF OLEDs	75
5 Conclusion	95
5.1 Achieved results and impact	95
5.2 Outlook	96
Curriculum Vitae	99

List of Figures

1.1	Double bond in ethene molecule	3
1.2	Chemical structures of organic semiconductor molecules	4
1.3	Spincoating and thermal evaporation	5
1.4	OLED display revenues	7
1.5	OLED stack and working principle	8
1.6	Charge carrier balance factor	10
1.7	Light outcoupling factor	11
1.8	Setup current-voltage-luminance measurement	14
1.9	Setup angle-dependent electroluminescence measurement	15
1.10	Setup transient electroluminescence measurement	16
1.11	Singlet/triplet exciton formation	17
1.12	Dexter/Förster resonance energy transfer	18
1.13	Exciton decay - Jablonski diagram	19
1.14	Schema thermally activated delayed fluorescence	20
1.15	Thermally activated delayed fluorescence in OLED devices	20
1.16	Triplet-triplet annihilation and triplet-polaron quenching	22
1.17	Schema dipole model	26
1.18	Schema s- and p-polarization	27
1.19	Schema comprehensive device model	28
2.1	OLED layer stack	39
2.2	Angle-dependent electroluminescence spectra and emission zone	40
2.3	Transient electroluminescence peak after turn-off the OLED	41
2.4	Simulated ideal OLED stack	43
2.5	Split emission zone and transient electroluminescence turn-off peak	44
2.6	Simulated mobility, split emission zone, electroluminescence peak	45
2.7	Simulated split emission zone, electroluminescence peak and TTA	46
S2.1	Angle-dependent electroluminescence spectra for low and high currents	53
S2.2	Simulated electroluminescence peak, split emission zone with TPQ	53
3.1	Measured and simulated IVL and current efficiency	59
3.2	Influence light outcoupling factor on generated photons	60
3.3	Contributions exciton continuity equation for increasing bias	61

List of Figures

3.4	Relative contributions exciton continuity equation for increasing bias	62
3.5	Exciton and charge carrier distribution for low and high bias	63
3.6	Influence purcell factor on generated photons	64
3.7	Measured and simulated transient electroluminescence decay	65
3.8	Electroluminescence decay contribution	66
S3.1	Mode analysis for increasing bias	72
4.1	TADF OLED stack	77
4.2	Schema exciton processes in TADF OLED	79
4.3	Measured and simulated IVL and current efficiency	80
4.4	Measured and simulated angle-dependent electroluminescence spectra	81
4.5	Split emission zone and purcell factor	81
4.6	Transient electroluminescence decay of aged and IV of fresh and aged OLED .	82
4.7	Emission zone analysis	83
4.8	Prediction of OLED efficiency enhancement	84
S4.1	Refractive index and extinction coefficient data	90
S4.2	Absorbance and photoluminescence spectra of host and guest	91
S4.3	Angle-dependent electroluminescence spectra and emission zone at high bias	91
S4.4	Host exciplex and guest exciton density in emitting layer	93
S4.5	Prediction of OLED efficiency for best case scenario	93

List of Tables

S3.1 Model parameters of electro-optical simulations	73
S4.1 Mobility parameters used in the electro-optical model	94

Aim and Structure of the Thesis

Highly efficient phosphorescence-based OLEDs can be found in most current displays of mobile phones, televisions and smart watches. Current research tries to replace these highly efficient phosphorescence-based OLEDs with fluorescence-based OLEDs because of their higher color purity and operational stability, as well as less expensive emitter materials. This was not possible for a long time due to the lower quantum yield of fluorescence-based OLEDs. However, the recent discovery of thermally activated delayed fluorescence (TADF) made it possible to realize fluorescence-based OLEDs with similarly high efficiencies as phosphorescence-based OLEDs. The full potential of TADF has not yet been exploited. Decisive for achieving highly efficient OLED devices is the knowledge of the position and profile of the emission zone and a good understanding of the exciton dynamics in the OLED.

The aim of this thesis is to investigate the emission zone and exciton dynamics in phosphorescent and TADF OLEDs with advanced electro-optical characterization techniques in combination with optical simulations. The result is a comprehensive OLED device model that can reproduce the electro-optical characteristics of a state-of-the-art TADF OLED, and thus allows to identify the most promising routes for further efficiency enhancements through a model parameter study.

Chapter 2 is a study, which determines the emission zone (EMZ) profiles and position on in-house fabricated phosphorescence-based OLEDs are determined for different bias. For the EMZ determination a homemade angle-dependent electroluminescence (EL) spectra measurement setup and optical simulations are used, which reveals a bias-dependent split emission zone. Through additional transient EL measurements an appearing EL peak after turn-off the OLED with a negative bias could be identified as a hallmark of the split emission zone. A qualitative electro-optical model is used to verify the experimental data.

In chapter 3, a second study is presented, where the qualitative model in chapter 2 is improved to a quantitative device model including exciton quenching processes. With an optimization algorithm a model parameter set is found, that could reproduce the current-voltage-luminance characteristics, the bias-dependent split emission zone and the transient EL decay data, as well as the current efficiency behavior for increasing current density of the investigated phosphorescence-based OLEDs in chapter 2. With the device model the exciton dynamics could be elucidated and the surprising measured rise of the current efficiency for increasing bias and the following decrease could be explained by the emission zone change, causing a reduction of the triplet-polaron quenching and light outcoupling efficiency, and the triplet-triplet annihilation.

A third study in chapter 4 investigates state-of-the-art TADF OLEDs from our Korean project partner. These TADF OLEDs consists of an exciplex host doped with a fluorescent emitter and show EQEs of $> 10\%$ at low bias. For accurate simulation of the triplet harvesting process on this exciplex host the electro-optical model was extended to include the exciplex dynamics of the host singlet and triplet states in addition to the exciton dynamics of the guest singlet state. With the exciplex parameters provided by the Korean project partner, the comprehensive model could reproduce the measured current-voltage-luminance, current efficiency and angle-dependent EL spectra data for optically tuned and optically detuned OLED stacks. Interestingly a split emission zone is also observed in these state-of-the-art OLED devices. Furthermore the model reveals the TADF contribution to the EQE for increasing bias and shows that the triplet harvesting is only high at low bias and rapidly decreases with increasing bias. Finally, with a model parameter study promising routes are predicted for efficiency enhancements, which, if realized, would lead to OLEDs with EQEs of up to 42%.

1 Introduction

This chapter is intended to provide an overview on different aspects of organic light-emitting diodes (OLEDs). While the first section introduces historical milestones, suitable semiconductor materials and processing techniques for organic optoelectronics in general, the second section focuses on OLEDs, including the chronology of the industrial implementation, the device architecture, the working principle, different characterization methods and important figures of merit. Due to the importance of exciton dynamics for the understanding of OLEDs and the device modelling, a separate subsection is added to discuss in detail exciton formation, decay, transfer and quenching. In the third and last section, OLED device modelling is then introduced, starting with a description of the basics for numerical and optical modelling, followed by the introduction of the comprehensive electro-optical device model employed in this work.

Details on the investigated OLEDs in this work can be found in the individual introduction and experimental sections of the following chapters and thus are not described in this chapter.

1.1 Organic Optoelectronics

Since the beginning of the 21st century organic optoelectronics receives considerable attention from research and industry. This is due to their promise as low cost and high throughput technology with a wide range of application such as flexible devices. The recent commercialization of organic light-emitting diodes (OLEDs) taking a market share of 60% in 2018 for mobile phone displays indeed underlines this successful technological implementation. This rise of organic optoelectronics becomes possible due to the discovery and understanding of a new class of materials, called organic semiconductors. First reports on organic semiconductor dates back to the 1910s, where studies with anthracene crystals on photoconductivity were reported¹⁻⁴. Several tens of years later in 1953 organic materials based electroluminescence was reported for the first time on a cellulose film doped with acridine orange by Bernanose⁵ and in the 1960s electroluminescence in anthracene crystals was reported by Pope et al. and others^{6,7}. Further important achievements were the successful syntheses and the theory of

highly conductive organic semiconductor polymers in the 1970s by Alan J. Heeger, Alan G. MacDiarmid and Hideki Shirakawa^{8,9}, which was rewarded with the nobel prize in 2000. Further milestones were the first demonstration of efficient organic photovoltaic cells¹⁰ and thin-film transistors¹¹ in the 1980s. Also in the late 1980s the first OLED devices with an efficiency of about 1% by Tang and VanSlyke¹² and later by Burroughes et al.¹³ were fabricated. In the late 1990s then the use of organometallic complexes allowing phosphorescence in organic semiconductors led to four times higher device efficiencies compared to the fluorescence-based OLED counterparts¹⁴. All these discoveries together paved the way for today's commercial optoelectronics revolution based on organic semiconductors and its huge variety of chemical structures.

Organic semiconductors consist mainly of carbon and hydrogen atoms, where the essential part for semiconductor characteristics lies in the formation of alternating double single carbon-carbon bonds throughout the molecule. In **Figure 1.1a** the electronic configuration for a carbon-carbon double bond is shown taking the example of the ethene molecule. A carbon atom has four valence electrons, where two electrons of them occupy the 2s orbital and the other two electrons occupy the 2p orbitals. In an ethene molecule each carbon atom has three bonding partners (two hydrogen atoms and one carbon atom), such that simple valence bond theory predicts each carbon atom to form three equivalent sp^2 hybridized orbitals, which are lying all in one plane, separated by an angle of 120° . Two of these hybrid orbitals of the neighboring carbon atoms overlap and form the sigma (σ) bond. The remaining 2p-orbital of each carbon atom is orientated perpendicular to sp^2 -hybridized orbital plane and due to the overlap between the former, a second, energetically weaker carbon-carbon pi (π) bond, additional to the carbon-carbon σ bond from the sp -hybridized orbitals, is formed as illustrated in Figure 1.1b.

In Figure 1.1c the electrons of the initially involved carbon atomic orbitals (AO) and the resulting molecular orbitals (MO) of the ethene molecule are shown. The energy levels can be calculated with the Hückel molecular orbital theory to a certain accuracy, where a linear combination of atomic orbitals approximation is used. Detailed description can be found in textbooks from A. Köhler and H. Bässler¹⁵, M. Schwörer and H. C. Wolf¹⁶ and M. Pope and C. E. Swenberg¹⁷. Due to constructive and destructive interference of the electron wavefunctions of the involved atomic orbitals for the σ and π bond an energetically low bonding and energetically high antibonding (*) character is formed. Due to less overlap of the p_z -orbitals the π bond is weaker compared to the σ bond and therefore the energy splitting in the molecular orbitals for the π bond is less pronounced. Filling up the molecular orbitals with the involved electrons from the atomic orbitals results that the π orbital is the highest occupied molecular orbital (HOMO) and the π^* orbital is the lowest unoccupied molecular orbital (LUMO). These HOMO and LUMO orbitals are often called frontier orbitals, and their energy levels are specific for each organic semiconductor molecule and play an important role in the optical and electrical processes of the molecule. In organic semiconductors molecules in general these frontier orbitals are the π - and π^* orbitals, which show an energy splitting of about 2.5 ± 0.5 eV and thus light absorption or light emission occurs in the visible spectral range (380

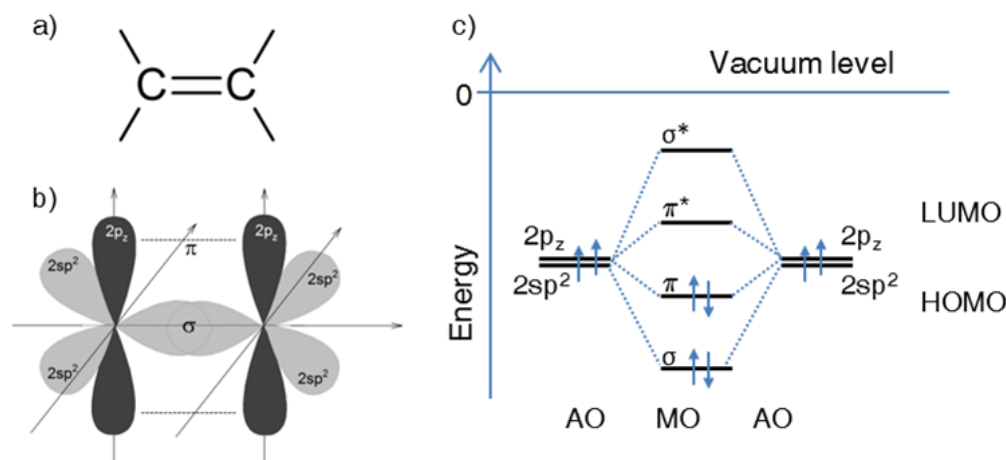


Figure 1.1 – Chemical structure of the ethene molecule (a). Schematic illustration of the atomic orbitals involved in forming a carbon-carbon double bond shown on the example of ethene (b). Energy level diagram showing the molecular orbitals (MO) formed from the involved atomic orbitals (AO) for the carbon-carbon double bond (c). The highest occupied molecular orbital (HOMO) is the π orbital and the lowest unoccupied molecular orbital (LUMO) is the π^* orbital. Figure adapted from reference¹⁵

– 740 nm) which is well suited for optoelectronics. Furthermore with typical HOMO (LUMO) energy levels of about -5 (-2) eV good hole (electron) injection to the HOMO (LUMO) from standard electrode materials, such as indium tin oxide (-4.8 eV) or calcium (-2.8 eV) is possible. For these reasons, organic semiconductor molecules are ideal candidates for applications in optoelectronic devices, such as OPVs, OFETS and OLEDs, but also in organic light emitting electrochemical cells (OLECS) or organic photodetectors.

Typically two classes of these organic semiconductor molecules are defined, the low molecular-weight molecules with well defined structures and a fixed number of atoms, called small molecules and macromolecules with a large chain of repeating structural units and an average high molecular-weight, called polymers¹⁸. As examples in **Figure 1.2** all organic semiconductor molecules used in the investigated OLEDs in this work are shown. Figure 1.2a shows the chemical structures of the doped conductive polymer poly(3,4-ethylenedioxythiophene)-poly(styrenesulfonate) (PEDOT:PSS) which is an often used semitransparent and high conductive electrode planarization and hole injection layer on top of the indium tin oxide anode. All other shown organic semiconductors belong to the class of small molecules, where Figure 1.2b and c are tris(4-carbazoyl-9-ylphenyl)amine (TCTA) and 4,4'-cyclohexylidenebis[N,N-bis(4-methylphenyl)benzenamine] (TAPC) and often used hole transport materials, Figure 1.2d and e are 4,6-bis[3,5-(dipyrid-4-yl)phenyl]-2-methylpyridine (B4PYMPM) and 4,6-bis[3,5-(dipyrid-4-yl)phenyl]-2-methylpyridine (NBPhen) and often used electron transport materials. Figure 1.2f 4,4'-bis(N-carbazoyl)-1,1'-biphenyl (CBP) is an often used host

coating techniques are the easy and low-cost processing and the possibility of large area processing. The disadvantages are that for multilayers orthogonal solvents have to be found in order not to dissolve the underlying layer. Furthermore lateral structuring of the polymer film is difficult and relies on lithographic or laser ablation techniques. To circumvent the latter shortcomings, inkjet printing technique could be used²¹.

Figure 1.3b shows the schematic process of the deposition of small molecules through thermal vacuum-evaporation. Typically the small molecules can be bought in form of powders (highest possible purity grade), which then can be filled in crucibles and mount into evaporation source units. The substrates are fixed on a substrate holder on top of the crucibles. Under high-vacuum ($\approx 10^{-6}$ mbar) the evaporation sources are heated through electrical resistance and the small molecules start to evaporate and thus form a film on the substrate. Through rotation of the substrate inhomogeneities on the surface are smoothed. The rate of deposition can be controlled by the temperature of the crucibles and the thickness of the deposited film is measured using quartz crystal sensors. The advantages of the thermal vacuum-evaporation is the possibility of structuring the film through shadow masks and the straight forward fabrication of multilayer and co-evaporated films through evaporation of different materials in sequence or at once. The biggest disadvantages are the relatively high cost of vacuum deposition and the limitation of the substrate to the size of the vacuum chamber. The vacuum deposition technique, however, is still compatible with roll-to-roll coating as has been demonstrated by Fraunhofer institute (FEP)²².

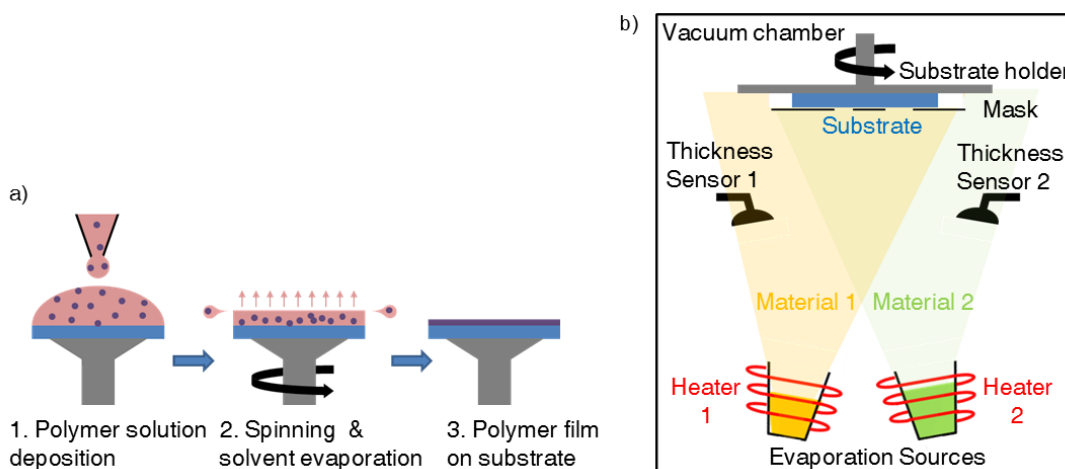


Figure 1.3 – Schematic illustration of the three-step spin coating process for polymer deposition (a) and the small molecule deposition process through thermal vacuum-evaporation (b).

1.2 Organic Light-Emitting Diodes

In this section the fundamental aspects of an OLED are discussed, starting with an OLED chronology from the first observation of electroluminescence nearly seventy years ago to the industrial implementation to the today's multi-billion dollar market. This is followed by a basic description of the OLED device architecture and its working principle, before characterization techniques and figure of merits are introduced. At the end the exciton dynamics that can take place in an OLED are discussed.

1.2.1 Industrial implementation of OLEDs

Despite the discovery of electroluminescence on a cellulose film doped with acridine orange in the year 1953 by Bernanose⁵, where high voltages of about 400 V were necessary to observe light emission, it took more than 30 years until Tang and Vanslyke¹² at Eastman Kodak in 1987 reported an OLED device with an efficiency of 1%, a brightness of $> 1000 \text{ cd/m}^2$ and a driving voltage below 10 V. This was achieved by the fabrication of a double-layer structure with ultrathin-films fabricated from evaporated small molecules, resulting in an efficient light generation at the bilayer interface. In the year 1990 followed the first polymer OLED device reported by Burroughes et al.¹³, leading to the first commercial polymer OLED Displays by Pioneer and Cambridge Display Technology in the year 1996²³. Two years later in the year 1998 Baldo et al.¹⁴ reported for the first time a phosphorescence-based OLED with a platinum organometal-complex as phosphorescent dye and up to that time unprecedented efficiency of 4% and thus paved the way for the industrial mass production of OLEDs. Further innovations, such as the introduction of electrical doped transport layers²⁴ or the utilization of iridium complexes as phosphorescent dyes²⁵ led to a drastically reduced OLED operating voltages and strongly increased OLED efficiencies close to 30% and thus greatly helped the rapid and successful commercialization of OLEDs. In 2003 the first commercial mobile phone using an OLED display was unveiled by Sanyo. In 2007 the first commercial OLED TV XEL-1 with a 11inch OLED display from Sony starts to sale in Japan. In 2008 OLED display is used in Nokia's N85 mobile phone, yielding brighter and sharper colours. Nowadays most mobile phones are using OLED displays²⁶. In 2019 the OLED display revenue market is expected to reach 31 billion \$ and until 2022 grow up close to 49 billion \$ and thus more than triples the value of the year 2016, as shown in **Figure 1.4**. The main OLED displays revenues were, are and will be in the near future for mobile phones, followed by OLED displays for television and smart watches. Even though first products for OLED lighting applications are nowadays available on the market, the prices are high and the variety is very low. With the continuing rapid development, such as seen on the latest announcement by LG, with the launch of a rollable large area OLED TV or the latest announcements by Samsung and Huawei, launching the foldable mobile phones, it is only a matter of time until we will see commercial products for large area lighting applications.

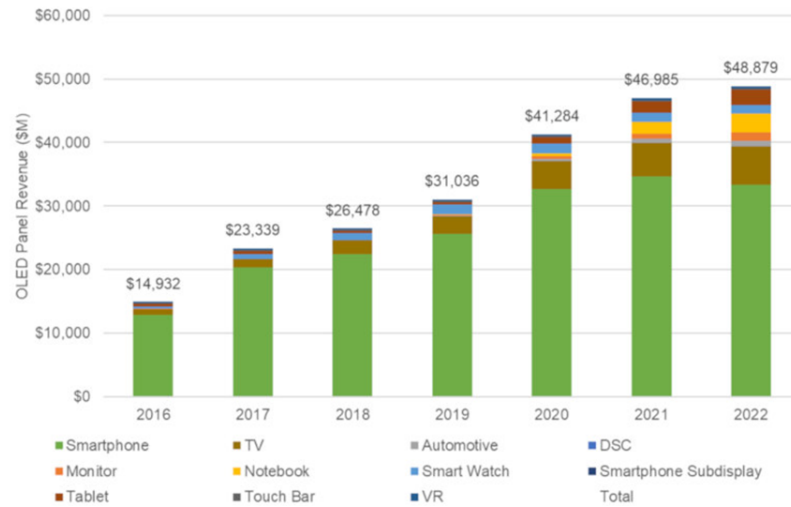


Figure 1.4 – Overview of OLED display revenues from 2016 to now and forecast up to the year 2022, where revenues could reach close to 49 billion \$ and thus more than triples the value from 2016. Main OLED displays revenues were, are and will be in the near future for mobile phones (green bars) followed by television (brown bars). Graphic taken from²⁷

1.2.2 Device architecture and working principle

In order to build a functioning OLED device at least one organic layer between two electrodes is required, whereby one electrode must be semitransparent for light outcoupling. Usually several organic layers are used in today's OLED devices, where each individual layer can be tuned in its functional properties through appropriate materials. A typical OLED stack for bottom emission is shown in **Figure 1.5a** where the organic part consists of three individual layers for hole transport (HTL), emission (EML) and electron transport (ETL). The emission layer is mainly doped with a fluorescent or phosphorescent emitter material to improve the OLED efficiency (differences between fluorescence and phosphorescence and its influence on the efficiency is discussed in subsection 1.2.5).

In more advanced OLED device architectures, electrical doping of the HTL and ETL are used for improved charge carrier injection and transport and additional hole (electron) blocking layers between the emission layer and ETL (HTL) are introduced to confine the charge carriers in the emission layer, both leading to improved efficiencies and higher OLED stabilities²⁸.

Another recently reported advanced device architecture concept showing high EQEs, uses instead of a single host material, co-evaporated HTL and ETL materials, resulting in much simpler device architectures with high charge carrier confinement and low internal energy barriers. Kim et al.²⁹ reported OLEDs with such device architecture, showing low operating voltages and very high efficiencies of more than 30% EQE for phosphorescence-based OLEDs. In chapter 4, an OLED having this exciplex host, but with a fluorescent dye is investigated.

The substrate in an OLED device is often glass, but for flexible applications polymer or metal foils can be used, too. On a glass substrate mostly the semitransparent anode indium tin oxide (ITO)³⁰ is used, which has a high transparency in the visible light range of $85\pm 5\%$ and a low electrical resistance ($\approx 20 \Omega/\square$). On top of the ITO often a thin film of PEDOT:PSS¹⁹ (cf. Figure 1.2) is spin coated for reduced surface roughness and increased work function (≈ -4.8 to -5.2 eV) for an improved hole injection to the HTL.

On the other side, on top of the organic layers, highly, for the cathode highly reflective metals such as aluminium or silver are used for the cathode, combined with low work function metals such as calcium (≈ -2.8 eV). This provides are used for good high light reflection and good excellent electron injection into the ETL.

Since many of this low work function metals and also the organic materials react with oxygen and moisture the OLED under operation would rapidly degrade³¹ if the device architecture is not encapsulated. The encapsulation is often done with an additional glass plate on top and glued to the bottom glass substrate under inert atmosphere. Furthermore often a getter material is added to absorb small amounts of oxygen or water that penetrate with time through the encapsulation.

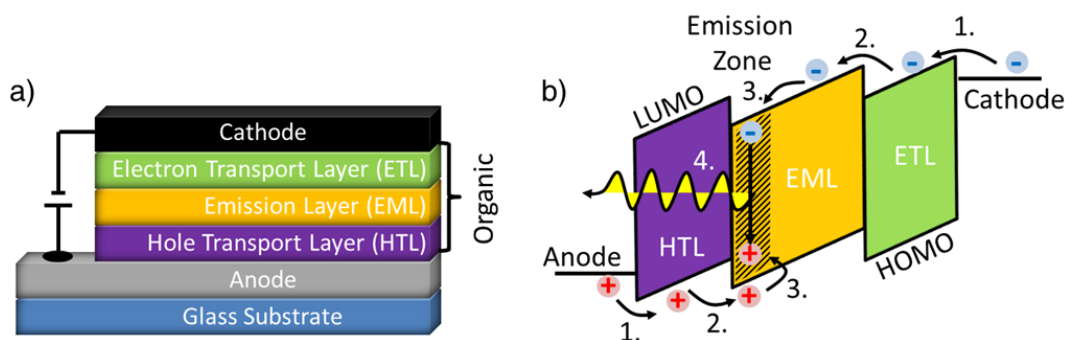


Figure 1.5 – Typical device architecture for a bottom emitting OLED, where the anode must be semitransparent for light outcoupling (a) and schematic illustration of the OLED working principle under operation (b) described in four steps: Charge carrier injection, charge carrier transport through organic layers, electron-hole pair/exciton formation and radiative recombination of the exciton and light emission through the semitransparent anode and glass substrate.

In Figure 1.5b the working principle of light emission in an OLED is shown for an applied bias, which is high enough to drive the device. The mechanism can be described in four steps³²:

1. Injection of charge carriers: If the applied voltage at the electrodes is high enough the holes from the anode and the electrons from the cathode can overcome the metal/organic energy barrier and get injected in the HOMO of the HTL and in the LUMO of the ETL, respectively.

2. Transport of charge carriers through the organic: Through the applied voltage at the electrodes an electrical field is generated in the OLED, which causes the injected holes in the HOMO to drift to the cathode and the injected electrons in the LUMO to drift to the anode. The transport for holes and electrons in the OLED can differ strongly, depending on the hole and electron mobilities in the individual layers, the layer thicknesses, as well as internal energy barriers inbetween the layers.
3. Electron-hole pair/exciton formation: If an electron in the LUMO and a hole in the HOMO are in close proximity, they form an electron-hole pair due to their coulombic attraction. This formed electron-hole pair is also called exciton and its intrinsic lifetime depends on the material and the spin state (see additional information in subsection 1.2.5).
4. Radiative recombination of exciton and light emission: In the lifetime of an exciton, different exciton dynamics can take place in an OLED (see subsection 1.2.5), one of these exciton processes is the radiative recombination, where the electron in the LUMO recombines with the hole in the HOMO and releases energy in form of a photon. The spatial location of the radiative recombination in the emission layer is often called emission zone (as depicted in Figure 1.5b). Under certain outcoupling conditions this photon from the emission zone can now exit the OLED stack through the transparent electrode and light emission can be observed. The colour of the emitted light depends on the HOMO-LUMO energy difference and thus can be tuned by appropriate emitter materials.

Detailed description of possible loss mechanisms causing no light emission in an OLED under operation is given with the introduction of the external quantum efficiency in the next subsection.

1.2.3 Figures of merit

The figures of merit of an OLED give information of how good an OLED device is functioning in regard of efficiency, brightness, energy consumption and operational lifetime.

External quantum efficiency

The most important key figure is the external quantum efficiency (EQE), which gives the ratio between the number of emitted photons and the number of injected charge carriers and thus describes how efficient the OLED converts electrons to photons. The EQE can be written as a product of four factors^{32,33}:

$$EQE = \gamma \cdot \eta_{S/T} \cdot \eta_{eff} \cdot \eta_{Out} \quad (1.1)$$

Chapter 1. Introduction

First factor γ is the charge carrier balance factor and gives the ratio of electrons and holes that recombine and form excitons (recombination current J_{rec}) to the total injected electrons and holes (total current J), illustrated in **Figure 1.6**. By introducing electron and hole blocking layers in the device stack (as mentioned above in subsection 1.2.2) the leakage currents caused by electrons reaching the anode or by holes reaching the cathode can be reduced close to zero and thus achieving a charge balance factor close to unity²⁸.

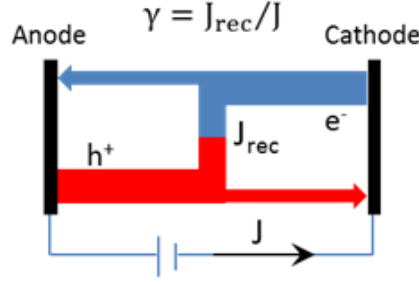


Figure 1.6 – Visulation of the charge carrier balance factor γ , which gives the ratio of the recombined electrons and holes (J_{rec}) to the total injected electrons and holes (J). Adapted from Tsutsui³³

The second factor $\eta_{S/T}$ is the singlet/triplet factor and describes the amount of how many of the generated excitons can radiatively recombine. Under electrical operation spin statistics (see section 1.1) shows that the probability of forming a triplet exciton is three times higher than forming a singlet exciton. Depending on the emitter molecule in the OLED, fluorescent or phosphorescent (details in 1.2.5), only radiative recombination for singlets (fluorescence) is allowed yielding $\eta_{S/T} = 25\%$, or radiative recombination for both triplets and singlets is allowed yielding $\eta_{S/T} = 100\%$ ³⁴. Recently with the discovery of TADF (details in 1.2.5) also OLEDs with only fluorescent emitter can achieve $\eta_{S/T} = 100\%$, due to reverse intersystem crossing of triplets to singlet states^{35–37}.

The third factor q_{eff} is the effective radiative quantum efficiency and gives the ratio of the effective radiatively recombining excitons and the the total number of formed excitons and can be derived from the intrinsic quantum efficiency q :

$$q = \frac{k_{rad}}{k_{rad} + k_{nr}} \quad (1.2)$$

where k_{rad} and k_{nr} are the intrinsic, material specific, radiative and non-radiative decay rates of the emitter, which can be determined from photoluminescence quantum efficiency measurements on the emission layer film only. In an OLED device, an optical micro-cavity is present and therefore the radiative decay rate is modified by the optical environment (mainly the distance to the reflective cathode) as following:

$$k_{rad} \rightarrow F \cdot k_{rad}, \quad (1.3)$$

where F is the Purcell factor^{38,39}. The non-radiative decay rate is not affected by the Purcell effect and thus the effective radiative quantum efficiency can be written as:

$$q_{eff} = \frac{F \cdot k_{rad}}{F \cdot k_{rad} + k_{nr}} \quad (1.4)$$

Depending on the device architecture and the position of the emission zone in the OLED the Purcell factor can increase or decrease the radiative decay rate and consequently the effective radiative quantum efficiency. To be noted here, exciton quenching processes, such as triplet-triplet annihilation or triplet-polaron quenching (described in subsection 1.2.5), are non-radiative decay processes and so they can significantly reduce the effective radiative quantum efficiency and thus the EQE of an OLED.

The product of the first three factors ($\gamma, \eta_{S/T}, q_{eff}$) is defined as the internal quantum efficiency (IQE), which can be close to 100% as shown by Adachi and co-workers³⁴.

The fourth factor η_{Out} is the light outcoupling efficiency, which gives the fraction of emitted light out of the OLED stack to the generated light inside the OLED stack. Often this factor is only roughly estimated with following equation^{40,41}:

$$\eta_{Out} = \frac{1}{2n^2} \quad (1.5)$$

where n is the refractive index of the organic materials (1.6 – 1.8). The resulting outcoupling efficiencies of 15 – 20% are quite low. The reason is the total internal reflection caused by the high refractive index of the organic (1.6 – 1.8) compared to lower refractive indices for the substrate (1.5) and ambient air, as shown in **Figure 1.7**. Using a more advanced approach called mode analysis, the light can be assigned to different modes (outcoupled, substrate, waveguided or evanescent modes) is discussed in more detail in subsection 1.3.3 with the introduction of the optical device model. With external attached micro-lens arrays on the substrate, external or internal scattering layers or refractive index engineering, are some common light extracting techniques for increasing the outcoupling efficiency and thus the OLED EQE⁴¹.

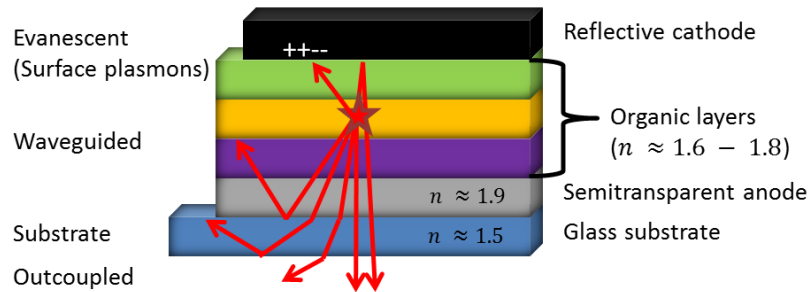


Figure 1.7 – Schematic illustration of outcoupled and trapped light in the OLED.

Luminance

Luminance is a photometric measure of how bright an OLED looks under a certain viewing angle (θ) under consideration of the colour sensitivity of the human eye and thus is another important key figure of an OLED. The luminance $L(\theta)$ can be calculated from the measured angle-dependent spectral light intensity $E(\lambda, \theta)$:

$$L(\theta) = 683 \text{ lm/W} \int_{380 \text{ nm}}^{740 \text{ nm}} V(\lambda) \cdot E(\lambda, \theta) d\lambda \quad (1.6)$$

where $V(\lambda)$ is the photopic human eye sensitivity function and 683 lm/W is the photopic constant representing the maximum of the luminous efficacy for an emitter with a wavelength of 555 nm ⁴². The SI unit of the luminance is cd/m^2 , often also the unit nits ($10 \text{ nits} = 10 \text{ cd/m}^2$) is found.

Current efficiency

The current efficiency CE is defined as the ratio of the luminance L and the applied device current density j :

$$CE = \frac{L}{j}. \quad (1.7)$$

The CE, thus, shows how bright the OLED looks for a human eye under a certain viewing angle and under a certain working point. The current efficiency has the unit cd/A and is often found in literature as a key figure for the OLED efficiency.

Luminous efficacy

The luminous efficacy (often also called power conversion efficiency) is another OLED efficiency key figure calculated from the photopic measure luminous flux ϕ_L and the electrical driving conditions, as following³²:

$$\eta_L = \frac{\phi_L}{V \cdot I} \quad (1.8)$$

where V is the applied voltage and I is the current flowing through the OLED. Therefore the luminous efficacy with the unit lm/W expresses how much light (weighted by the human eye sensitivity) the OLED emits per electrical power consumed. Thus this is an important key figure for OLED displays. To have low power consumption, OLEDs with low turn-on voltages are desired.

Operational lifetime

The operational lifetime of an OLED is given often as LT_{95} in hours, where the subscript number (here 95) expresses the percentage of the initial luminance after the number of hours.

Best OLED devices with red and green emitter achieve several 10 000 hours LT₉₅, bottle neck is still the blue emitter, with only several 100 h LT₉₅⁴³.

The figures of merit of the investigated state-of-the-art TADF OLED in this work (see chapter 4) are as follows: At a low bias < 2.4 V, EQEs > 10% with luminance values < 10 cd/m² were obtained. The current efficiency at 2.4 V was 22 cd/A. The luminous efficacy and the lifetime were not determined in this work.

1.2.4 Electro-optical characterization

Electro-optical characterization is needed to determine the above figure of merits and to elucidate the physical mechanisms in an OLED from measurements. The characterization can be done in different operation regimes, such as steady-state or transient, allowing to target different physical mechanisms in the OLED. In the following, only those measurement setups and characterization techniques used in this thesis are presented.

Current – Voltage – Luminance

A basic and very often used characterization technique for OLEDs is the current – voltage – luminance (I-V-L) measurement, where the applied voltage is swept and the current and luminance (more precisely the photodetector voltage) values are measured. Knowing the distance of the used photodetector⁴⁴ to the OLED, as well as the spectral sensitivity and geometry of the photodetector the luminance can be calculated⁴⁵:

$$L = \frac{f_{V-lm}}{\Omega \cdot f_{amp}} \cdot \frac{1}{A_{OLED}} \cdot V_{PD} \quad (1.9)$$

where f_{V-lm} is the voltage-to-lumen conversion factor for the photodetector, which depends on the detector sensitivity and the emission spectrum. Ω is the solid angle with $\Omega = \frac{A_{PD}}{r^2}$ (OLED is approximated as point source), where A_{PD} is the detector area and r is the distance from the OLED to the photodetector. Due to a possible amplification of the photodetector (0 dB – 60 dB range) an amplification factor f_{amp} for the luminance calculation is needed with $f_{amp} = 10^{\frac{PD_{amp}}{20}}$, where PD_{amp} reveals the amplification in dB. A_{OLED} is the OLED pixel size in m² and V_{PD} is the measured photodetector voltage. In **Figure 1.8** the used measurement setup and typical I-V-L curves are shown.

For the voltage source and the current measurement, as well as for the photodetector voltage measurement, the all-in-one measurement system Paios (from Fluxim AG)⁴⁷ is used. For accurate values and to avoid heating/damaging the OLED device each voltage point can be applied as a pulse, where after a specific time the current and photodetector voltage are measured. The measurement settings and the data processing is done with the Characterization Suite software (from Fluxim AG)⁴⁶. Besides the key figure luminance also the current efficiency at 0° (CE = L/J) can be displayed.

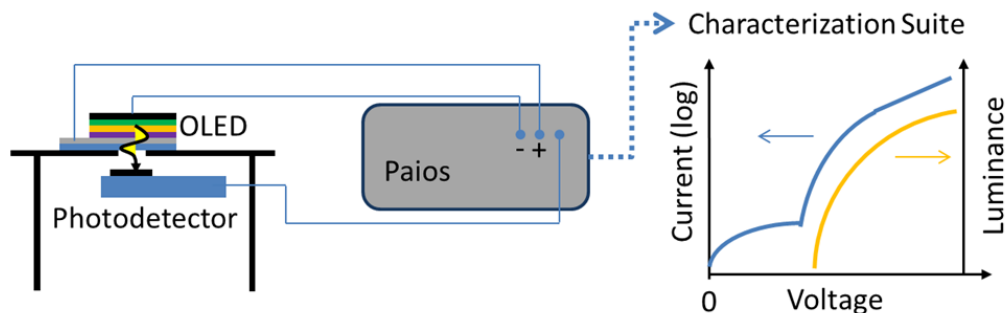


Figure 1.8 – Schematic illustration of the used current-Voltage-Luminance measurement setup and of a typical I-V-L curve. Paios and Photodetector are commercial hardware products and characterization suite is the controlling software for Paios^{44,46,47}.

Angle-dependent Electroluminescence

Another and important characterization technique is the angle-dependent electroluminescence (EL) measurement, where the s- or p-polarized spectral emission pattern of an OLED under a certain current is measured. In **Figure 1.9** a schematic illustration of the angle-dependent EL spectra measurement with resulting typical EL spectrum plot, as well as drawing and photo of the self-developed goniometer setup and resulting commercial product Phelos (commercialized by Fluxim AG)⁴⁸.

Using an index matching outcoupling lens (as illustrated in Figure 1.9a) attached to the glass substrate (≈ 1.52) the total internal reflection of light at the glass/air interface is vanished and the generated light in the OLED is also outcoupled at angles $> 42^\circ$ perpendicular to the surface. With the moving detector head, consisting of a polarizer and a $\lambda/4$ plate, the s- or p-polarized angle-dependent internal angle-dependent EL spectra of an OLED can be measured in a range of 0° to $\pm 70^\circ$ with the home-made setup (Figure 1.9b). In Phelos (Figure 1.9c), due to fixed detector and moving sample, the whole 0° to 360° view angle range can be measured. Knowing the quantity of outcoupled light and its emission pattern, the EQE and other efficiency key figures described above can be derived. Furthermore with angle-dependent luminance spectra measurements the dipole orientation of the emitting species can be determined by analyzing the p-polarized angle-dependent PL⁴⁹ or EL spectra⁵⁰ (not done in this work).

In this work in the following chapters 2, 3 and 4 the home-made setup is used to measure angle-dependent s-polarized EL spectra on optically detuned OLEDs (adapted ETL thickness for enhancing s-polarized emission) to determine and analyze the emission zone in the investigated phosphorescence-based and state-of-the-art TADF OLEDs. Details on the emission zone determination are described in chapter 2.

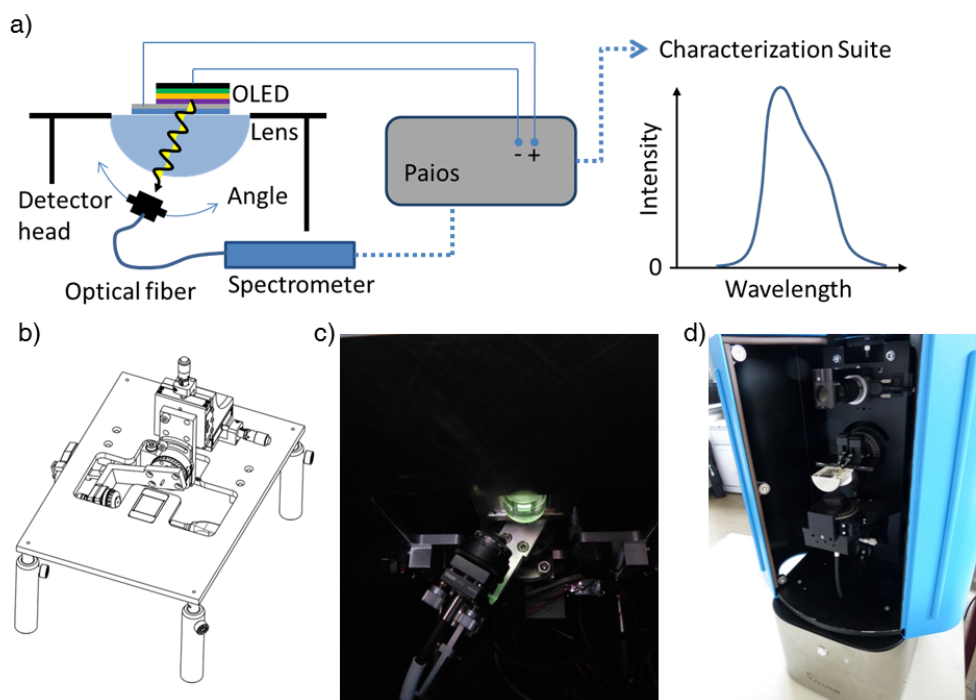


Figure 1.9 – Schematic illustration of angle-dependent EL spectra measurement and typical EL spectrum plot (a) and drawing and photo of the self-developed goniometer setup (b) and (c), as well as a photo of the resulting commercially product Phelos (d), distributed by Fluxim AG⁴⁸.

Transient Electroluminescence

To investigate exciton dynamics in an OLED, such as exciton quenching in form of triplet-triplet annihilation (TTA) or triplet-polaron quenching (TPQ)⁵¹, often the luminescence decay behavior after turning-off the OLED to zero or negative voltages is analyzed. Depending on the light generation in the OLED, the transient electroluminescence (EL)⁵², the photoluminescence (PL)⁵³ or a combination of PL/EL⁵⁴ can be analyzed.

In this work bias-dependent transient EL decay of the investigated phosphorescent and TADF OLEDs are measured to analyze the exciton dynamics. In chapter 2 and 3 this characterization method is used to analyse the exciton quenching in form of triplet-triplet annihilation (TTA) or triplet-polaron quenching (TPQ) and additionally used to verify the split emission zone in the OLED. For the measurements of the EL decay signals a gated photomultiplier tube (PMT H11526-01) from Hamamatsu⁵⁵ with a response time < 1 ns was incorporated and connected to the commercial available liquid nitrogen crystate add-on module to Paios from Fluxim AG (see **Figure 1.10**). The PMT current output is measured with a 50 Ω measurement resistor. The obtained PMT voltage is used to calculate the luminance (see above luminance calculation from photodetector voltage in I-V-L), considering the PMT spectral sensitivity and gain, as well as the distance from the PMT to the light mixing rod. The light mixing rod between the OLED and the PMT increases the light collection due to the closer distance to the OLED (additional

collection of light from larger viewing angles) and thus increases the signal to noise ratio of the measurement.

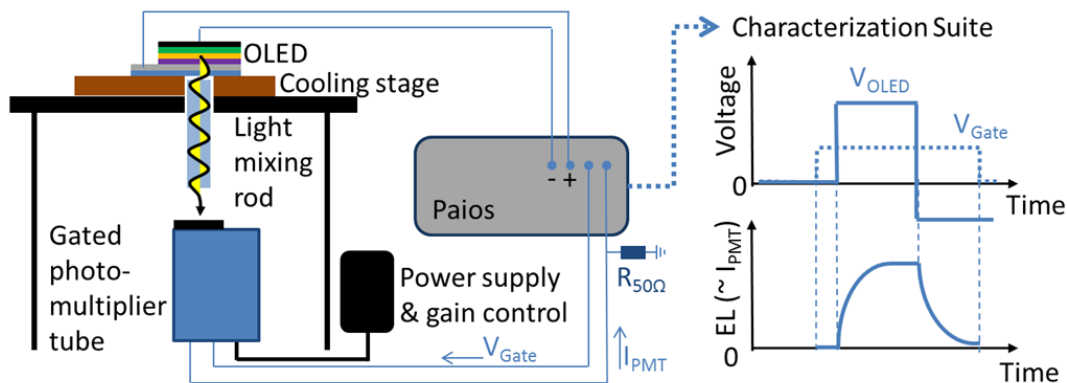


Figure 1.10 – Schematic illustration of the transient EL measurement setup, as well as typical plots for the applied voltage pulse and measured transient light.

In Figure 1.10 the depicted cooling stage (from Linkam Scientific)⁵⁶ in the measurement setup, having a temperature range of 100 – 500 K, was used for performing temperature-dependent EL decay measurements on TADF OLEDs (data not shown in this work) to analyze the reverse intersystem crossing process. Details on the reverse intersystem crossing process in TADF OLEDs are explained in the next subsection.

1.2.5 Exciton dynamics

The exciton dynamics in OLEDs describe several physical mechanisms such as exciton formation, diffusion, decay and quenching and thus it is essential for the understanding of an OLED, as well as for accurate electro-optical device modelling (see section 1.3). In the following the individual processes are described and the physical mechanisms explained. For detailed quantum mechanical calculations the textbooks by A. Köhler and H. Bässler¹⁵ and M. Pope and C.E. Swenberg¹⁷ are recommended.

Exciton formation

In an OLED under operation, after electron and hole injection and transport in the organic towards them via an electrical field, an electron-hole pair can be formed through Coulombic attraction if an electron in the LUMO and a hole in the HOMO are in close proximity. This electron-hole pair is then called exciton and depending on its spin state it is called singlet or triplet exciton. From spin statistics the ratio of singlet to triplet exciton formation is 1:3.

In quantum mechanical textbooks^{15,17} the singlet/triplet exciton formation ratio of 1:3 can be derived using instead of one exciton a two-particle system of two electrons, where one of them is located in the ground state and the other in an excited state and each of them has a spin of either $+\frac{1}{2}$ or $-\frac{1}{2}$. The sign indicates the direction of the spin (often also written

as spin up or down, or drawn as \uparrow or \downarrow). The total spin of the two-particle system can have either $S = 0$ or $S = 1$, resulting in four possible combinations (spin system multiplicities $2S+1$), as shown in **Figure 1.11a**. For the total spin of $S = 0$ only one combination is possible (with eigenvalue $M_S = 0$) and thus this combination is called singlet and for the total spin of $S = 1$ three combinations are possible (with eigenvalues $M_S = -1, 0, 1$) and thus this arrangement is called triplet. Looking at the probability, the above mentioned singlet to triplet exciton formation ratio of 1:3 is obtained.

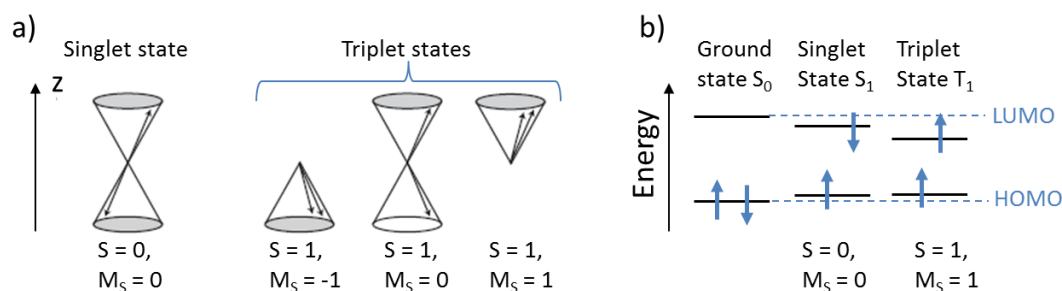


Figure 1.11 – Schematic illustration of the singlet and triplet states depicted with two electron spins in form of vectors, which precess around a local magnetic field in z -direction (a) and in an energy level diagram (b). S and M_S denote the total spin of the two-electron system and its eigenvalue. Adapted from textbook¹⁵

Figure 1.11b shows the singlet and triplet state formation when the two-particle system is located on one molecule. The energy difference between the singlet state S_1 and triplet state T_1 is twice the energy of the exchange integral, which strongly depends on the wavefunction overlap between the LUMO and HOMO¹⁵. The larger the overlap of the wavefunctions, the larger the exchange energy and thus the stronger the exchange interaction. In TADF OLEDs the reverse transition, from the triplet state to the singlet state, is wanted (cf. Figure 1.14). Therefore small exchange energies are needed, which can be achieved if the LUMO and HOMO are located on different molecular moieties or on two different molecules. In the latter case the formed electron-hole pair is called exciplex (or in the OPV community often also called charge-transfer exciton). In chapter 4 TADF exciplex host OLEDs are investigated, showing a small exchange energy of only 8.5 meV. The described exciton processes in the following can be also applied in the same way for exciplexes, but for clarity it is only shown for excitons.

Exciton diffusion

After the formation of an exciton through an electron and hole, described above, the exciton has a certain lifetime depending on the material and its spin state (singlet or triplet). In this lifetime the exciton on a molecule can transfer its energy in a non-radiative manner to a neighbouring molecule due to quantum chemical coupling, as following:



Where D^* denotes the excited state donor molecule (= exciton containing molecule) and A denotes the neighbouring ground state acceptor molecule (A). After the energy transfer, the donor molecule (D) is in its ground state and the acceptor molecule is in its excited state (A^*). This energy transfer can be described by the Förster resonance energy transfer (FRET)⁵⁷ or the Dexter energy transfer (DEX)⁵⁸. **Figure 1.12a** schematically shows the Dexter energy transfer, where the energy transfer takes place through electron exchange between the excited donor molecule and the ground state acceptor molecule. Due to electron exchange the distance between the molecules is limited to less than 1 nm and only singlet to singlet or triplet to triplet transitions are allowed (Wigner spin conservation theorem)⁵⁹. In Figure 1.12b the Förster resonance energy transfer is shown. There dipole-dipole interactions between the excited donor molecule and ground state acceptor molecule are involved leading to much larger possible molecule distances of 1 nm to 10 nm. The Förster resonance energy transfer is allowed for singlet to singlet transition, but not for the triplet to triplet transition due to the Pauli exclusion principle^{60,61}, which says that a quantum state cannot be occupied by two electrons with the same spin (which would be the case if in Figure 1.12b the excited donor molecule D^* would be a triplet).

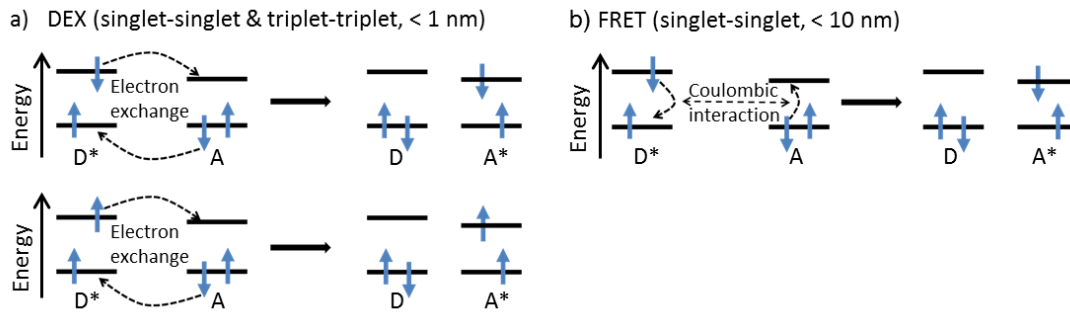


Figure 1.12 – Schematic illustration of the Dexter energy transfer (DEX), using electron exchange, which is allowed for singlet-singlet and triplet-triplet states in close proximity (a) and Förster resonance energy transfer (FRET) using dipole-dipole interaction, which is allowed for singlet-singlet states (not for triplet-triplet states due to Pauli principle) with a energy transfer distance up to 10 nm (a).

Both energy transfers can be used to describe exciton diffusion in OLEDs between same molecule types or in a host-guest system, from the host to the guest molecule. Energy transfer equations and the derivation for the Dexter and Förster resonance energy transfers can be found in detail in reference¹⁵. In both cases the energy transfer depends on the spectral overlap integral J , which expresses the overlap of the involved orbitals from the donor (D^*) and acceptor (A), as follows:

$$J = \int I_D(\lambda) \epsilon_A(\lambda) \lambda^4 d\lambda \quad (1.11)$$

There, $I_D(\lambda)$ is the normalized fluorescence spectrum of the donor and $\epsilon_A(\lambda)$ is the extinction coefficient, conventionally expressed in $\text{M}^{-1}\text{cm}^{-1}$. These quantities can be experimentally obtained (see Figure S4.2) and thus can give a first hint if exciton diffusion is large or small.

Exciton decay

As mentioned above an exciton has a certain lifetime, and after this lifetime the exciton decays, quantum mechanically this means that a transition from the excited state (S_1 or T_1) to the ground state S_0 takes place, which can be either radiative under generation of a photon or non-radiative under generation of heat through phonons from multiple vibrational relaxations. The radiative decay from S_1 state is commonly called fluorescence and from the T_1 state it is commonly called phosphorescence, as shown in **Figure 1.13a**. These transition or decay rates can be obtained experimentally from photoluminescence quantum efficiency measurements⁶² or quantum mechanically calculated with the Fermi's golden rule¹⁸.

In fluorescence-based OLEDs, phosphorescence is forbidden because it would conflict with the Pauli exclusion principle⁶⁰ that forbids the occupation of one state with two electrons with the same spin. Thus, in these OLEDs the formed triplet excitons decay non-radiatively through intersystem crossing and vibrational relaxation to the ground state and are lost for light emission. In phosphorescence-based OLEDs, however, organometallic-complexes with a heavy atom, such as the Ir(ppy)₂(acac) complex⁶³ (Figure 1.13b), are used as emitters, where due to spin-orbit coupling an admixture of the singlet state character into the triplet state takes place and thus allows the radiative transition from the T_1 state to the ground state S_0 ¹⁵. In general this allowed transition results in much higher efficiencies in phosphorescence-based OLEDs compared to fluorescence-based ones⁵¹.

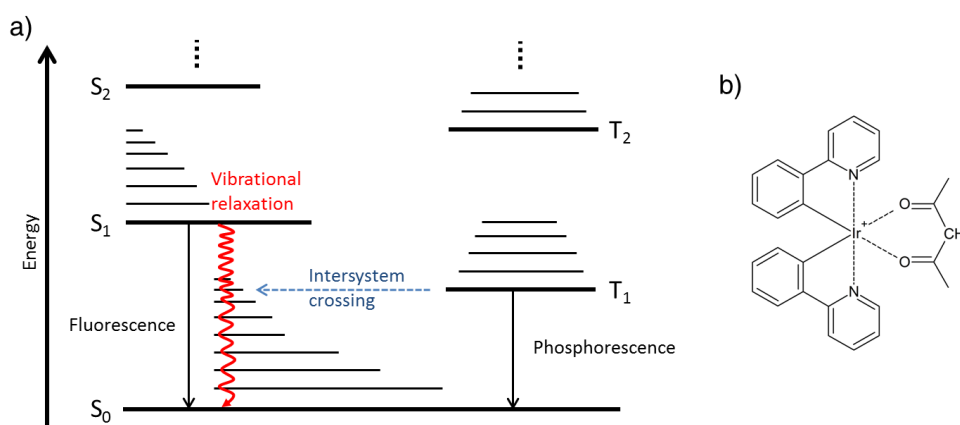


Figure 1.13 – Jablonski-diagram of a molecule (a), showing the ground state S_0 , as well as excited singlet (S_1 , S_2) and triplet states (T_1 , T_2) with vibrational levels. Arrows indicate different radiative and non-radiative transitions between different states. In (b) the chemical structure of the organometallic-complex Ir(ppy)₂(acac)⁶³ is shown, which is used often in OLEDs as phosphorescent emitter.

Recently a new mechanisms, called thermally activated delayed fluorescence (TADF), was employed in OLEDs by Adachi and coworkers³⁵, allowing delayed fluorescence from triplet states without using emitting metal-complexes. They synthesized fluorescent emitter molecules having a small singlet/triplet energy difference ΔE and thus allowed efficient reverse intersystem crossing (RISC) from the T_1 to S_1 state, leading to a delayed fluorescence and thus strongly improved efficiency in the fluorescence-based OLED. The TADF mechanism is schematically illustrated in **Figure 1.14**.

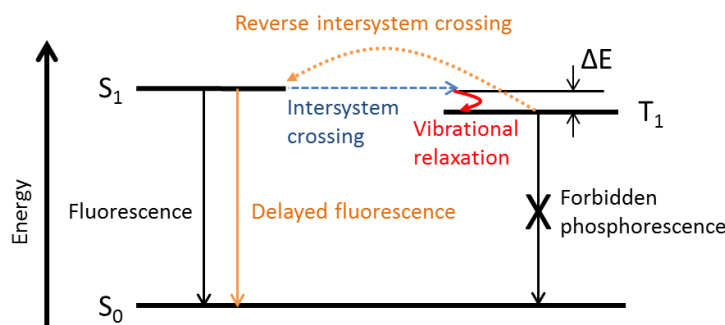


Figure 1.14 – Schematic illustration of TADF mechanism, where singlet/triplet energy barrier is minimized and thus reverse intersystem crossing gets efficient leading to delayed fluorescence.

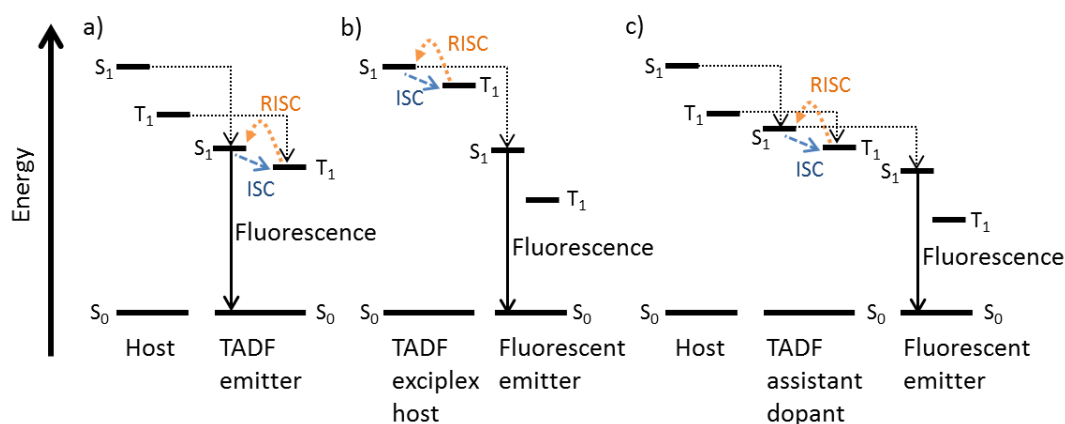


Figure 1.15 – Schematic illustration of different OLED device approaches to implement the TADF mechanism for harvesting of the generated triplet excitons on the host through TADF emitter (a), TADF exciplex host (b) and TADF assistant dopant (c). Only main/dominant transitions are shown for clarity. In a complete illustration all non-radiative transitions from the S_1 and T_1 states, possible radiative transitions from the host S_1 , TADF exciplex host S_1 or TADF assistant dopant S_1 state, transitions from the S_1 to T_1 states, as well as transitions from T_1 to T_1 states in (b) and (c) must be included.

Currently, in research different device approaches are followed to implement this TADF mechanism in fluorescence-based OLEDs to improve the efficiency by harvesting the generated

triplet excitons at the host so that they can contribute to light emission. Mostly and what also Adachi and coworker reported first, is the replacement of the fluorescent or phosphorescent dye in the OLED device with a TADF emitter^{35–37} (see **Figure 1.15a**). Another approach is the fabrication of OLEDs with exciplex hosts showing TADF characteristics and using common fluorescent emitter dyes⁶⁴, shown in Figure 1.15b. TADF OLEDs with this approach are investigated in this thesis in chapter 4, via electro-optical characterization and device modelling. In Figure 1.15c, TADF molecules are additionally included as assistant dopant to the fluorescent dye in a common host^{65–67}. Further reported approaches (not shown in Figure 15) are combinations of TADF exciplex host and TADF emitter⁶⁸ or TADF exciplex host and TADF assistant dopant⁶⁹. A more detailed overview on TADF OLED approaches and resulting efficiencies can be found in reference²⁹ and⁶⁵.

Exciton quenching

Exciton quenching processes can be found often in OLEDs operated at high current driving conditions, where high exciton and charge carrier densities are present. There the non-radiative quenching of an exciton can take place either by another exciton, then it is called exciton-exciton annihilation or by a electron or hole polaron, then it is called exciton-polaron quenching under the release of heat. Due to the presence of singlet and triplet excitons in an OLED, several combinations among each other can be found^{18,51}, as following:



Where S_1 and T_1 are singlet or triplet excitons, P can be either a electron or hole polaron, S_0 is the ground state and n^* denotes a higher excited state. All these exciton quenching processes have in common, that they reduce the efficiency due to the loss of an exciton for light emission. In literature this efficiency reduction at high currents through exciton quenching processes is described as efficiency roll-off⁵¹ and is most prominent in phosphorescence-based and the above mentioned TADF OLEDs, where the long-living triplet excitons play an important role for light emission. **Figure 1.16** shows schematically the triplet exciton quenching processes via triplet-triplet annihilation and triplet-polaron quenching, where the non-radiative transition of a triplet exciton to the ground state leads to an excitation of a neighbouring triplet exciton (or polaron) to a higher excited state. This higher excited triplet or polaron then immediately falls down to the lowest excited state through internal conversion and vibrational relaxation under the release of heat and hence a triplet exciton is lost for light emission.

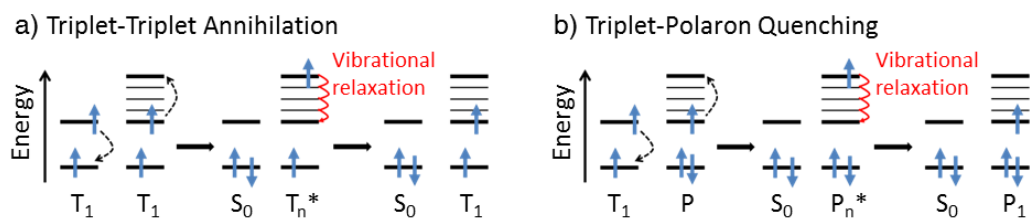


Figure 1.16 – Schematic illustration of non-radiative triplet-triplet annihilation (a) and triplet-polaron quenching process (b), where T_1 is the triplet exciton, P is a electron or hole polaron, S_0 is the ground state and n^* denotes a higher excited electronic state.

1.3 Device Modelling

Device modelling is an important method to understand the physics of an OLED. Based on measureable macroscopic quantities, such as current, voltage and light of an OLED, it is tried to establish find appropriate model equations describing the internal processes and thus allows to elucidate the physical mechanisms of an OLED. For the device model in this work a 1D numerical drift-diffusion model is provided with the commercial simulation software Setfos (Fluxim AG)⁷⁰. Details on the framework of the 1D drift-diffusion model in Setfos can be found in reference⁷¹ and⁷². For details on other device modelling approaches, such as master equation calculations or kinetic Monte Carlo simulations the reference⁷³ is recommended.

In the following two subsections a basic description of the electrical and optical model in Setfos is given. In the subsection 1.3.3 the comprehensive electro-optical device model used in this work is introduced.

1.3.1 Electrical modelling of injection, drift and diffusion of charge carriers

In Setfos the numerical modelling of charge carrier injection is based on the metal-organic contact, the applied bias, the electrode metal work function and the respective LUMO/HOMO energy level in the organic semiconductor material. For the metal-organic contact two model implementations are available.

First, for an ohmic contact, charge carrier injection is not limiting the device current. An ohmic contact is used in this work for the injection of electrons at cathode/organic interface because of the small energy barriers of less than 0.3 eV in the investigated OLEDs. The injected electron density n into the LUMO energy level of the organic semiconductor is calculated from the cathode metal work function ϕ using Boltzmann statistics as follows:

$$n = N_0 \exp\left(\frac{\phi_{Cathode} - LUMO}{k_B T}\right) \quad (1.17)$$

where N_0 denotes the density of chargeable sites in the organic, k_B is the Boltzmann constant and T is the temperature.

Second, for a thermionic contact, charge carrier injection is modelled with a field-dependent injection barrier and image charge recombination⁷⁴, which is used in this work for the hole injection at the anode/organic interface where energy barriers are larger than 0.3 eV. The hole injection current from the anode metal work function into the HOMO energy level in the organic semiconductor is calculated as follows:

$$J_p = \mu_p \frac{C}{e^2} \left(N_0 \exp\left(\frac{HOMO\phi_{Anode}}{k_B T}\right) + f^{\frac{1}{2}} \right) - p \cdot S_E, \quad (1.18)$$

where μ_p is the hole mobility in the organic, e is the elementary charge, C denotes a constant factor, f denotes a reduced electric field, p the hole density in the organic and S_E is a surface

recombination velocity. Further details can be found in reference⁷⁴.

Having the charge carriers now injected into the organic from the electrodes, the subsequent charge carrier transport in the organic semiconductors is mathematically described with the general semiconductor drift-diffusion equations^{71,75,76}:

$$\nabla E(x) = (p - n + A_{Doping} - D_{Doping}) \cdot \frac{e}{\epsilon_r \epsilon_0} \quad (1.19)$$

$$J_n = -en\mu_n E(x) + eD_n \nabla n \quad (1.20)$$

$$J_p = ep\mu_p E(x) - eD_p \nabla p \quad (1.21)$$

$$\frac{dn}{dt} = -\frac{1}{-e} \frac{dJ_n}{dx} - R(n, p) \quad (1.22)$$

$$\frac{dp}{dt} = -\frac{1}{e} \frac{dJ_p}{dx} - R(n, p) \quad (1.23)$$

The first equation 1.19 is Poisson's equation, which relates the gradient of the electrical field $E(x)$ to the mobile electron and hole densities n and p and to the local acceptor doping (A_{Doping}) and donor doping (D_{Doping}) densities, where e is the elementary charge and ϵ_0 vacuum permittivity and ϵ_r is the relative permittivity of the organic material, with the boundary condition of

$$\int_0^L E(x) dx = V_{app} - V_{bi} \quad (1.24)$$

where L is the total thickness of the semiconductor layers, V_{app} is the applied voltage and V_{bi} is the built-in voltage, which is defined as the difference of the metal workfunctions of the electrodes ($eV_{bi} = \phi_{Anode} - \phi_{Cathode}$).

The equations 1.20 and 1.21 represents the current drift-diffusion equations for the mobile electrons and holes in the organic semiconductors, where the first term is the drift part with $\mu_{n,p}$ denoting the charge carrier mobilities and the second term is the diffusion term with $D_{n,p}$ denoting the diffusion constants, which are linked to the charge carrier mobilities by the classical Einstein relation⁷⁷:

$$D_{n,p} = \mu_{n,p} \frac{k_B T}{e} \quad (1.25)$$

In organic semiconductors the charge carrier mobility is generally dependent on the electrical field. In this thesis we employ the Pool Frenkel mobility law⁷⁸

$$\mu_{n,p} = \mu_0 e^{\gamma_{n,p} \sqrt{E}}, \quad (1.26)$$

where μ_0 is the zero-field mobility, $\gamma_{n,p}$ is the field-dependence parameter and E is the electrical field.

The last two organic semiconductor drift-diffusion equations are the continuity equations for electrons and holes, which account for the conservation of the charge carriers in the organic

semiconductor layers. The R term describes the bimolecular recombination of electrons and holes which can be expressed by

$$R(n, p) = \eta np(\mu_e + \mu_h) \frac{e}{\epsilon_r \epsilon_0} \quad (1.27)$$

according to the Langevin theory⁷⁹. Thus the recombination rate R depends on the local charge carrier densities n and p, the sum of the electron and hole mobility ($\mu_e + \mu_h$) and the relative permittivity ϵ_r of the organic material. η is a phenomenological correction parameter, which in this work is set to 1. Multiplying this recombination rate R with the singlet/triplet factor yields the exciton formation rate that enters in the exciton continuity equation (see subsection 1.3.3).

1.3.2 Optical modelling of light outcoupling and emission zone

To describe light outcoupling from an OLED, the optical model in Setfos simulates the radiative decay rate of an emitter as power radiated from an oscillating electrical dipole. This basic concept was first described by Sommerfeld⁸⁰ and later expanded by Chance et al.⁸¹ for optical cavities. In a planar multilayer-system, as assumed for the OLED device stack, the modelling of the light propagation through the individual layers has to take into account the polarization-dependent Fresnel reflection ($r_{s,p}$) and transmission ($t_{s,p}$) coefficients at all involved interfaces⁸². Several other parameters, such as the emitter spectrum ($I(\lambda)$), emitter orientation (θ) and emitter position (z) in the OLED stack, and (birefringent) refractive index (n or n_o, n_e), extinction coefficient (k or k_o, k_e) and thickness (d) for all layers are influencing the dipole radiation and thus must be considered^{32,71,83,84}, as depicted in **Figure 1.17**.

Due to the microcavity in an OLED (Purcell effect³⁹) the radiative decay rate of the emitter is modified and thus the radiated power of the dipole in the OLED amounts to^{32,71,83–85}

$$b = (1 - q_0) b_0 + q_0 b_0 \cdot F \quad (1.28)$$

where b is the total dissipated power of the dipole. The first term denotes the non-radiative fraction with q_0 being the intrinsic radiative quantum efficiency (see subsection 1.2.4) and b_0 being the intrinsic power of the dipole in an isotropic, infinite medium. The second term is the radiative fraction, which is modified by the Purcell factor F, where F can be expressed by means of a parametrization of the emission angle θ_e :

$$F = \int_0^\infty f(u) du \quad (1.29)$$

with $u = k_{parallel} / k = n_e \sin(\theta) / n_e = \sin \theta_e$, where n_e is the refractive index of the emitter medium. A partial integration of $f(u)$ within certain limits of u determined by the total internal reflection law, thus, yields the fractional radiated power that can be outcoupled. Using different u integration limits the fractional radiated power assigned to substrateguided (light trapped in the glass substrate), wave guided (light trapped in the organic) and evanescent

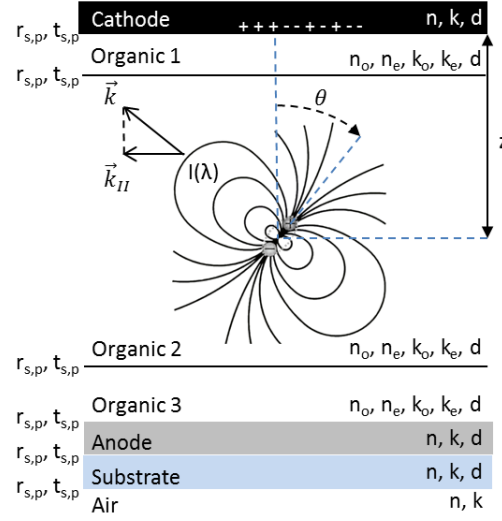


Figure 1.17 – Schematic illustration of an oscillating electrical dipole placed in a planar multilayer-system forming a microcavity. Where the cathode is assumed to be metallic and thus depending on the distance (z) more or less surface plasmons are formed. All other parameters are described in the text. Figure is adapted from reference³².

modes (light forms surface plasmons) can also be calculated:

$$u = 0 \dots n_{air}/n_e \quad \text{Outcoupled modes} \quad (1.30)$$

$$u = n_{air}/n_e \dots n_{sub}/n_e \quad \text{Substrate guided modes} \quad (1.31)$$

$$u = n_{sub}/n_e \dots 1 \quad \text{Wave guided modes} \quad (1.32)$$

$$u = 1 \dots \infty \quad \text{Evanescent modes} \quad (1.33)$$

where n_{air} , n_{sub} and n_e are the refractive indices of air ($n_{air} = 1$), the substrate layer and the emission layer. In addition to the radiative fraction of the outcoupled light, the optical model in Setfos can display also the spectrum and angle-dependence of the outcoupled, emitted light, and its s- or p-polarized contribution. **Figure 1.18** shows the decomposition of an arbitrarily oriented dipole into three orthogonal dipoles in regard to the layer plane and the corresponding polarizations.

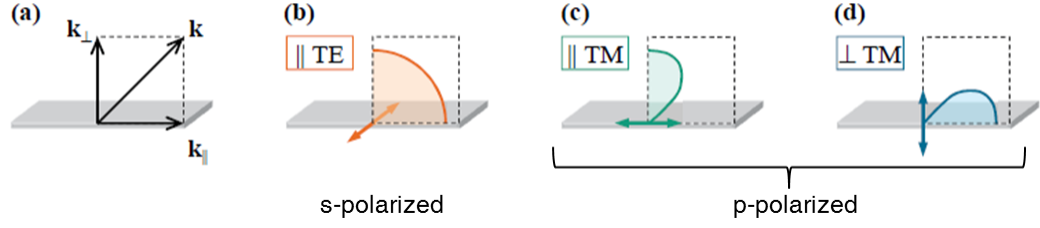


Figure 1.18 – Schematic illustration of *s*- and *p*-polarization, where the *s*-polarized contributions comes from the with the wavevector \mathbf{k} and its parallel and perpendicular components in (a) and the three orthogonal oscillating dipoles (b-d) placed in the layer plane and their corresponding radiation patterns. Figure is adapted from reference⁸⁶.

Using the simulated emission spectra and fitting them to measured *s*-polarized angle-dependent electroluminescence spectra, the optical model in Setfos can determine the emission zone profile^{87–90}. This inverse problem is solved in the model by employing a linear least square fit with the mathematical task to minimize the residuum $r^s(\theta_e, \lambda)$ between simulated and measured spectra⁸⁸:

$$r^s(\theta_e, \lambda) = \sum_{z=1}^N I_{sim}^s(\theta_e, \lambda, d_z) \cdot P(d_z) - I_{meas}^s(\theta_e, \lambda) \quad (1.34)$$

Where θ_e is the emission angle, λ denotes the wavelength. The first term, the simulated *s*-polarized spectra are expressed as the superposition of assumed discrete emitters (dirac shape functions) $I_{sim}^s(\theta_e, \lambda, d_z)$ equally distributed in the EML and a weighting factor $P(d_z)$ at each emitter positions d_z . During the fit of the simulated spectra to the measured ones (second term) the weighting factor is adapting the amplitudes of the discrete emitter to reduce the residuum. For minimized $r^s(\theta_e, \lambda)$ the vector of $P(d_z)$ yields the emission zone profile in the OLED. Further readings on emission zone determination from angle-dependent EL spectra measurements and combined optical simulations can be found in references^{50,91–93}.

1.3.3 A comprehensive electro-optical device model

The used comprehensive electro-optical device model in Setfos closes the gap between the electrical drift-diffusion model (charge carrier injection, transport and exciton formation) and the optical model (radiative excition decay, light outcoupling, Purcell effect) by introducing an optical feedback giving the excitons a position-dependent lifetime as shown in **Figure 1.19**.

The dynamics of the excitons (see subsection 1.2.5) in the OLED are accounted for by an additional continuity equation for excitons in the model. This equation includes the exciton formation term from the drift-diffusion model, as well as the terms for radiative and non-radiative decay that depend on the position of the emissive dipole inside the emitter layer. For

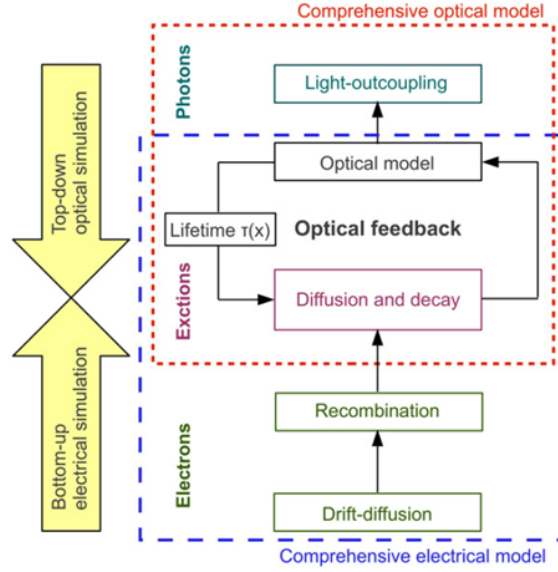


Figure 1.19 – Schematic illustration of used comprehensive electro-optical device model in Setfos accounting for electrons, excitons and photons. Figure taken from reference⁷².

example the continuity equation for triplet excitons used in the device model in chapter 3 to describe a phosphorescence-based OLED reads as follows

$$\begin{aligned} \frac{d\mathcal{T}(t, z)}{dt} = & G \cdot R(t, z) - F(z) \cdot k_{rad} \cdot \mathcal{T}(t, z) - k_{nonrad} \cdot \mathcal{T}(t, z) \\ & - k_{TPQH} \cdot \mathcal{T}(t, z) \cdot p(t, z) - k_{TPQE} \cdot \mathcal{T}(t, z) \cdot n(t, z) \\ & - k_{ann} \cdot \mathcal{T}(t, z)^2 + \nabla J_s(t, z) \end{aligned} \quad (1.35)$$

The exciton formation term is given with $G \cdot R(t, z)$, where G is the same as the singlet/triplet factor and R is the time (t) and position (z)-dependent Langevin recombination rate. The modified radiative decay term is given by $F(z) \cdot k_{rad} \cdot \mathcal{T}(t, z)$, where $F(z)$ denotes the position-dependent Purcell factor and k_{rad} is the intrinsic radiative decay rate of the triplet excitons $\mathcal{T}(t, z)$. In quantum mechanical terms it is the transition rate from the excited T_1 state to the ground state S_0 (see subsection 1.2.5). The other terms describe non-radiative decay, triplet-polaron quenching with holes and with electrons and triplet-triplet annihilation and exciton diffusion (Details see chapter 3).

In more advanced OLEDs, such as the investigated state-of-the-art TADF OLEDs (see chapter 4), three continuity equations for host singlet and triplet exciplexes and guest singlet excitons with individual or coupled dynamics, such as host-guest energy transfer or TADF mechanism, are modelled for accurate description of the experimental data.

References

1. Königsberger, J. & Schilling, K. Über Elektrizitätsleitung in festen Elementen und Verbindungen. I. Minima des Widerstandes, Prüfung auf Elektronenleitung, Anwendung der Dissoziationsformeln. *Annalen der Physik* **337**, 179–230 (1910).
2. Pauli, W. E. Lichtelektrische Untersuchungen an fluoreszierenden Substanzen. *Annalen der Physik* **345**, 677–700 (1913).
3. Pochettino, A. Sul comportamento fotoelettrico dell' antracene. *Rendiconti*, **15** (1906).
4. Stark, J. & Steubing, W. Fluorescence and light electrical sensitivity of organic substances. *Annalen der Physik* **32** (1908).
5. Bernanose, A., Comte, M. & Vouaux, P. A new method of emission of light by certain organic compounds. *J. chim. Phys.* **50** (1953).
6. Pope, M., Kallmann, H. P. & Magnante, P. Electroluminescence in Organic Crystals. *The Journal of Chemical Physics* **38**, 2042–2043 (Apr. 15, 1963).
7. Helfrich, W. & Schneider, W. G. Recombination Radiation in Anthracene Crystals. *Physical Review Letters* **14**, 229–231 (Feb. 15, 1965).
8. Chiang, C. K. *et al.* Electrical Conductivity in Doped Polyacetylene. *Physical Review Letters* **39**, 1098–1101 (Oct. 24, 1977).
9. Kivelson, S. & Heeger, A. J. Intrinsic conductivity of conducting polymers. *Synthetic Metals* **22**, 371–384. <http://www.sciencedirect.com/science/article/pii/0379677988901087> (Feb. 1, 1988).
10. Tang, C. W. Two-layer organic photovoltaic cell. *Applied Physics Letters* **48**, 183–185 (Jan. 13, 1986).
11. Tsumura, A., Koezuka, H. & Ando, T. Macromolecular electronic device: Field-effect transistor with a polythiophene thin film. *Applied Physics Letters* **49**, 1210–1212 (Nov. 3, 1986).
12. Tang, C. W. & VanSlyke, S. A. Organic electroluminescent diodes. *Applied Physics Letters* **51**, 14335, 913–915 (Sept. 21, 1987).
13. Burroughes, J. H. *et al.* Light-emitting diodes based on conjugated polymers. *Nature* **347**, 539. <https://www.nature.com/articles/347539a0> (Oct. 1990).
14. Baldo, M. A. *et al.* Highly efficient phosphorescent emission from organic electroluminescent devices. *Nature* **395**, 151–154. <https://www.nature.com/articles/25954> (Sept. 1998).
15. Anna Köhler, H. B. *Electronic Processes in Organic Semiconductors: An Introduction* Google-Books-ID: GXemBgAAQBAJ. 420 pp. ISBN: 978-3-527-33292-2. https://www.ebook.de/de/product/22338652/anna_koehler_heinz_baessler_electronic_processes_in_organic_semiconductors.html (John Wiley & Sons, June 8, 2015).
16. Markus Schwoerer, H. C. W. *Organische Molekulare Festkörper: Einführung in die Physik von pi-Systemen* Google-Books-ID: PPpM19gN_V4C. 509 pp. ISBN: 978-3-527-66235-7.

- https://www.ebook.de/de/product/22514591/markus_schwoerer_hans_christoph_wolf_organische_molekulare_festkoerper.html (John Wiley & Sons, Oct. 4, 2012).
17. Martin Pope, C. E. S. *Electronic Processes in Organic Crystals and Polymers* Google-Books-ID: AZVUAAAAMAAJ. 1368 pp. ISBN: 978-0-19-512963-2. https://www.ebook.de/de/product/3672754/martin_pope_charles_e_swenberg_electronic_processes_in_organic_crystals_and_polymers.html (Oxford University Press, 1999).
 18. Gaspar, D. J. & Polikarpov, E. *OLED Fundamentals: Materials, Devices, and Processing of Organic Light-Emitting Diodes* Google-Books-ID: dcjECQAAQBAJ. 474 pp. ISBN: 978-1-4665-1519-2 (CRC Press, May 15, 2015).
 19. Heraeus Epurio Clevios™, PEDOT:PSS https://www.heraeus.com/en/hep/products_hep/clevios/clevios_prod/clevios_1.html (2019).
 20. Lumtec Products http://www.lumtec.com.tw/portal_c1_cnt.php?owner_num=c1_290785&button_num=c1&folder_id=30643 (2019).
 21. *OLED inkjet printing* <https://www.oled-info.com/oled-inkjet-printing> (2019).
 22. *Flexible organic electronics - Fraunhofer FEP* en. https://www.fep.fraunhofer.de/en/Geschaeftsfelder/Flexible_organische_Elektronik.html (2019).
 23. *OLED Geschichte, first products* <https://www.oled.at/oled-geschichte/> (2019).
 24. Huang, J. *et al.* Low-voltage organic electroluminescent devices using pin structures. *Applied Physics Letters* **80**, 139–141 (Jan. 2, 2002).
 25. Tanaka, D. *et al.* Ultra High Efficiency Green Organic Light-Emitting Devices. *Japanese Journal of Applied Physics* **46**, L10 (Dec. 22, 2006).
 26. *OLED history* <https://www.oled-info.com/history> (2019).
 27. *OLED revenues* <https://www.oled-info.com/dscc-oled-market-will-grow-19-2019-reach-31-billion-revenues> (2019).
 28. Meerheim, R., Lussem, B. & Leo, K. Efficiency and Stability of p-i-n Type Organic Light Emitting Diodes for Display and Lighting Applications. *Proceedings of the IEEE* **97**, 1606–1626 (Sept. 2009).
 29. Kim, K.-H. & Kim, J.-J. Origin and Control of Orientation of Phosphorescent and TADF Dyes for High-Efficiency OLEDs. *Advanced Materials* **30** (Oct. 1, 2018).
 30. Ossila ITO Ossila. <https://www.ossila.com/products/oled-ito-substrates> (2019).
 31. Scholz, S., Kondakov, D., Lüssem, B. & Leo, K. Degradation Mechanisms and Reactions in Organic Light-Emitting Devices. *Chemical Reviews* **115**, 8449–8503 (Aug. 26, 2015).
 32. Brütting, W. & Adachi, C. *Physics of Organic Semiconductors* Google-Books-ID: K2U_t1nuRIQC. 707 pp. ISBN: 978-3-527-65496-3. https://www.ebook.de/de/product/21194106/physics_of_organic_semiconductors.html (John Wiley & Sons, Oct. 2, 2012).
 33. Tsutsui, T. & Takada, N. Progress in Emission Efficiency of Organic Light-Emitting Diodes: Basic Understanding and Its Technical Application. *Japanese Journal of Applied Physics* **52**. 00009, 110001. <http://iopscience.iop.org/1347-4065/52/11R/110001> (Nov. 1, 2013).

34. Adachi, C., Baldo, M. A., Thompson, M. E. & Forrest, S. R. Nearly 100% internal phosphorescence efficiency in an organic light-emitting device. *Journal of Applied Physics* **90**, 5048–5051 (Oct. 31, 2001).
35. Endo, A. *et al.* Thermally Activated Delayed Fluorescence from Sn4+–Porphyrin Complexes and Their Application to Organic Light Emitting Diodes — A Novel Mechanism for Electroluminescence. *Advanced Materials* **21**, 4802–4806 (2009).
36. Goushi, K., Yoshida, K., Sato, K. & Adachi, C. Organic light-emitting diodes employing efficient reverse intersystem crossing for triplet-to-singlet state conversion. *Nature Photonics* **6**, 253–258. <http://www.nature.com/nphoton/journal/v6/n4/abs/nphoton.2012.31.html> (Apr. 2012).
37. Uoyama, H., Goushi, K., Shizu, K., Nomura, H. & Adachi, C. Highly efficient organic light-emitting diodes from delayed fluorescence. *Nature* **492**, 00452, 234–238. <http://www.nature.com/nature/journal/v492/n7428/abs/nature11687.html> (Dec. 13, 2012).
38. Nowy, S., Krummacher, B. C., Frischeisen, J., Reinke, N. A. & Brütting, W. Light extraction and optical loss mechanisms in organic light-emitting diodes: Influence of the emitter quantum efficiency. *Journal of Applied Physics* **104**, 123109 (Dec. 15, 2008).
39. Purcell, E. M., Torrey, H. C. & Pound, R. V. Resonance Absorption by Nuclear Magnetic Moments in a Solid. *Physical Review* **69**, 37–38 (Jan. 1, 1946).
40. Greenham, N. C., Friend, R. H. & Bradley, D. D. C. Angular Dependence of the Emission from a Conjugated Polymer Light-Emitting Diode: Implications for efficiency calculations. *Advanced Materials* **6**, 491–494 (1994).
41. Saxena, K., Jain, V. K. & Mehta, D. S. A review on the light extraction techniques in organic electroluminescent devices. *Optical Materials* **32**, 221–233. <http://www.sciencedirect.com/science/article/pii/S0925346709002316> (Nov. 1, 2009).
42. *Spectral sensitivity of the human eye* <https://light-measurement.com/spectral-sensitivity-of-eye/> (2019).
43. *OLED Lifetime* <https://www.oled-info.com/oled-lifetime> (2019).
44. *Thorlabs Photodetector PDA36A* <https://www.thorlabs.de/thorproduct.cfm?partnumber=PDA36A&pn=PDA36A#11887> (2019).
45. *Characterization Suite 4.1 Manual* Fluxim. 00000 (). <https://www.fluxim.com/paios/>.
46. *Characterization Suite* Fluxim. <https://www.fluxim.com/news/2018/5/4/characterization-suite-41-released> (2019).
47. *Paios, Platform for All-In-One Characterization of Solar Cells and OLEDs, Characterization Suite Software version 4.12*, Fluxim Fluxim. 00000. <https://www.fluxim.com/paios/>.
48. *Phelos*, Fluxim Fluxim. 00000. <https://www.fluxim.com/phelos>.
49. Frischeisen, J., Yokoyama, D., Adachi, C. & Brütting, W. Determination of molecular dipole orientation in doped fluorescent organic thin films by photoluminescence measurements. *Applied Physics Letters* **96**, 00058, 073302 (Feb. 15, 2010).

50. Flämmich, M., Michaelis, D. & Danz, N. Accessing OLED emitter properties by radiation pattern analyses. *Organic Electronics* **12**, 00016, 83–91. <http://www.sciencedirect.com/science/article/pii/S1566119910003216> (Jan. 2011).
51. Murawski, C., Leo, K. & Gather, M. C. Efficiency Roll-Off in Organic Light-Emitting Diodes. *Advanced Materials* **25**, 00088, 6801–6827 (Dec. 1, 2013).
52. Baldo, M. A. & Forrest, S. R. Transient analysis of organic electrophosphorescence: I. Transient analysis of triplet energy transfer. *Physical Review B* **62**, 10958–10966 (Oct. 15, 2000).
53. Baldo, M. A., Adachi, C. & Forrest, S. R. Transient analysis of organic electrophosphorescence. II. Transient analysis of triplet-triplet annihilation. *Physical Review B* **62**, 10967–10977 (Oct. 15, 2000).
54. Wehrmeister, S. *et al.* Combined Electrical and Optical Analysis of the Efficiency Roll-Off in Phosphorescent Organic Light-Emitting Diodes. *Physical Review Applied* **3**, 00002, 024008 (Feb. 19, 2015).
55. Hamamatsu, Photomultiplier H11526-01 <https://www.hamamatsu.com/eu/en/product/type/H11526-01/index.html> (2019).
56. Linkam, Cooling Stage Linkam Scientific. <http://www.linkam.co.uk/temperature-controlled-stages> (2019).
57. Förster, T. Zwischenmolekulare Energiewanderung und Fluoreszenz. *Annalen der Physik* **437**, 55–75 (1948).
58. Dexter, D. L. A Theory of Sensitized Luminescence in Solids. *The Journal of Chemical Physics* **21**, 836–850 (May 1, 1953).
59. Wigner, E. P. *Gruppentheorie und ihre Anwendung auf die Quantenmechanik der Atom-spektren* ISBN: 978-3-663-02555-9. <https://www.springer.com/de/book/9783663025559> (2019) (Vieweg+Teubner Verlag, 1931).
60. Kaplan, I. G. Pauli Exclusion Principle and its theoretical foundation. *arXiv:1902.00499 [math-ph, physics:quant-ph]*. arXiv: 1902.00499 [quant-ph]. <http://arxiv.org/abs/1902.00499> (Jan. 29, 2019).
61. *Pauli exclusion principle* Page Version ID: 897472559. https://en.wikipedia.org/w/index.php?title=Pauli_exclusion_principle&oldid=897472559 (2019).
62. Kawamura, Y., Sasabe, H. & Adachi, C. Simple Accurate System for Measuring Absolute Photoluminescence Quantum Efficiency in Organic Solid-State Thin Films. *Japanese Journal of Applied Physics* **43**, 7729 (Nov. 10, 2004).
63. Lumtec, *Ir(ppy)2(acac)* http://lumtec.com.tw/portal_c1_cnt_page.php?owner_num=c1_290785&button_num=c1&folder_id=30652&cnt_id=257627&search_field=&search_word=&search_field2=&search_word2=&search_field3=&search_word3=&bool1=&bool2=&search_type=1&up_page=1 (2019).
64. Kim, K.-H., Moon, C.-K., Sun, J. W., Sim, B. & Kim, J.-J. Triplet Harvesting by a Conventional Fluorescent Emitter Using Reverse Intersystem Crossing of Host Triplet Exciplex. *Advanced Optical Materials* **3**, 00000, 895–899 (July 1, 2015).

65. Byeon, S. Y., Lee, D. R., Yook, K. S. & Lee, J. Y. Recent Progress of Singlet-Exciton-Harvesting Fluorescent Organic Light-Emitting Diodes by Energy Transfer Processes. *Advanced Materials*, 1803714 (Feb. 13, 2019).
66. Furukawa, T., Nakanotani, H., Inoue, M. & Adachi, C. Dual enhancement of electroluminescence efficiency and operational stability by rapid upconversion of triplet excitons in OLEDs. *Scientific Reports* **5**, 00006. http://www.nature.com/srep/2015/150212/srep08429/full/srep08429.html?WT.ec_id=SREP-639-20150217 (Feb. 12, 2015).
67. Nakanotani, H., Sasabe, H. & Adachi, C. Singlet-singlet and singlet-heat annihilations in fluorescence-based organic light-emitting diodes under steady-state high current density. *Applied Physics Letters* **86**, 00066, 213506 (May 23, 2005).
68. Moon, C.-K. *et al.* Combined Inter- and Intramolecular Charge-Transfer Processes for Highly Efficient Fluorescent Organic Light-Emitting Diodes with Reduced Triplet Exciton Quenching. *Advanced Materials* **29**, 1606448 (2017).
69. Li, D., Hu, Y. & Liao, L.-S. Triplet exciton harvesting by multi-process energy transfer in fluorescent organic light-emitting diodes. *Journal of Materials Chemistry C* **7**, 977–985. <https://pubs.rsc.org/en/content/articlelanding/2019/tc/c8tc05141k> (2019).
70. *Setfos 4.6, Fluxim Fluxim*. 00000. <https://www.fluxim.com/setfos-intro/>.
71. Ruhstaller, B. *et al.* in *Optoelectronic Devices and Properties*, edited by Oleg Sergiyenko, ISBN 978-953-307-204-3, DOI: 10.5772/14626 00009 (2011). (2017).
72. Perucco, B. *et al.* On the exciton profile in OLEDs-seamless optical and electrical modeling. *Organic Electronics* **13**, 1827–1835. <http://www.sciencedirect.com/science/article/pii/S1566119912002534> (Oct. 1, 2012).
73. Cottaar, J. Modeling of charge-transport processes for predictive simulation of OLEDs. <https://research.tue.nl/en/publications/modeling-of-charge-transport-processes-for-predictive-simulation-> (2012).
74. Scott, J. C. & Malliaras, G. G. Charge injection and recombination at the metal–organic interface. *Chemical Physics Letters* **299**, 115–119. <http://www.sciencedirect.com/science/article/pii/S0009261498012779> (Jan. 6, 1999).
75. Ruhstaller, B. *et al.* Transient and steady-state behavior of space charges in multilayer organic light-emitting diodes. *Journal of Applied Physics* **89**, 00224, 4575–4586 (Apr. 15, 2001).
76. Pflumm, A Numerical Scheme to Model Current and Voltage Excitation of Organic Light-Emitting Diodes.
77. Sutherland, W. LXXV. A dynamical theory of diffusion for non-electrolytes and the molecular mass of albumin. *The London, Edinburgh, and Dublin Philosophical Magazine and Journal of Science* **9**, 781–785 (June 1, 1905).
78. Frenkel, J. On Pre-Breakdown Phenomena in Insulators and Electronic Semi-Conductors. *Physical Review* **54**, 647–648 (Oct. 15, 1938).
79. Langevin, P. Recombinaison et mobilités des ions dans les gaz. *Ann. Chim. Phys* (1903).

80. Sommerfeld, A. Über die Fortpflanzung des Lichtes in dispergierenden Medien. *Annalen der Physik* **349**, 177–202 (1914).
81. Chance, R. R., Prock, A. & Silbey, R. in *Advances in Chemical Physics* 1–65 (John Wiley & Sons, Ltd, Mar. 2007). ISBN: 978-0-470-14256-1.
82. Yeh, P. *Optical Waves in Layered Media* 2nd. English. 420 pp. ISBN: 978-0-471-73192-4. https://www.ebook.de/de/product/3594646/pochi_yeh_optical_waves_in_layered_media.html (Wiley-Interscience, Hoboken, NJ, Mar. 1, 2005).
83. Neyts, K. A. Simulation of light emission from thin-film microcavities. *Journal of the Optical Society of America A* **15**. 00000, 962. <https://www.osapublishing.org/abstract.cfm?URI=josaa-15-4-962> (Apr. 1, 1998).
84. Novotny, L. Allowed and forbidden light in near-field optics. I. A single dipolar light source. EN. *JOSA A* **14**, 91–104. ISSN: 1520-8532. <https://www.osapublishing.org/josaa/abstract.cfm?uri=josaa-14-1-91> (2019) (Jan. 1997).
85. Perucco, B., Reinke, N. A., Müller, F., Rezzonico, D. & Ruhstaller, B. *The influence of the optical environment on the shape of the emission profile and methods of its determination in Organic Photonics IV* (eds Heremans, P. L., Coehoorn, R. & Adachi, C.) **7722**. 00002 (Proc. of SPIE, Apr. 2010), 77220F1. (2016).
86. Flämmich, M., Michaelis, D. & Danz, N. *In situ measurement of spectrum, emission zone, and dipole emitter orientation in OLEDs in Light-Emitting Diodes: Materials, Devices, and Applications for Solid State Lighting XV* (eds Streubel, K. P., Jeon, H., Tu, L.-W. & Linder, N.) **7954** (Proc. of SPIE, Feb. 2011), 7954101. (2016).
87. Jenatsch, S. *et al.* Time-Dependent p-i-n Structure and Emission Zone in Sandwich-Type Light-Emitting Electrochemical Cells. *ACS Photonics* **5**, 1591–1598. <https://doi.org/10.1021/acsp Photonics.8b00047> (2018) (Apr. 2018).
88. Perucco, B., Reinke, N. A., Rezzonico, D., Moos, M. & Ruhstaller, B. Analysis of the emission profile in organic light-emitting devices. *Optical Society of America* **18**. 00013, A246. http://www.opticsinfobase.org/view_article.cfm?gotourl=http%3A%2F%2Fwww%2Eopticsinfobase%2Eorg%2FDirectPDFAccess%2FBD2DC44F%2DDC94%2DF2EE%2D639CB01A65261B00%5F202487%2Foe%2D18%2DS2%2DA246%2Epdf%3Fda%3D1%26id%3D202487%26seq%3D0%26mobile%3Dno&org= (S2 June 21, 2010).
89. Regnat, M., Pernstich, K. P., Züfle, S. & Ruhstaller, B. Analysis of the Bias-Dependent Split Emission Zone in Phosphorescent OLEDs. en. *ACS Applied Materials & Interfaces* **10**, 31552–31559. ISSN: 1944-8244, 1944-8252. <http://pubs.acs.org/doi/10.1021/acsam.8b09595> (2018) (Sept. 2018).
90. Regnat, M., Pernstich, K. P. & Ruhstaller, B. Influence of the bias-dependent emission zone on exciton quenching and OLED efficiency. *Organic Electronics* **70**, 219–226. <http://www.sciencedirect.com/science/article/pii/S1566119919301922> (July 1, 2019).
91. Danz, N. *et al.* Detection of sub-10 nm emission profile features in organic light-emitting diodes using destructive interference. *Optics Letters* **37**, 4134–4136. <http://www.osapublishing.org/abstract.cfm?uri=ol-37-19-4134> (Oct. 1, 2012).

92. Gather, M. C., Flämmich, M., Danz, N., Michaelis, D. & Meerholz, K. Measuring the profile of the emission zone in polymeric organic light-emitting diodes. *Applied Physics Letters* **94**, 263301 (June 29, 2009).
93. Mensfoort, S. L. M. v. *et al.* Measuring the light emission profile in organic light-emitting diodes with nanometre spatial resolution. *Nature Photonics* **4**. 00052, 329–335. <http://www.nature.com/nphoton/journal/v4/n5/full/nphoton.2010.32.html> (May 2010).

2 Emission Zone Analysis in Phosphorescence-based OLEDs

Analysis of the Bias-Dependent Split Emission Zone in Phosphorescent OLEDs

Markus Regnat^{1,2}, Kurt P. Pernstich¹, Simon Züfle^{1,3}, Beat Ruhstaller^{1,3}

¹Zurich University of Applied Sciences ZHAW, Institute of Computational Physics, Technikumstrasse 9, 8400 Winterthur, Switzerland

²Institut des Matériaux, Ecole Polytechnique Fédérale de Lausanne, EPFL, Station 12, 1015 Lausanne, Switzerland

³Fluxim AG, Katharina-Sulzer-Platz 2, 8400 Winterthur, Switzerland

Reprinted with permission from ACS Applied Materials & Interfaces.

Copyright 2018 American Chemical Society.

ACS Appl. Mater. Interfaces, 2018, 10 (37), pp 31552–31559, DOI: 10.1021/acsami.8b09595

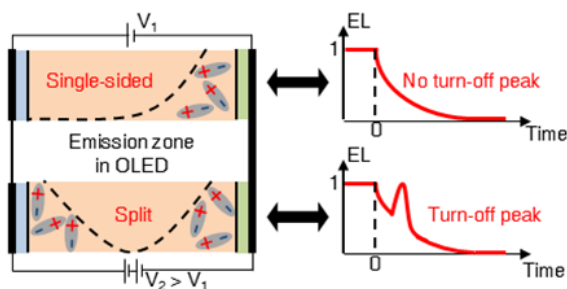
<https://pubs.acs.org/doi/abs/10.1021/acsami.8b09595>

Declaration of Contribution: Markus Regnat fabricated all the devices, carried out the device characterization, did the optoelectronic simulation, analysed the data and contributed to manuscript preparation.

Abstract

From s-polarized, angle-dependent measurements of the electroluminescence spectra in a three-layer phosphorescent organic light-emitting diode, we calculate the exciton distribution inside the 35 nm thick emission layer. The shape of the exciton profile changes with applied bias due to differing field dependencies of the electron and hole mobility. A split

emission zone with high exciton densities at both sides of the emission layer is obtained, which is explained by the presence of energy barriers and similar electron and hole mobilities. A peak in the transient electroluminescence signal after turn-off and the application of a reverse bias is identified as a signature of a split emission zone.



Introduction

Organic light-emitting diodes (OLEDs) nowadays reach high external quantum efficiencies of 30% and above^{1–5}, and they are commonly used in displays for smartphones, televisions, and increasingly as lighting elements. In general, a high luminance is desired, which can be achieved with high current densities. However, this driving condition often causes a reversible decrease of the efficiency^{6,7}. To optimize the layer stack for maximum light output, the knowledge of the emission zone (EMZ) inside the emission layer (EML) is essential. The location and extend of the emission zone is closely related to the current balance, i.e. where the charges accumulate and recombine both radiatively and non-radiatively, which limits the quantum efficiency of the OLED. Exciton confinement inside the EML is thus a key factor in optimizing OLED efficiency^{8–10}. The EMZ generally depends on the driving current and on the state of degradation, and it is affected by exciton quenching mechanisms if present.

Different techniques have been used to provide information about the emission zone, namely the use of sensing layers^{8,11–17} electro-optical simulations^{15,18–23}, as well as measuring and modelling the angle-dependent electroluminescence (EL)^{24–29}. In this work, we use the latter two techniques to investigate the changes in the EMZ with increasing current densities. Our findings reveal that the emission zone has two peaks at either side of the emission layer, and the maximum of this split emission zone shifts with applied bias. This split emission zone gives rise to an EL peak after the OLED is turned-off and reverse biased where the peak height depends on the forward voltage. To elucidate the EMZ from optical measurements, the OLED cavity has to be optically detuned in order to maximize the sensitivity of the angle-dependent signal to changes of the EMZ rather than to maximize the light output. The peak in the transient EL decay is also observed in an OLED stack optimized for light output, highlighting that split emission zones can be a general feature in OLEDs. With bottom-up electro-optical

simulations of an idealized OLED stack the finding of a split emission zone is directly linked with the appearance of the peak in the EL signal after turn-off.

Results and Discussion

The bottom-emission OLED stack under investigation is shown in **Figure 2.1** and comprises ITO (100 nm) / PEDOT:PSS (30 nm) / TCTA (46 nm) / CBP:Ir(ppy)₂(acac) (35 nm, 5 wt%) / NBPhen (52 nm or 120 nm) / Ca (15 nm) / Al (100 nm). The full material names are listed in the experimental section. The thickness of the NBPhen electron transport layer (ETL) of 52 nm in the optically tuned OLED maximizes the light output. To determine the emission zone in the thin EML from optical measurements, the ETL thickness was increased to 120 nm in the optically detuned OLED. The optical detuning maximizes the sensitivity of the angle-dependent s-polarized EL spectra to changes in the emission zone^{30,31} and reduces the measured current efficiency by a factor of 40. The thickness of the TCTA hole transporting layer (HTL) was kept constant, as its influence on the angular emission is minor.

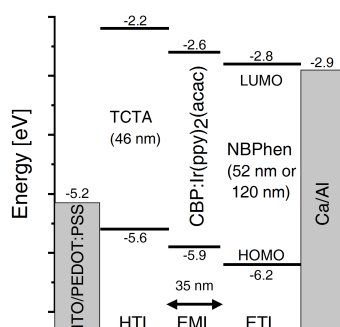


Figure 2.1 – Energy level diagram of the fabricated OLEDs. The emission layer is only 35 nm thin, and the thickness of the NBPhen layer is either 52 nm in the tuned OLED or 120 nm in the optically detuned OLED.

Split Emission Zone

Figure 2.2a shows the measured and simulated EL spectra for various angles at an intermediate current of 0.5 mA together with the photoluminescence (PL) spectrum of the Ir(ppy)₂(acac) dopant; **Figure S4.3** shows the spectra at 0.1 and 4 mA. The excellent agreement over the entire wavelength and viewing angle range was obtained with the emission zones shown in Figure 2.2c. For a constant current density, the EL spectrum changes with the viewing angle because the interference effect in the OLED cavity evolves with the viewing angle. For low angles, a peak near 520 nm is present, while at larger angles a second resonance appears in the EL spectrum near 570 nm. Consequently, the long-wavelength shoulder in the PL spectrum (Figure 2.2a) of the emitting species is pronounced at 70°. The evolution of the EL spectrum with current is shown in Figure 2.2b for a fixed angle of 30°. The long-wavelength shoulder around 570 nm in the normalized spectrum nearly vanishes for increasing currents.

This measured intensity decrease at 570 nm for increasing currents has to be associated with changes in the spatial distribution of the exciton density inside the EML and is, thus, a clear evidence that the emission zone changes with current.

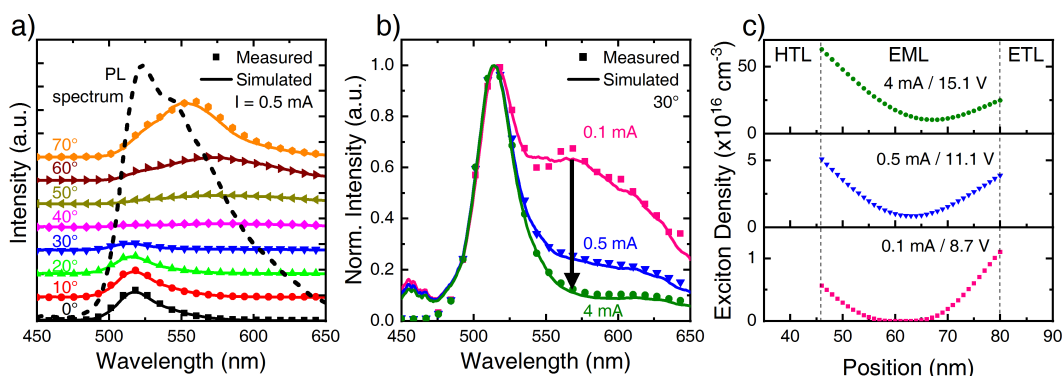


Figure 2.2 – Measured (symbols) and simulated (solid lines) angle-dependent s-polarized EL spectra for a constant current of 0.5 mA together with the PL spectrum of the Ir(ppy)₃(acac) dopant (a). Panel (b) shows the EL spectra at an angle of 30° for different currents. The shoulder at 570 nm is reduced significantly for increasing currents proving that the emission zone is changing with current. From these measurements, the optical model yields the emission zones shown in panel (c).

The emission zones calculated from angle-dependent measurements at all three current densities are shown in Figure 2.2c. High exciton densities are present at both interfaces of the EML. A split emission zone has also been reported in refs¹⁸ and³², whereas other OLED stacks can also show homogeneous or single sided emission zones as reported in e.g. refs¹³ and¹⁶. Having high emission at both EML interfaces indicates the presence of high electron and hole concentrations at both interfaces. This somewhat counter-intuitive observation can easily be rationalized by the presence of energy barriers for holes at the EML/ETL interface and for electrons at the HTL/EML interface as illustrated in Figure 3b. Without these energy barriers, no confinement of the unrecombined electrons and holes inside the EML takes place, and instead of forming a split emission zone the leakage currents would increase thus reducing the internal quantum efficiency. Electrical simulations of an idealized OLED further support and illustrate this explanation as discussed below.

The exciton distributions in Figure 2.2c show that the position of the highest emission intensity shifts from the EML/ETL to the HTL/EML interface for increasing current densities. A similar shift of the exciton density with current was observed by Coburn et al.¹³ in mCBP:Ir(dmp)₃ OLEDs by using sensing layers. At an intermediate current of 0.5 mA the exciton densities at both interfaces are equal and the emission zone is balanced. As discussed in detail below, this balance leads to the largest peak intensity in the transient EL signal when the OLED is reverse biased. We note that the observed shift of the emission zone maxima is caused by a different field dependence of the hole and the electron mobility, as discussed in the context of Figure 2.4.

Transient Electroluminescence

The biasing scheme for the transient electroluminescence measurements is illustrated in **Figure 2.3a**. After applying a certain forward voltage for a time long enough to reach steady state, the OLED is reverse biased with -10 V while the EL signal is measured. On top of the expected EL decay, a peak is observed that is caused by the split emission zone as shown in Figure 2.3c for the detuned OLED. This peak exceeds the steady-state value for voltages higher than 8 V. The peak appears approx. $0.5\mu\text{s}$ after turn-off and its intensity scales with on-voltages up to 11 V, before it decreases for larger forward voltages as shown in the inset to Figure 2.3c. The schematic energy diagram in Figure 2.3b illustrates the mechanism leading to this turn-off peak. Due to energy barriers between the EML and the neighboring HTL and ETL layers, electrons and holes that did not form excitons due to the low minority carrier density accumulate at the HTL/EML and the EML/ETL interface respectively. This leads to the observed split emission zone and to the turn-off peak, because these excess charge carriers drift toward each other upon applying the reverse bias and recombine when those charge carrier clouds meet. Without energy barriers at both EML interfaces, the leakage current would increase and no turn-off peak would be observed. The occurrence of a turn-off peak in the EL decay signal in reverse biased OLEDs is, thus, a clear signature of a split emission zone. A turn-off peak has also been observed in e.g. refs.³³ and³⁴, but without reporting a dependence on the emission zone profile and on driving conditions.

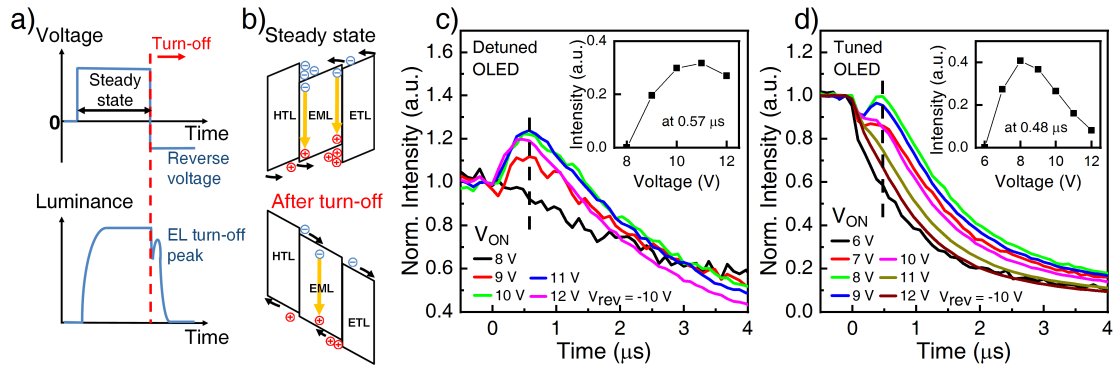


Figure 2.3 – (a) Biasing scheme for the transient electroluminescence measurements. (b) Illustration of the energy diagram highlighting the accumulation of excess electrons at the HTL/EML and of excess holes at the EML/ETL interface that drift toward each other under reverse bias, which leads to an increased recombination and the observed EL peak in detuned (c) and tuned (d) OLEDs. The insets show that this peak intensity increases with on-voltage up to a certain voltage before it decreases.

To demonstrate that a split emission zone can also be present in optimized OLEDs with maximized emission intensity, the transient EL signals of a tuned OLED are shown in Figure 2.3d. As in the detuned OLED, the same trend of the turn-off peak with an increasing intensity up to a certain on-voltage (V_{on}) is observed. As shown in the inset of Figure 2.3d, the maximum peak intensity occurs at a lower on-voltage of 8 V compared to 11 V for the detuned OLED, because

the voltage to reach the same ratio of excess charges is lower in the tuned OLED due to the decreased resistance of the thinner ETL layer^{35,36}. The average electric field in the tuned OLED for 8 V and in the detuned OLED for 11 V is similar (55 and 60 V/ μm) confirming the consistent behavior of the two OLEDs. Because the turn-off peak in transient EL measurements under reverse bias is also present in tuned OLEDs, we argue that the presence of such an EL turn-off peak is in general a signature of a split emission zone.

Electrical simulations of an idealized OLED

To further support the identification of the split emission zone from optical and transient EL measurements, we devised an electrical model for an idealized OLED stack. This illustrative example shows the requirements for the occurrence of a split emission zone, explains the observed EL turn-off peak, and sheds light on the physical mechanisms at work. The idealized OLED consists of the same three layers as the measured devices, but energy levels have been adapted to be aligned, except for the LUMO levels at the HTL/EML interface and for the HOMO levels at the EML/HTL interface as illustrated in **Figure 2.4a**. The model either employs a constant (cases I-III in **Figure 2.5**) or a field-dependent mobility model (case IV in **Figure 2.6**) to simulate the electronic and optical properties. To account for the high exciton densities at certain bias conditions, triplet-polaron quenching (TPQ) and triplet-triplet annihilation (TTA) have been investigated but showed no relevant effect on the formation of a split emission zone as discussed in case V (**Figure 2.7**) and VI (**Figure S2.2**).

Figure 2.4b shows the modelled energy band diagram in steady state under forward bias and right after applying a reverse bias of -4 V for equal electron and hole mobilities (case II). Under forward bias, electrons and holes accumulate at the respective interface of the EML due to the presence of an energy barrier of 700 meV. Not all charge carriers form excitons due to the low minority carrier density as discussed in detail below, and the excess charge carriers drift toward each other under reverse bias conditions as illustrated in **Figure 2.4b**. When those excess charge carrier clouds meet, they generate additional excitons that recombine and cause a peak in the transient EL signal after turn-off (c.f. **Figure 2.5d-f**). In the case of exactly balanced electron and hole densities in the EML (at all voltages), no excess charge carriers would accumulate at the respective interfaces and thus there would likely be no turn-off peak.

The detailed charge carrier profiles at 0 and 0.6 μs after turn-off are shown in **Figure 2.5a, d** and **g** for different combinations of hole and electron mobilities (cases I-III). **Figures 2.5b, e** and **h** show the temporal evolution of the emission zone at steady state and after turn-off, and **Figures 2.5c, f** and **i** show the resulting EL signal normalized to the steady state value under forward bias.

In case I (**Figure 2.5a-c**), the electron mobility in the EML and ETL is ten times higher than the hole mobility in the EML and HTL, which leads to a larger electron than hole density (**Figure 2.5a**). After exciton formation, a large number of excess electrons remains due to the lower hole density. These excess electrons accumulate at the HTL/EML interface and a single-sided emission zone is formed. We note that accumulation of electrons can extend into the HTL if

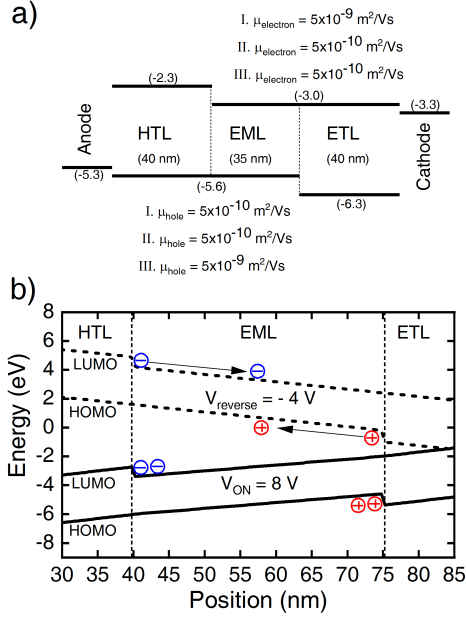


Figure 2.4 – (a) Energy levels and mobility values used in the idealized model of a tuned OLED for cases I-III. The band diagram in (b) illustrates the accumulation of excess electrons and holes at the respective EML interfaces at steady state. After reverse biasing, these excess electrons and holes migrate towards the center where they can generate additional excitons which leads to the observed peak in the transient EL signal.

the energy barrier is low, especially for a large electron mobility in the HTL. Upon applying a reverse bias, the excess electrons migrate towards the cathode, and because the hole density is much lower, the majority of electrons reach the cathode without forming excitons, while the holes migrate less due to the lower mobility. Therefore, the electroluminescence signal decays without a peak.

For case II in Figure 2.5d-f, the electron and hole mobilities are equal, and the excess electron and hole densities are identical at both EML interfaces. This leads to a nearly balanced exciton distribution with equal number of excitons at either side of the EML. Due to the Purcell effect, which increases the exciton decay rate near the metal cathode, the maximum exciton density is slightly higher at the anode side of the EML as can be seen in Figure 2.5e and by comparing Figure 2.5b and h. When the excess electrons and holes migrate toward the center of the EML under reverse bias (dotted lines in Figure 2.5d), a significant number of excitons is formed in the center of the EML (Figure 2.5e), leading to a pronounced peak in the transient electroluminescence (Figure 2.5f).

Case III (Figure 2.5g-i) is inverse to case I, and the higher hole mobility causes a higher hole than electron density in the EML, with excess holes at the EML/ETL interface. Under reverse bias, the excess holes migrate to the anode, and because there are no excess electrons, the electroluminescence decays without a peak.

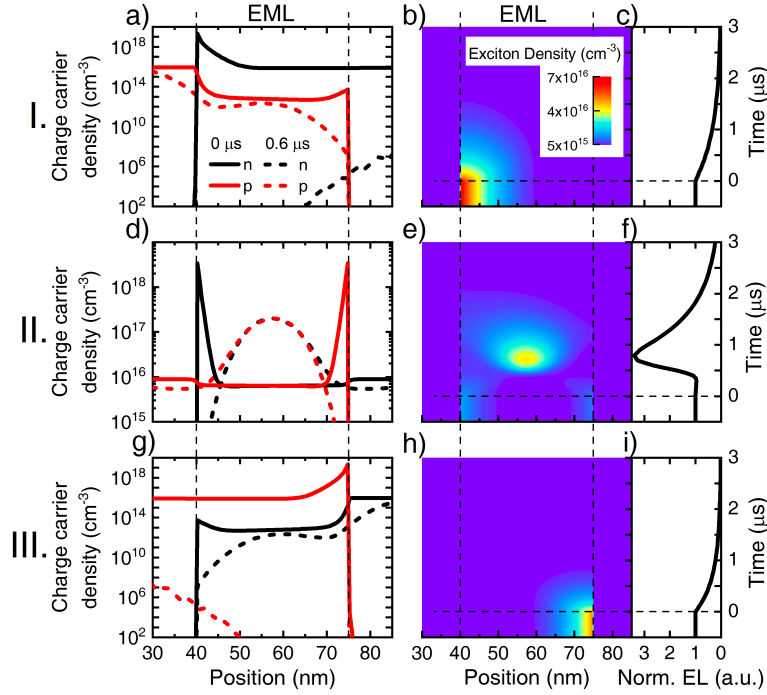


Figure 2.5 – Charge carrier profiles at 0 and 0.6 μs after turn-off (a), (d) and (g), temporal evolution of the emission zone (b), (e) and (h), and resulting EL signal (c), (f) and (i) for the three different electron and hole mobility combinations (cases I-III) in the ideal OLED. Under reverse bias, the excess charge carriers migrate toward the electrodes. In cases I and III, no excess minority charge carrier are present and the electroluminescence decays without a peak, while in case II, excess holes and electrons, present at both interfaces of the EML, form a significant number of excitons, which leads to the peak in the transient EL signal.

The simulations for cases I-III demonstrate that an EL turn-off peak is only observed if a split emission zone is formed. The split emission zone is formed when electron and hole mobilities are equal or similar, and energy barriers for electrons are present at the HTL/EML interface and for holes at the EML/ETL interface. The same behavior can be expected in non-ideal devices as long as electron and hole injection into the EML are equal or similar.

To explain the measured bias-dependent emission zone, the simulations for case IV used a different field dependence of the electron and the hole mobility. We argue that only a different field dependence leads to the observed bias-dependent emission zone. **Figure 2.6a** shows the electron and hole mobility for typical electric fields inside the OLED stack^{37,38}. An electric field exists at which both mobilities are equal, as in case II above, due to the different field dependencies. At higher fields, the electron mobility is larger than the hole mobility (case I), while at lower fields the situation is reversed (case III).

Figure 2.6b shows the exciton densities at three different voltages. At low external bias, the emission zone is located mainly at the EML/ETL interface, while at high bias the maximum

emission originates from the HTL/EML interface. At an intermediate bias, the exciton densities are nearly equal at both EML interfaces. This balanced and split emission zone leads again to the largest peak in the transient turn-off signal under reverse bias as shown in Figure 2.6c. The inset to Figure 2.6c shows the peak height of this turn-off peak for different on-voltages. The same behavior as in the measurements (Figure 2.3c, d) is observed, confirming that the exciton density is split and balanced on both sides of the EML for a bias of 11 V or 8 V for the detuned and tuned case, respectively. The different field-dependences of the electron and hole mobility are, thus, responsible for the changing emission zone with applied bias. If electron and hole mobilities had the same field-dependence, the ratio of the effective mobilities at different biases would be equal and no bias-dependent change of the emission zone would occur. We note that the exact condition for the appearance of the largest peak is a complex interplay between the mobility values, especially their field dependence, the energy barriers and the Purcell factor of the OLED cavity. Nevertheless, the maximum peak always occurs when the exciton density is nearly balanced at both EML interfaces.

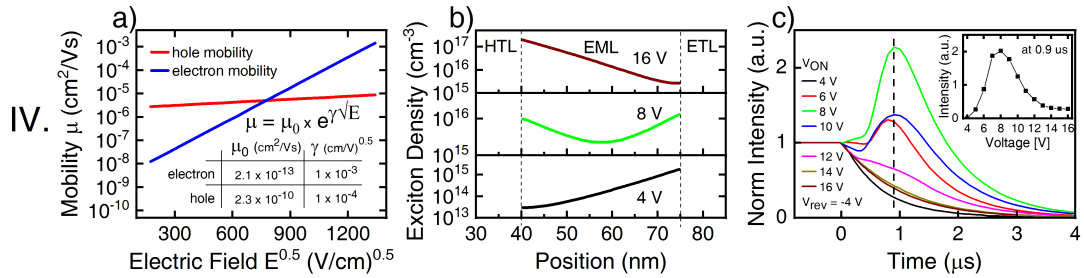


Figure 2.6 – Electron and hole mobilities used in the simulation plotted for typical electric fields (a) and simulated exciton densities for different biases (b). At an applied voltage of 8 V where both mobilities are equal, the split emission zone shows nearly balanced exciton densities at both EML interfaces, which results in the largest turn-off peak in the simulated transient EL signal (c).

The local charge carrier and exciton densities in the idealized OLEDs are in a range where triplet-polaron quenching (TPQ) or triplet-triplet annihilation (TTA) can become significant.³⁹ If these exciton quenching processes are considered in the simulations, the results remain qualitatively the same as shown for TPQ in **Figure 2.7** and for TTA in **Figure S2.2**. The exciton quenching leads to a faster EL decay (Figures 2.7a and S2.2a), but the peak in the transient EL signal under reverse bias appears at the same time as in the case without quenching and the maximum peak height is again obtained for an on-voltage of 8 V as expected.

The emission zone for the case considering exciton quenching is again single sided for low and for high applied bias, and is nearly balanced for an intermediate voltage that results in the largest EL turn-off peak (see Figure 2.7a and S2.2a). In comparison to Figure 2.6c, the exciton density in Figure 2.7b is lower due to exciton quenching, especially at high biases. The peak height in Figure 2.7a with exciton quenching appears larger than in Figure 2.6c without quenching, but this is due to the large effect of TPQ in steady state, which lowers the intensity used for normalization. The number of excess electrons and holes remains the

same irrespective of exciton quenching mechanisms, thus the number of additional excitons formed after turn-off remains essentially the same. Initial studies reveal a tendency that the measurements are better explained when exciton quenching mechanisms are included, and further studies are in progress to clarify the role of exciton quenching in those devices.

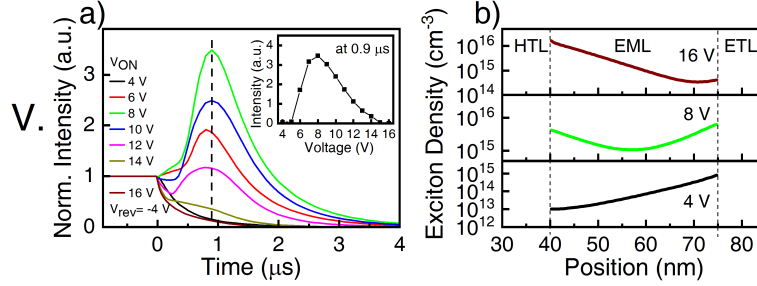


Figure 2.7 – Transient EL signal (a) and exciton densities (b) when triplet-polaron quenching is considered in the model. The same qualitative results as without quenching were obtained.

Conclusion

We have shown how measurements of angle-dependent EL spectra in optically detuned OLEDs reveal changes in the spatial distribution of the exciton density with applied bias in three-layer phosphorescent OLEDs. The emission zone obtained by solving the inverse problem on the basis of a dipole emission model can have two peaks at either side of the emission layer, and the maximum of this split emission zone shifts with applied bias due to differing field dependencies of the electron and hole mobility. A large excess charge density at both sides of the emissive layer leads to a pronounced electroluminescence peak after the OLED is reverse biased. The intensity of this turn-off peak depends on the extent of the split emission zone, and a bias dependence of the peak height implies changes of the split emission zone with forward voltage. Our findings are rationalized with electrical charge drift-diffusion device simulations and are largely unaffected by exciton quenching processes. The bias dependent split emission zone can also be present in optimized OLEDs that maximize light output.

Materials and Methods

OLED fabrication

For the fabrication of the OLEDs we used commercially available glass substrates structured with a 20 Ω/□ indium tin oxide (ITO) from Ossila. After cleaning in acetone and isopropanol in an ultrasonic bath, a 15 min UV-Ozone treatment was performed, directly followed by spin coating poly(3,4-ethylenedioxythiophene) polystyrene sulfonate (PEDOT:PSS, Clevis P VP AI 4083) with a spin speed of 3000 rpm. Before evaporating the organic materials, the substrates were annealed for 10 min at 160°C under nitrogen atmosphere in a glove box. The phosphorescent OLED stack consists of ITO (100 nm) / PEDOT:PSS (30 nm) / TCTA (46 nm)

/ CBP:Ir(ppy)₂(acac) (35 nm, 5 wt%) / NBPhen (52 or 120 nm) / Ca (15 nm) / Al (100 nm). The organic materials 4,4',4''-Tris(carbazol-9-yl)triphenylamine (TCTA), 4,4'-Bis(carbazol-9-yl)biphenyl (CBP), Bis(2-phenylpyridine)(acetylacetonate)iridium(III) (Ir(ppy)₂(acac)) and 2,9-Bis(naphthalen-2-yl)-4,7-diphenyl-1,10-phenanthroline (NBPhen) were purchased from Lumtec and were evaporated under high vacuum of $< 10^{-6}$ mbar without any prior purification. TCTA was used as hole transport layer (HTL) and electron blocking layer due to its higher lowest unoccupied molecular orbital (LUMO) level than the CBP LUMO level. NBPhen was used as electron transport layer (ETL), which has a good hole blocking property due to its low-lying highest occupied molecular orbital (HOMO) compared to the HOMO level of CBP. The energy levels with values taken from literature^{20,40,41} are shown in Figure 2.1. The phosphorescent emitter Ir(ppy)₂(acac) was co-evaporated with the CBP host to obtain a concentration of ≈ 5 wt%. For the evaporation of the Ca/Al cathode the shadow masks were exchanged, and the samples were exposed to N₂. After fabrication, the OLEDs were encapsulated using an encapsulation epoxy and a cover glass from Ossila under nitrogen atmosphere. The optical and electrical characterization took place in air, and the active area of the OLED pixels is 0.045 cm².

EL measurements

The angle-dependent s-polarized EL spectra were measured in a home-built setup consisting of a half cylinder lens, a rotational stage with a detector unit comprising pinhole, polarizer, retarder and a ULS2048L spectrometer (Avantes). The angular measurement range is from -70° to +70° w.r.t the surface normal, and with a 1 mm diameter pinhole an angular resolution of less than $\pm 1^\circ$ is achieved. The setup is connected with the all-in-one measurement system Paios from Fluxim^{42,43} and a redesigned version of the setup is now available as the angular luminescence spectrometer Phelos by Fluxim. The half cylinder lens out-couples all substrate modes to air and thus allows to measure the entire angle-dependent EL spectra in the glass substrate. A gated Hamamatsu photosensor module (H11526-110) attached to Paios was used to measure the time-dependent EL decay.

Calculating the emission zone

To calculate the shape of the emission zone from measured angle-dependent s-polarized EL spectra, the optical dipole emission model of the Setfos 4.6 software by Fluxim was used⁴⁴, which implements a fit algorithm previously introduced and evaluated by Peruccio et al.^{21,22,29} and by Jenatsch et al.⁴⁵. The algorithm uses a superposition of delta-like emitters equally distributed inside the emission layer and adapts their height to minimize the difference between measured and simulated EL spectra and also extracts the PL spectrum of the emitter (cf. Figure 2.2a). The preferential horizontal alignment of the Ir(ppy)₂(acac) emitter molecule was set to be 77 % horizontal^{1,46}. To calculate the exciton density from the measured radiative dipole density, the same radiative exciton decay rate as in the electrical OLED model was used. With this approach, the shape of the emission zone can be determined from optical measurements using a purely optical model.

Electrical OLED model

The electrical simulations were performed with the software Setfos 4.6⁴⁴, which solves the drift-diffusion equations for electron and holes, considers exciton formation, diffusion and decay in the framework of radiating dipoles inside a cavity including the Purcell effect²³. Either constant or field-dependent electron and hole mobilities according to the Poole-Frenkel model with $\mu(E) = \mu_0 e^{\gamma\sqrt{E}}$ were used²³. The chosen HOMO/LUMO values are close to the ones displayed in Figure 2.1, and the boundary conditions for the charge carrier densities at the electrodes were set to satisfy Fermi-level alignment at thermal equilibrium. Exciton generation is only permitted in the emission layer and follows the standard Langevin-recombination²¹. Exciton recombination was modelled with a non-radiative decay rate of $0.09 \mu s^{-1}$ and a radiative decay rate of $0.63 \mu s^{-1}$, resulting in a quantum efficiency of 87% and an exciton lifetime of $1.39 \mu s$ as reported for similar systems^{3,47,48}. The exciton diffusion coefficient was set to $63 nm^2/\mu s$ which results in an exciton diffusion length of $9 nm$ as observed in the optical measurements. If larger exciton diffusion coefficients were used, the exciton distribution inside the EML is smeared out, and for very large values, the split emission zone can even disappear. The excitons were confined to the EML because the triplet energy of TCTA (2.8 eV)⁴⁹ is larger than that of Ir(ppy)₂(acac) (2.4 eV)⁴⁹, which prevents exciton transport into the HTL. The reported triplet energy for NBPhen (2.2 eV)⁴⁰ allows exciton transport into the ETL, but the exciton transport into the ETL is expected to be only a few percent¹³ and was thus neglected. For emitters with high triplet energy levels exciton transport should be considered. The organic-organic interfaces assume quasi-Fermi level alignment and use Boltzmann statistics to calculate the charge carrier densities in the OLED stack. For the results shown in Figure 2.7 and Figure S2.2, exciton quenching was modeled as triplet-polaron quenching or triplet-triplet annihilation with quenching rates of $5 \cdot 10^{-12} cm^3/s$ taken from refs³⁹ and⁴⁷.

References

1. Kim, K.-H., Moon, C.-K., Lee, J.-H., Kim, S.-Y. & Kim, J.-J. Highly Efficient Organic Light-Emitting Diodes with Phosphorescent Emitters Having High Quantum Yield and Horizontal Orientation of Transition Dipole Moments. *Advanced Materials* **26**. 00043, 3844–3847 (2014).
2. Kim, K.-H. *et al.* Phosphorescent dye-based supramolecules for high-efficiency organic light-emitting diodes. *Nature Communications* **5**, 4769. <http://www.nature.com/ncomms/2014/140910/ncomms5769/full/ncomms5769.html> (Sept. 10, 2014).
3. Park, Y.-S. *et al.* Exciplex-Forming Co-host for Organic Light-Emitting Diodes with Ultimate Efficiency. *Advanced Functional Materials* **23**. 00067, 4914–4920 (2013).
4. Tanaka, D. *et al.* Ultra High Efficiency Green Organic Light-Emitting Devices. *Japanese Journal of Applied Physics* **46**, L10 (Dec. 22, 2006).

5. Udagawa, K., Sasabe, H., Cai, C. & Kido, J. Low-Driving-Voltage Blue Phosphorescent Organic Light-Emitting Devices with External Quantum Efficiency of 30%. *Advanced Materials* **26**, 5062–5066 (Aug. 1, 2014).
6. Murawski, C., Leo, K. & Gather, M. C. Efficiency Roll-Off in Organic Light-Emitting Diodes. *Advanced Materials* **25**. 00088, 6801–6827 (Dec. 1, 2013).
7. Tsutsui, T. & Takada, N. Progress in Emission Efficiency of Organic Light-Emitting Diodes: Basic Understanding and Its Technical Application. *Japanese Journal of Applied Physics* **52**. 00009, 110001. <http://iopscience.iop.org/1347-4065/52/11R/110001> (Nov. 1, 2013).
8. Erickson, N. C. & Holmes, R. J. Investigating the Role of Emissive Layer Architecture on the Exciton Recombination Zone in Organic Light-Emitting Devices. *Advanced Functional Materials* **23**, 5190–5198 (Nov. 6, 2013).
9. Jeon, S. K. & Lee, J. Y. Direct monitoring of recombination zone shift during lifetime measurement of phosphorescent organic light-emitting diodes. *Journal of Industrial and Engineering Chemistry* **32**, 332–335. <http://www.sciencedirect.com/science/article/pii/S1226086X15004207> (Dec. 25, 2015).
10. Jesuraj, P. J. *et al.* Recombination Zone Control without Sensing Layer and the Exciton Confinement in Green Phosphorescent OLEDs by Excluding Interface Energy Transfer. *The Journal of Physical Chemistry C* **122**, 2951–2958 (Feb. 8, 2018).
11. Aminaka, E.-i., Tsutsui, T. & Saito, S. Effect of layered structures on the location of emissive regions in organic electroluminescent devices. *Journal of Applied Physics* **79**, 8808–8815 (June 1, 1996).
12. Beierlein, T. A. *et al.* Investigation of internal processes in organic light-emitting devices using thin sensing layers. *Synthetic Metals. Organic Materials for Device Applications. Proceedings of Symposium F, E-MRS Spring Meeting 2002, June 18-21, 2002, Strasbourg, France* **138**. 00026, 213–221. <http://www.sciencedirect.com/science/article/pii/S0379677902012699> (June 2, 2003).
13. Coburn, C., Lee, J. & Forrest, S. R. Charge Balance and Exciton Confinement in Phosphorescent Organic Light Emitting Diodes. *Advanced Optical Materials* **4**, 889–895 (June 1, 2016).
14. Li, C., Tsuboi, T. & Huang, W. Recombination zone in organic light emitting diodes with emitting layer of diphenylanthracene-derivative host. *Physics Procedia. 9th International Conference on Nano-Molecular Electronics* **14**, 213–216. <http://www.sciencedirect.com/science/article/pii/S1875389211003130> (Supplement C Jan. 1, 2011).
15. Ruhstaller, B. *et al.* Simulating electronic and optical processes in multilayer organic light-emitting devices. *IEEE Journal of Selected Topics in Quantum Electronics* **9**, 723–731 (May 2003).
16. Sim, B., Moon, C.-K., Kim, K.-H. & Kim, J.-J. Quantitative Analysis of the Efficiency of OLEDs. *ACS Applied Materials & Interfaces* **8**. 00000, 33010–33018 (Dec. 7, 2016).
17. Zhang, Y., Lee, J. & Forrest, S. R. Tenfold increase in the lifetime of blue phosphorescent organic light-emitting diodes. *Nature Communications* **5**. 00010, 5008 (Sept. 25, 2014).

18. Eersel, H. v., Bobbert, P. A., Janssen, R. a. J. & Coehoorn, R. Effect of Förster-mediated triplet-polaron quenching and triplet-triplet annihilation on the efficiency roll-off of organic light-emitting diodes. *Journal of Applied Physics* **119**, 163102 (Apr. 28, 2016).
19. Van Eersel, H., Bobbert, P. A., Janssen, R. a. J. & Coehoorn, R. Monte Carlo study of efficiency roll-off of phosphorescent organic light-emitting diodes: Evidence for dominant role of triplet-polaron quenching. *Applied Physics Letters* **105**, 143303 (Oct. 6, 2014).
20. Mesta, M. *et al.* Molecular-scale simulation of electroluminescence in a multilayer white organic light-emitting diode. *Nature Materials* **12**, 652–658. <http://www.nature.com/nmat/journal/v12/n7/full/nmat3622.html> (July 2013).
21. Perucco, B. *et al.* On the exciton profile in OLEDs-seamless optical and electrical modeling. *Organic Electronics* **13**, 1827–1835. <http://www.sciencedirect.com/science/article/pii/S1566119912002534> (Oct. 1, 2012).
22. Perucco, B., Reinke, N. A., Müller, F., Rezzonico, D. & Ruhstaller, B. *The influence of the optical environment on the shape of the emission profile and methods of its determination* in *Organic Photonics IV* (eds Heremans, P. L., Coehoorn, R. & Adachi, C.) **7722**. 00002 (Proc. of SPIE, Apr. 2010), 77220F1. (2016).
23. Ruhstaller, B. *et al.* in *Optoelectronic Devices and Properties, edited by Oleg Sergiyenko, ISBN 978-953-307-204-3, DOI: 10.5772/14626 00009* (2011). (2017).
24. Carvelli, M., Janssen, R. A. J. & Coehoorn, R. Spatial resolution of methods for measuring the light-emission profile in organic light-emitting diodes. *Journal of Applied Physics* **110**, 0845121 (Oct. 15, 2011).
25. Danz, N. *et al.* Detection of sub-10 nm emission profile features in organic light-emitting diodes using destructive interference. *Optics Letters* **37**, 4134–4136. <http://www.osapublishing.org/abstract.cfm?uri=ol-37-19-4134> (Oct. 1, 2012).
26. Flämmich, M. *et al.* Orientation of emissive dipoles in OLEDs: Quantitative in situ analysis. *Organic Electronics* **11**. 00000, 1039–1046. <http://www.sciencedirect.com/science/article/pii/S1566119910000856> (June 2010).
27. Ciarnain, R. M. *et al.* Emission from outside of the emission layer in state-of-the-art phosphorescent organic light-emitting diodes. *Organic Electronics* **44**, 115–119. <http://www.sciencedirect.com/science/article/pii/S1566119917300605> (May 2017).
28. Mensfoort, S. L. M. v. *et al.* Measuring the light emission profile in organic light-emitting diodes with nanometre spatial resolution. *Nature Photonics* **4**. 00052, 329–335. <http://www.nature.com/nphoton/journal/v4/n5/full/nphoton.2010.32.html> (May 2010).
29. Perucco, B., Reinke, N. A., Rezzonico, D., Moos, M. & Ruhstaller, B. Analysis of the emission profile in organic light-emitting devices. *Optical Society of America* **18**. 00013, A246. http://www.opticsinfobase.org/view_article.cfm?gotourl=http%3A%2F%2Fwww%2Eopticsinfobase%2Eorg%2FDirectPDFAccess%2FBD2DC44F%2DDC94%2DF2EE%2D639CB01A65261B00%5F202487%2Foe%2D18%2DS2%2DA246%2Epdf%3Fda%3D1%26id%3D202487%26seq%3D0%26mobile%3Dno&org= (S2 June 21, 2010).

30. Flämmich, M., Michaelis, D. & Danz, N. *In situ measurement of spectrum, emission zone, and dipole emitter orientation in OLEDs in Light-Emitting Diodes: Materials, Devices, and Applications for Solid State Lighting XV* (eds Streubel, K. P., Jeon, H., Tu, L.-W. & Linder, N.) **7954** (Proc. of SPIE, Feb. 2011), 7954101. (2016).
31. Flämmich, M., Michaelis, D. & Danz, N. Accessing OLED emitter properties by radiation pattern analyses. *Organic Electronics* **12**. 00016, 83–91. <http://www.sciencedirect.com/science/article/pii/S1566119910003216> (Jan. 2011).
32. Coehoorn, R., van Eersel, H., Bobbert, P. & Janssen, R. Kinetic Monte Carlo Study of the Sensitivity of OLED Efficiency and Lifetime to Materials Parameters. *Advanced Functional Materials* **25**. 00003, 2024–2037 (Apr. 1, 2015).
33. Song, D., Zhao, S., Luo, Y. & Aziz, H. Causes of efficiency roll-off in phosphorescent organic light emitting devices: Triplet-triplet annihilation versus triplet-polaron quenching. *Applied Physics Letters* **97**. 00056, 243304 (Dec. 13, 2010).
34. Reineke, S. *et al.* Measuring carrier mobility in conventional multilayer organic light emitting devices by delayed exciton generation. *physica status solidi (b)* **245**, 804–809 (May 1, 2008).
35. Bhansali, U. S. *et al.* Controlling the carrier recombination zone for improved color stability in a two-dopant fluorophore/phosphor white organic light-emitting diode. *Applied Physics Letters* **94**, 203501 (May 18, 2009).
36. Lee, W. H. *et al.* Improvement of charge balance, recombination zone confinement, and low efficiency roll-off in green phosphorescent OLEDs by altering electron transport layer thickness. *Materials Research Express* **5**, 076201. <http://stacks.iop.org/2053-1591/5/i=7/a=076201> (2018).
37. Lee, S.-B., Yasuda, T., Yang, M.-J., Fujita, K. & Tsutsui, T. Charge Carrier Mobility in Vacuum-Sublimed Dye Films for Light-Emitting Diodes Studied by the Time-of-Flight Technique. *Molecular Crystals and Liquid Crystals* **405**, 67–73 (Jan. 1, 2003).
38. Parshin, M. A., Ollevier, J. & der Auweraer, M. V. *Charge carrier mobility in CBP films doped with Ir(ppy)₃ in Organic Optoelectronics and Photonics II* (eds Heremans, P. L., Muccini, M. & Meulenkaamp, E. A.) **6192** (Proc. of SPIE, Apr. 21, 2006), 61922A1. <http://proceedings.spiedigitallibrary.org/proceeding.aspx?doi=10.1117/12.663553> (2017).
39. Reineke, S., Walzer, K. & Leo, K. Triplet-exciton quenching in organic phosphorescent light-emitting diodes with Ir-based emitters. *Physical Review B* **75**. 00375, 125328 (Mar. 28, 2007).
40. Yamazaki, S. & Tsutsui, T. *Physics and Technology of Crystalline Oxide Semiconductor CAAC-IGZO: Application to Displays* Google-Books-ID: 11B7DQAAQBAJ. 444 pp. ISBN: 978-1-119-24745-6. <https://www.amazon.com/Physics-Technology-Crystalline-Semiconductor-CAAC-IGZO/dp/1119247454?SubscriptionId=AKIAIOBINVZYXZQZ2U3A&tag=chimbori05-20&linkCode=xm2&camp=2025&creative=165953&creativeASIN=1119247454> (John Wiley & Sons, Feb. 6, 2017).

41. Zhang, D. *et al.* Low efficiency roll off at high current densities in Ir-complex based electrophosphorescence diode with exciton diffusing and fluorescence compensating layers. *Applied Physics Letters* **91**, 183516 (Oct. 29, 2007).
42. *Platform for All-In-One Characterization of Solar Cells and OLEDs, Software version Paios 3.3, Fluxim* <https://www.fluxim.com/paios>.
43. *Characterization Suite Fluxim*. <https://www.fluxim.com/news/2018/5/4/characterization-suite-41-released> (2019).
44. *Setfos 4.6, Fluxim* Fluxim. 00000. <https://www.fluxim.com/setfos-intro/>.
45. Jenatsch, S. *et al.* Time-Dependent p-i-n Structure and Emission Zone in Sandwich-Type Light-Emitting Electrochemical Cells. *ACS Photonics* **5**, 1591–1598. <https://doi.org/10.1021/acsp Photonics.8b00047> (2018) (Apr. 2018).
46. Liehm, P. *et al.* Comparing the emissive dipole orientation of two similar phosphorescent green emitter molecules in highly efficient organic light-emitting diodes. *Applied Physics Letters* **101**, 00052, 253304 (Dec. 17, 2012).
47. Kalinowski, J. *et al.* Quenching effects in organic electrophosphorescence. *Physical Review B* **66**, 235321 (Dec. 31, 2002).
48. Wehrmeister, S. *et al.* Combined Electrical and Optical Analysis of the Efficiency Roll-Off in Phosphorescent Organic Light-Emitting Diodes. *Physical Review Applied* **3**, 00002, 024008 (Feb. 19, 2015).
49. Sun, N. *et al.* High-Performance Hybrid White Organic Light-Emitting Devices without Interlayer between Fluorescent and Phosphorescent Emissive Regions. *Advanced Materials* **26**, 1617–1621 (Mar. 1, 2014).

ACKNOWLEDGMENT

We thank L. Penninck, S. Altazin and S. Jenatsch from Fluxim, T. Beierlein from ZHAW and F. Nüesch from EPFL for fruitful discussions and valuable comments.

ABBREVIATIONS

EL, electroluminescence; EML, emission layer; EMZ, emission zone; ETL, electron transport layer; HOMO, highest occupied molecular orbital; HTL, hole transport layer; LUMO, lowest unoccupied molecular orbital; OLED, organic light emitting diode; PL, photoluminescence; TPQ, triplet-polaron quenching.

2.1 Supporting Information

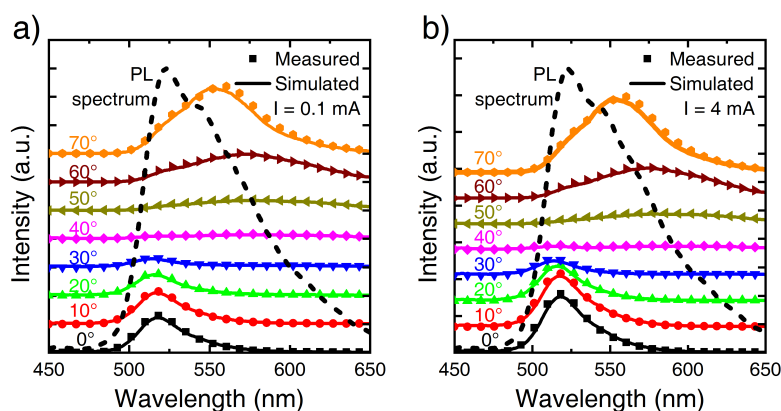


Figure S2.1 – Measured (symbols) and simulated (solid lines) angle-dependent s-polarized EL spectra for a constant current of 0.1 mA (a) and 4 mA (b) together with the PL spectrum of the $\text{Ir(ppy)}_2\text{(acac)}$ emitter molecule.

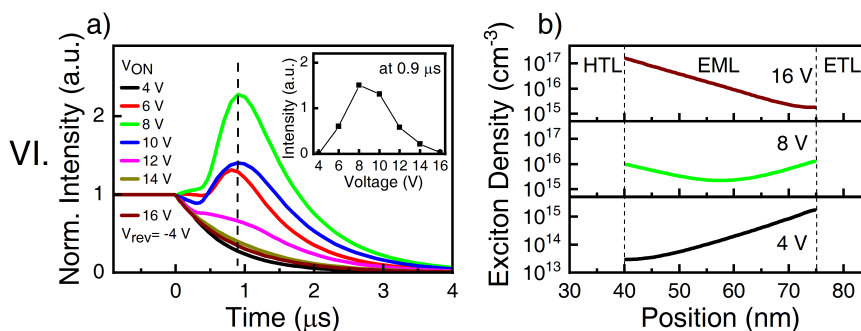


Figure S2.2 – Transient EL signal (a) and exciton densities (b) when triplet-triplet annihilation is considered in the model (case VI). The same qualitative results were obtained as with triplet-polaron quenching (cf. Fig. 2.7) and without exciton quenching (cf. Fig. 2.6).

3 Emission Zone Influence on Exciton Quenching and Efficiency

Influence of the Bias-dependent Emission Zone on Exciton Quenching and OLED Efficiency

Markus Regnat^{a,b}, Kurt P. Pernstich^a, Beat Ruhstaller^{a,c}

^aZurich University of Applied Sciences ZHAW, Institute of Computational Physics, Technikumstrasse 9, 8401 Winterthur, Switzerland

^bInstitut des Matériaux, Ecole Polytechnique Fédérale de Lausanne, EPFL, Station 12, 1015 Lausanne, Switzerland

^cFLUXIM AG, Technoparkstrasse 2, 8406 Winterthur, Switzerland

Reprinted with permission from Organic Electronics Journal.

Copyright 2019 Elsevier B.V.

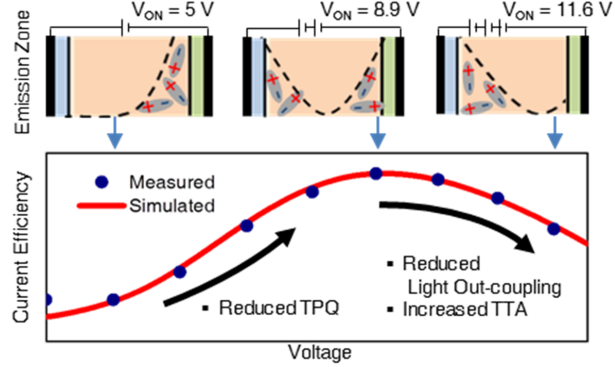
Organic Electronic, Volume 70, July 2019, Pages 219-226, Doi:10.1016/j.orgel.2019.04.027

<https://doi.org/10.1016/j.orgel.2019.04.027>

Declaration of Contribution : Markus Regnat fabricated all the devices, carried out the device characterization, did the optoelectronic simulation, analysed the data and contributed to manuscript preparation.

Abstract

We present an electro-optical model of a three-layer phosphorescent OLED which accurately describes the measured current efficiency and transient electroluminescence decay for different biases. Central findings are a bias-dependent emission zone, which influences light outcoupling as well as exciton quenching, and the presence of strong triplet-polaron quenching even at low bias. The measured current efficiency initially increases up to 9 V before it decreases, where the increase is found to be caused by reduced triplet-polaron quenching with holes, while the decrease is caused by a reduced light outcoupling and increased triplet-triplet annihilation. The numerical model allows identifying the individual contributions of the exciton continuity equation and explains the electroluminescence decay, which deviates significantly from a mono-exponential decay due to the dominating influence of exciton generation and quenching after the external bias is removed.



Introduction

Over the last years OLED efficiencies increased up to nearly 40% due to the use of orientated phosphorescent^{1–4} and TADF emitters^{5–8} with internal quantum efficiencies close to 100%. Including different light scattering strategies for improved light outcoupling from the OLED stack, remarkable EQEs up to 62% were achieved^{9–11}. Besides reaching high efficiencies, a major challenge for realizing OLEDs with high luminous intensities is still the efficiency roll-off at high biases due to exciton quenching processes, namely triplet-polaron quenching (TPQ) and/or triplet-triplet annihilation (TTA)^{12,13}.

To improve further the light emission at high biases, a better understanding of the underlying mechanisms, especially at high biases, is necessary. An important OLED characterization parameter is the current efficiency (CE)^{14–16}, which gives the ratio of the photometric measure luminance L to the applied current density j .

$$CE = \frac{L}{j} \quad (3.1)$$

In this study, we show that a bias-dependent position of the emission zone has an influence on the CE, as well as on the electroluminescence (EL) decay. Direct experimental evidence

of a bias-dependent emission zone in the investigated OLED from optical measurements was presented by us recently¹⁶. In the work presented here, an elaborate electro-optical model is parametrized to describe quantitatively the measured current-voltage-luminance, the current efficiency, and the transient electroluminescent decay. This model also shows a strong bias dependence of the emission zone and further reveals that significant exciton quenching occurs already at low bias and that the strength of exciton quenching is influenced by the bias-dependent emission zone. Only with a combination of a bias-dependent emission zone - which influences the light outcoupling as well as exciton quenching - the observed trends in CE and EL decay can be explained.

Our study sheds light on the interplay between the position of the emission zone and exciton quenching, and highlights the importance of considering the details of the emission zone, particularly a possible bias dependence, when optimizing OLED efficiency.

Experimental

OLED fabrication

The investigated phosphorescent OLED stack (see inset to Figure 3.1) consists of indium tin oxide ITO (100 nm)/ PEDOT:PSS (30 nm)/ TCTA (46 nm)/ CBP:Ir(ppy)₂(acac) (35 nm, 5 wt%)/ NBPhen (52 nm)/Ca (15 nm)/Al (100 nm). The organic materials poly(3,4-ethylenedioxythiophene): polystyrene sulfonate (PEDOT:PSS), 4,4',4''-tris(carbazol-9-yl) triphenylamine (TCTA), 4,4'-bis(carbazol-9-yl)biphenyl (CBP), bis(2-phenylpyridine) (acetylacetonate) iridium(III) (Ir(ppy)₂(acac)) and 2,9-bis(naphthalen-2-yl)-4,7-diphenyl-1,10-phenanthroline (NBPhen) were purchased from Heraeus CleviosTM and Lumtec. The glass substrates with patterned ITO anode were purchased from Ossila Ltd. The substrates were cleaned with acetone and isopropanol in an ultrasonic bath and afterwards for 15 min with UV-ozone. A 30 nm thick PEDOT:PSS film was spin coated in air and subsequently heated in a glovebox for 40 min at 150 °C. All organic layers were deposited in high vacuum ($< 10^{-6}$ mbar) by thermal sublimation. For the emission layer Ir(ppy)₂(acac) and CBP were co-evaporated. Prior to the cathode deposition, the shadow masks were exchanged under nitrogen atmosphere to obtain a pixel area of 4.5 mm². After film deposition, the OLEDs were encapsulated under nitrogen atmosphere.

Measurements

The electro-optical measurements were performed with the all-in-one measurement system Paios and the characterization suite 4.12 from Fluxim^(17,18). To measure the luminance a gated photomultiplier tube (PMT H11526 Series) from Hamamatsu was employed and controlled with Paios. The PMT output voltage V_{PMT} is directly proportional to the luminance because the electroluminescence (EL) spectrum is bias-independent, thus the PMT signal can be easily converted into luminance with the luminous sensitivity of the PMT. The acceptance angle of the PMT was $\approx \pm 10^\circ$, and the measured luminance is proportional to the luminance at 0° to

the surface normal (as obtained from the simulations) because the angular emission spectrum is essentially independent of the bias. To measure the J-V-L characteristics, voltage pulses with magnitudes from 4 to 12 V were applied to the OLED while measuring the current density j and the luminance L . The length of the voltage pulses was set to 200 μs in order to reach steady state, and the values for j and L were averaged over the last 20 μs of each pulse. For the transient EL decay measurements the on-voltage was applied for 200 μs before turning-off the OLED by applying 0 V. The JV characteristics was also measured using a higher precision, stepwise voltage ramp with longer integration time to obtain the J-V curve over the entire bias range.

Electro-optical Model

Electro-optical simulations were carried out with a preview version of Setfos 5.0 (Fluxim)¹⁹. Setfos calculates the position- and time-dependent charge carrier density distribution, exciton generation, diffusion and decay, and outcoupling of photons^{20,21}. In the electro-optical model, the exciton generation occurs via Langevin recombination inside the emission layer (EML), and exciton diffusion is limited to the EML. Generation of photons from radiatively decaying excitons considers the Purcell effect^{21,22}. Mode analysis was used to divide the generated photons into photons that are absorbed, emitted and dissipated in evanescent, substrate and guided mode²¹. Mode analysis in Setfos considers emission either into the entire hemisphere or into a restricted angular range. An angular range of $\pm 10^\circ$ was used to be able to compare the emitted photons with the measured luminance. To explain the measurements, we had to include multiple exciton quenching mechanisms in the model, namely triplet-polaron quenching for holes (TPQh) and for electrons (TPQe) as well as triplet-triplet annihilation (TTA). All model parameters are listed in table S3.1.

Optimization of the model parameters

A pattern search optimization algorithm with a genetic search routine implemented in Matlab was used to optimize the model parameters to obtain a good agreement between simulations and measurements. In each iteration, the optimizer started Setfos to calculate the electro-optical characteristics (current density - voltage (J-V), current efficiency (CE) and transient electroluminescence (EL)), which were used to calculate the goodness of fit. The initial values and reasonable bounds for the model parameters were taken or estimated from literature^{23–31}. Out of the 35 model parameters, 20 were allowed to vary (see table S3.1).

Despite the large number of free model parameters, we estimate that the obtained solution is close to a global optimum, because many of the parameter clusters influence only a certain subset of the dataset and, thus, they cannot be changed independently. While the simultaneous use of three different measurement types (J-V-L, CE, transient EL) in the fit prolongs the optimization process, they help, at the same time, to arrive closer to a global solution. As was demonstrated in an earlier study³², the use of datasets from multiple measurement types is advised as it reduces the correlation among the model parameters.

Result and Discussion

Figure 3.1a shows the measured and simulated current density and luminance for different applied biases. The J-V curve was measured in pulsed and stepwise mode as described in the experimental section. The step-wise measured JV curve shows a slightly higher current at high voltages than the pulsed measurement, possibly due to self-heating³³. The measured and simulated values agree very well, indicating the high quality of the model, and the inset to Figure 3.1a shows the layer stack of the phosphorescent OLED. Figure 3.1b shows the measured and simulated current efficiency (CE).

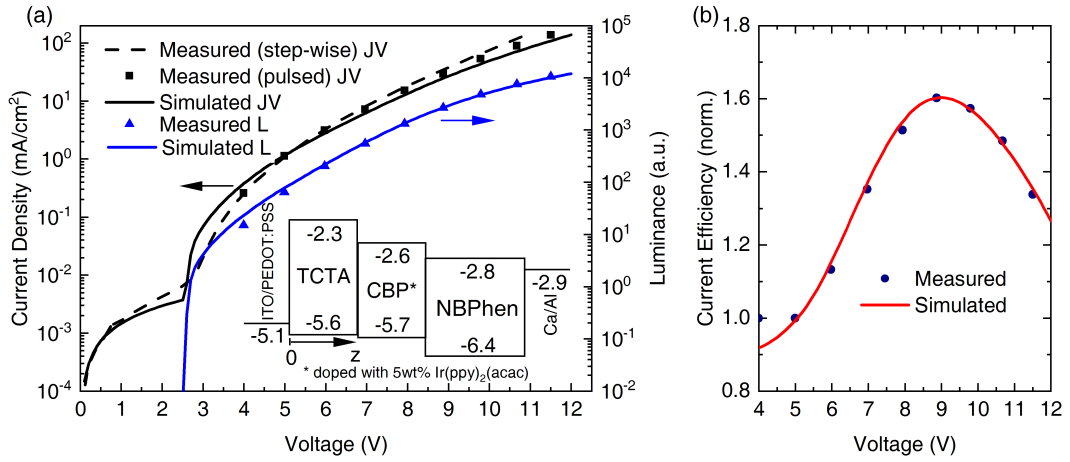


Figure 3.1 – Measured and simulated current density - voltage - luminance characteristic (a) and measured and simulated current efficiency for increasing bias (b) of the investigated OLED. The inset in (a) shows the OLED layer stack.

The large increase of the current efficiency between 5 V and 9 V is somewhat unexpected and can only be explained by considering a bias-dependent change of the emission zone and its influence on the exciton quenching contributions, as discussed in detail below. An increase in CE and EQE has been reported before^{34–37} and was explained by a non-constant charge balance³⁷, which agrees with the findings presented here. The decreasing CE at large bias can only be explained by considering exciton quenching as well as the bias-dependent change of the emission zone, which leads to a reduced light outcoupling at high bias as discussed next.

Influence of the emission zone on light outcoupling

In the electro-optical model, the luminance at 0° to the surface normal is calculated from (Manual Setfos 4.6, Fluxim, n.d.):

$$L = 683 \frac{\text{lm}}{\text{W}} \cdot \int \bar{y}(\lambda) \cdot \frac{1}{2p} \cdot E_{\gamma}(\lambda) \cdot \Lambda(\lambda) \cdot \int N_{\gamma}(z) \cdot g(z, \lambda) dz d\lambda. \quad (3.2)$$

The value of 683 lm/W is the maximum of the luminous efficacy, $\bar{y}(\lambda)$ is the dimensionless photopic luminosity function, $E_{\gamma}(\lambda)$ is the photon energy, and $\Lambda(\lambda)$ the intrinsic lumines-

cence spectrum of the emitting species. $N_\gamma(z)$ is the position-dependent number of photons generated from the emitting dipoles, and $g(z, \lambda)$ accounts for the optical feedback of the OLED micro cavity on the emitting dipoles including the effects of evanescent and guided modes, interference, light trapping due to total internal reflection as well as absorption in the individual layers (Manual Setfos 4.6, Fluxim, n.d.).

To describe the influence of the bias-dependent emission zone on light outcoupling, we introduce the light outcoupling factor $\xi(z)$ shown in **Figure 3.2**, which quantifies the emitted luminance at 0° to the surface normal as a function of emitter position. To obtain $\xi(z)$, the luminance was calculated as a function of the position z of a single emissive dipole and normalized to its maximum value. The light outcoupling factor has a maximum close to the EML/ETL interface. The maximum is slightly shifted towards the hole transport layer (HTL) because the evaporated electron transport layer (ETL) thickness was slightly lower (52 nm) than the optimum value (56 nm) obtained from simulations performed prior to device fabrication. At the HTL/EML interface, $\xi(z)$ is reduced by almost 50% due to a reduction of $g(z)$.

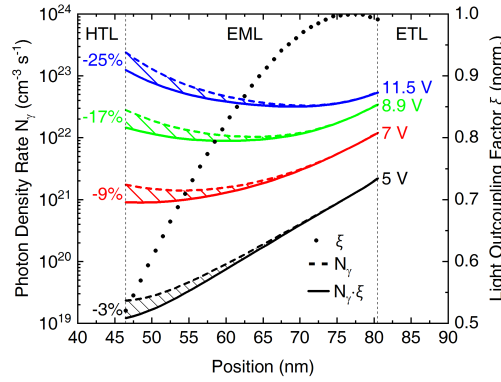


Figure 3.2 – Bias-dependent spatial distribution of generated photons before (dashed lines) and after (solid lines) considering the influence of the position-dependent light outcoupling factor (dotted line). The shift of the main emission from the EML/ETL interface to the HTL/EML interface reduces the emitted photons (shaded area) due to a lower light outcoupling factor $\xi(z)$.

In addition, Figure 3.2 shows the spatial distribution of the generated photons $N_\gamma(z)$ for different biases (dashed lines). At low biases, photons are mainly generated at the EML/ETL interface, while for higher biases, the maximum of the emission originates from the HTL/EML interface. The solid lines in Figure 3.2 represent the influence of the light outcoupling on the generated photons. Integrating the effect of the position-dependent light outcoupling factor and the bias-dependent distribution of generated photons over the entire EML results in a 3% reduction of emitted photons at low bias and in a 25% reduction at high bias as indicated with the shaded areas in Figure 3.2.

These outcoupling losses caused by the shifting emission zone reduce the luminance and contribute significantly to the reduction of the CE at high biases (cf. equation 3). However, to

describe the initial increase of CE, exciton quenching has to be considered as discussed in the following.

Influence of the emission zone on exciton quenching

As discussed above, the spatial distribution of emitting dipoles is strongly bias-dependent, which also influences the exciton quenching contributions at different biases. In the electro-optical model, the exciton physics is modeled with the following exciton continuity equation:

$$\frac{d\mathcal{T}(t, z)}{dt} = G \cdot R(t, z) + \nabla J_s(t, z) - F(z) \cdot k_{rad} \cdot \mathcal{T}(t, z) - k_{nonrad} \cdot \mathcal{T}(t, z) - k_{TPQH} \cdot \mathcal{T}(t, z) \cdot p(t, z) - k_{TPQe} \cdot \mathcal{T}(t, z) \cdot n(t, z) - k_{ann} \cdot \mathcal{T}(t, z)^2. \quad (3.3)$$

$G \cdot R(t, z)$ is the generation term for the time- (t) and position- (z) dependent triplet exciton density $\mathcal{T}(t, z)$, which is calculated from the exciton formation ratio $G = 1$ and the Langevin recombination rate R , where R is proportional to the electron and hole density in the EML ($R \propto n(t, z) \cdot p(t, z)$)²⁰. Only the triplet exciton equation is relevant because any singlet excitons quickly relax to triplet states on the Ir(ppy)₂(acac) emitter as no host emission and no fluorescence emission from the emitter was observed. $\nabla J_s(t, z) \propto \frac{d^2 T}{dx^2}$ is the exciton diffusion term, and $F(z) \cdot k_{rad} \cdot \mathcal{T}(t, z)$ describes radiative recombination of excitons with a rate constant k_{rad} modified by the position-dependent Purcell factor $F(z)$. The term $k_{nonrad} \cdot \mathcal{T}(t, z)$ represents non-radiative recombination with a rate constant k_{nonrad} . The terms $k_{TPQH} \cdot \mathcal{T}(t, z) \cdot p(t, z)$ and $k_{TPQe} \cdot \mathcal{T}(t, z) \cdot n(t, z)$ are the position-dependent triplet-polaron quenching terms, depending on the hole- and electron density with k_{TPQH} and k_{TPQe} being the respective rate constants. $k_{ann} \cdot \mathcal{T}(t, z)^2$ is the position-dependent triplet-triplet annihilation term with a rate constant k_{ann} . Integrating the terms in equation 3.3 over the emission layer yields the total contributions of each mechanism to the exciton continuity equation.

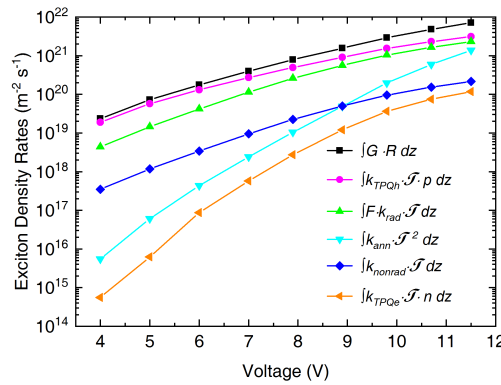


Figure 3.3 – Integrated terms of the exciton continuity equation for different biases. The integrated diffusion term is zero.

Figure 3.3 shows the bias dependence of the individual terms at steady state ($\frac{d\mathcal{T}(t, z)}{dt} = 0$).

Exciton generation (black line) increases with bias as expected. The main contribution reducing the number of excitons is triplet-polaron quenching with holes (magenta line), followed by radiative recombination (green line). Triplet-triplet annihilation (cyan line) is strongly bias-dependent and becomes increasingly important at high bias. Non-radiative recombination (blue line) and triplet-polaron quenching with electrons (orange line) are only minor contributions to the exciton balance, which agrees with findings in Adachi et al.²³ and Oyama et al.²⁸. The diffusion term in equation 3.3 vanishes after integration because exciton diffusion is limited to the EML.

Figure 3.4a shows the relative contribution of the individual terms of the exciton continuity equation (eq. 3.3) at each bias where 100% corresponds to the total number of generated excitons. The photons emitted into the hemisphere (red bars) are calculated via mode analysis from the radiatively decaying excitons ($\int F(z) \cdot k_{rad} \cdot \mathcal{T}(t, z) dz$). The light blue bars indicate the photons lost in evanescent, substrate and guided modes and through absorption. **Figure S3.1** shows these individual contributions. The shaded area in the light blue bars in Figure 3.4a indicate the lost photons due to the light outcoupling losses described by $\xi(z)$. As discussed in the context of Figure 3.2, the position-dependent light outcoupling factor $\xi(z)$ and the bias-dependent distribution of generated photons leads to a reduction of emitted photons by up to 25% for increasing biases. This corresponds to a loss of up to 8% of the generated excitons (shaded area in Figure 3.4a). At low biases, the outcoupling losses due to EMZ change contribute with less than 1%. Figure 3.4b zooms into the region of out-coupled

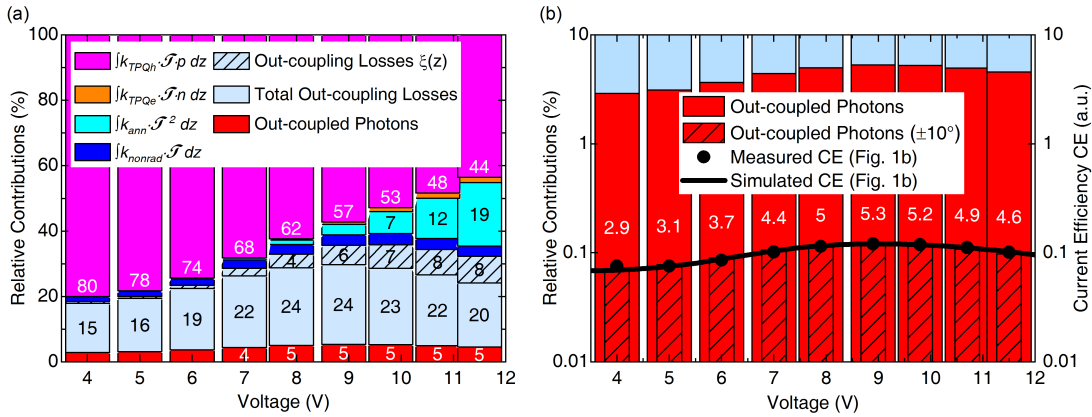


Figure 3.4 – Relative contributions of the individual terms of the exciton continuity equation where 100% corresponds to the total number of generated excitons (a) and the comparison of the outcoupled photons to the measured and simulated current efficiency (b). See text for details.

photons in Figure 3.4a, and shows the percentage of photons emitted into an angular range of $\pm 10^\circ$ (shaded bars) which increases up to 9 V before it decreases again at higher biases. The ratio of these out-coupled photons to generated excitons exactly resembles the measured current efficiency (cf. Figure 3.1 b), because the CE can also be calculated from the ratio of emitted photons ($\propto L$) and generated excitons ($\propto J$).

The contributions of non-radiative recombination (blue bars in Figure 3.4a) and triplet-polaron quenching with electrons (orange bars in Figure 3.4a) are essentially bias-independent and contribute with 1-2% and 1-3% to the total losses of generated excitons. Triplet-triplet annihilation (cyan bars in Figure 3.4a) becomes significant at high bias due to the quadratic dependence on exciton density and contributes up to 19% to the total losses. As can be seen from the magenta bars in Figure 3.4, triplet-polaron quenching with holes is the largest loss mechanism. Interestingly, the TPQh losses at low bias are rather large and decrease at higher bias. The behavior of TPQ with holes is explained in **Figure 3.5**, which shows the exciton distribution together with the electron and hole densities for 5 and 11.5 V.

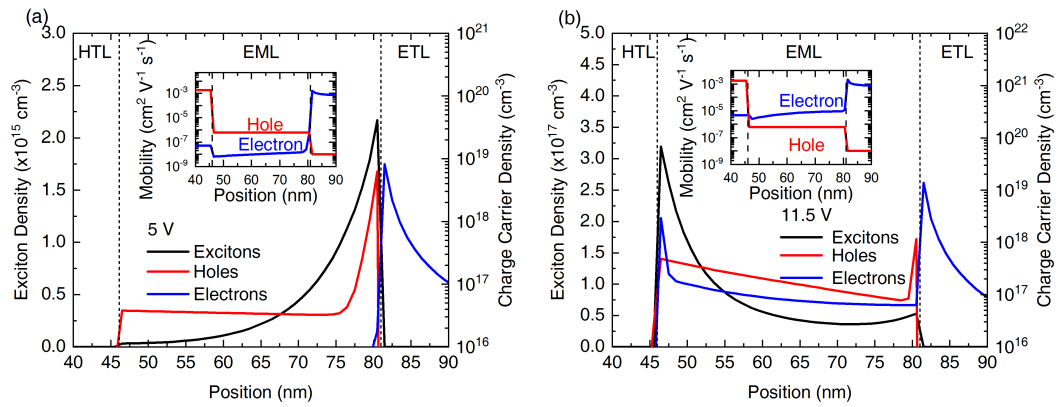


Figure 3.5 – Exciton distribution together with the hole and electron density profiles for 5 V (a) and 11.5 V (b). The insets show the effective hole and electron mobilities.

At 5 V (Figure 3.5a) the majority of electrons are in the ETL, while the holes accumulate at the EML side of the EML/ETL interface. Thus, the exciton density has a maximum at this interface and TPQ with holes is prominent. At 11.5 V (Figure 3.5b), a significant amount of electrons is being injected into the EML. Due to the larger field-dependence of the mobility for electrons than for holes, the effective electron mobility is larger than the hole mobility (cf. insets to Figure 3.5), electrons accumulate at the HTL/EML interface. The main exciton density is now at the HTL/EML interface where the hole density is low, and TPQ with holes becomes less prominent at high biases. We like to note that the large field dependent electron mobility is required to explain the shift of the EMZ with bias as presented previously¹⁶.

In References^{38,39}, two similar OLED stacks with larger EQE and similar emission zone have been presented. In those OLEDs, no energy barrier for electrons was present at the EML/ETL interface. When zeroing this energy barrier in our model, an increased electron density in the EML close to the EML/ETL interface is obtained. These electrons recombine, thereby reducing the number of excessive holes present at the EML/ETL interface. This significantly reduces the contribution of TPQ to 9% and increases the EQE to 13%. The EQE is, thus, strongly influenced by this energy barrier.

From the insights gained from the electro-optical model, the measured current efficiency (cf.

Figures 3.1 and 3.4a and b) can be well understood: The initial CE increase is due to a reduction of TPQ with holes because the emission zone shifts away from regions with large hole density. The decrease of CE at high bias is caused by increased TTA losses and by increased outcoupling losses due to the shifting emission zone. Thus, both CE trends, the increase and the decrease, are linked to the bias-dependent emission zone.

Influence of the emission zone on the EL decay

The decay time of emissive dipoles is known to depend on the local optical environment, and can be described by considering the position-dependent Purcell factor $F(z)$. The Purcell effect describes the dynamics of the dipole emission within an optical cavity, and a lower Purcell factor leads to a reduced spontaneous emission rate, and, thus, to a longer decay time²⁰. Because the emission zone in the investigated OLED stack shifts with bias, the electroluminescence decay rate is expected to change due to the Purcell effect. **Figure 3.6** shows the position-dependent Purcell factor together with the radiative exciton density rate calculated with the true Purcell factor (solid lines) and with a fictitious, constant Purcell factor of 1.65 (dashed lines). At low bias, the main emission originates at the EML/ETL interface with F being 1.65, while for high biases, the emission zone shifts towards the HTL/EML interface where F is reduced to 1.2.

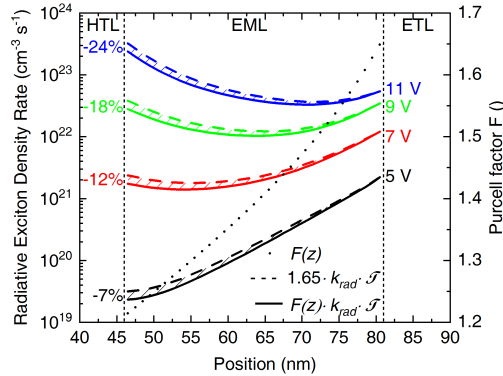


Figure 3.6 – Position-dependent Purcell factor F and calculated radiative exciton density rates with the true, position-dependent (solid lines) or fictitious, constant F of 1.65 (dashed lines).

The shaded area in Figure 3.6 indicates the reduction of the radiative exciton decay rate due to the changes of the emission zone and the accompanying reduced Purcell effect. With increasing bias, the contribution of the Purcell effect monotonically increases, which leads to an increased decay time (see equation 3.4 below). The measured decay time in the inset to **Figure 3.7** reveals a bias region with increasing decay time, but also a bias region with decreasing decay time, thus the contributions from the Purcell effect alone cannot explain the measurements.

As discussed in the previous section, exciton quenching plays a dominant role in explaining the measured trend in current efficiency. Exciton quenching is also known to influence the

radiative decay time t in electroluminescence and in photoluminescence (PL) experiments. In the absence of exciton quenching, a mono-exponential decay of the PL signal is expected after the laser excitation is turned-off, because only the terms describing radiative and non-radiative decay remain in the exciton continuity equation (cf. equation 3.3). In such a case, the PL decay time t_{PL} is directly related to the (non-)radiative decay rates³⁷

$$\tau_{PL} \propto \frac{1}{F \cdot k_{rad} + k_{nonrad}}. \quad (3.4)$$

When the PL decay is measured while a bias is applied to the OLED, the electron and hole densities in equation 3.3 remain constant, thus allowing to elucidate the rates for TPQ with holes and electrons^{28,37}. By varying the intensity of the exciting light, information about TTA can be obtained⁴⁰. All PL experiments have in common that the exciton generation term vanishes immediately after the excitation source is switched off.

In contrast, the EL decay is fundamentally different, because the generation term in equation 3.3 can persist over long times, in our case a few microseconds. The generation term strongly depends on the applied bias before turn-off, and is influenced by a multitude of variables, foremost the charge carrier distribution, the electric field inside the EML and the charge carrier mobilities as discussed in the context of **Figure 3.8**.

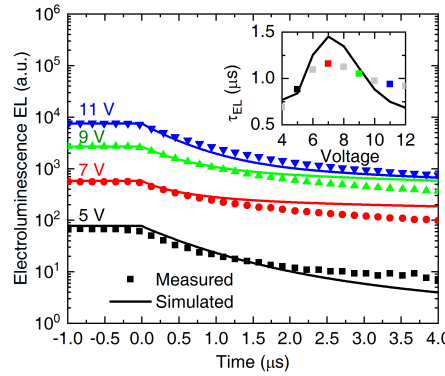


Figure 3.7 – Measured and simulated transient electroluminescence signals for different on-voltages. The inset shows the initial EL decay times extracted from the measured (symbols) and simulated (solid line) EL signal.

Figure 3.7 shows the measured and simulated EL decay for different on-voltages. The simulation fits the measurements reasonably well, supporting the validity of the presented model. As a consequence of the significant contribution of the exciton generation and quenching terms, the EL decay is not mono-exponential anymore, and we find that the slope of the initial decay is not directly related to the (non-)radiative decay rates, especially after $t > 1 \mu s$ and at high on-voltages. The inset to Figure 3.7 shows the measured and simulated decay time t_{EL} extracted from the initial slope of the EL decay ($t < 1 \mu s$) assuming an exponential decay proportional to $\exp(-\frac{t}{\tau_{EL}})$.

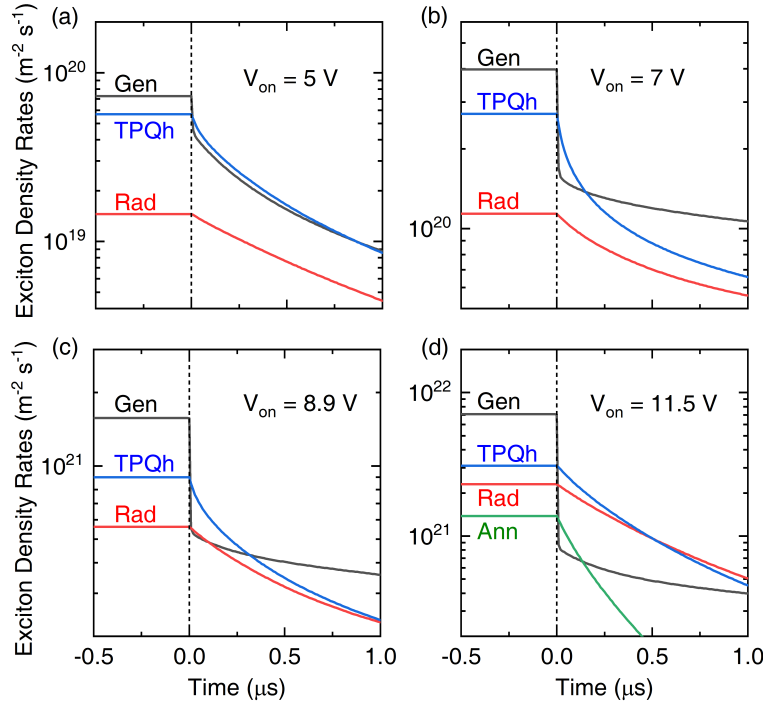


Figure 3.8 – Integrated exciton rates for generation (black lines), triplet-polaron quenching with holes (blue lines) and triplet-triplet annihilation (green line) to illustrate the respective contribution on the EL decay (red lines) at different biases.

To illustrate the complex interplay of the individual contributions in the exciton continuity equation (eq. 3.3) on the EL decay, Figure 3.8 shows the dominant terms integrated over the EML. At 5 V (Figure 3.8a) the generation term ($\int G \cdot R \, dz$) decays over a long time because the effective charge carrier mobilities are low, which leads to a low Langevin recombination rate. Interestingly, at this bias, the generation term is essentially cancelled by the TPQ term for holes ($\int k_{TPQh} \cdot \mathcal{T} \cdot p \, dz$). The other terms are negligible, thus the EL decay is essentially mono-exponential even in the presence of high exciton quenching. In this special case where the generation term is essentially cancelled by the TPQh term, the radiative decay time t_{EL} of $0.88 \, \mu s$ can be used to calculate the intrinsic (non-)radiative decay rates from equation 3.4, if the intrinsic quantum efficiency ($q_0 = \frac{k_{rad}}{k_{rad} + k_{nonrad}} = 0.889$) and the Purcell factor are known. Using the Purcell factor where the exciton density at 5 V is largest ($F_{EML/ETL} = 1.65$), the values $k_{rad} = 0.64 \, \mu s^{-1}$ and $k_{nonrad} = 0.08 \, \mu s^{-1}$ were calculated, which agrees well with the values of $0.613 \, \mu s^{-1}$ and $0.077 \, \mu s^{-1}$ used in the simulations. With these rate constants, an intrinsic emitter lifetime of $t_{intrinsic} = \frac{1}{k_{rad} + k_{nonrad}} = 1.39 \, \mu s$ was calculated, which is close to the value of $1.6 \, \mu s$ measured in PL experiments in solution⁴¹. Thus, in the special case where certain terms in the exciton continuity equation cancel each other so that only the radiative and non-radiative terms remain, the mono-exponential EL decay can be used to extract the intrinsic emitter lifetime.

At intermediate biases (Figures 3.8b, c), the generation term shows a sudden drop and the TQPh term is dominating the EL decay for $\approx 0.25 \mu s$ before the generation term starts to dominate the decay. At high bias (Figure 3.8d), the TTA term ($\int k_{ann} \cdot \mathcal{T}^2 dz$) becomes significant up to $\approx 0.25 \mu s$, after which it vanishes quickly. The generation term at this bias is also negligible and the EL decay is dominated only by TPQ with holes.

We like to note, that the individual contributions shown in Figure 3.8 strongly depend on the OLED stack and, therefore, cannot easily be generalized. Nevertheless, Figure 3.8 highlights that, in general, a full electro-optical model is required to extract the exciton rate constants and the intrinsic emitter lifetime from EL decay measurements.

Conclusion

We measured the current density - voltage - luminance (J-V-L), current efficiency (CE) and transient EL characteristics of a phosphorescent OLED. The current efficiency showed an unexpected increase up to 9 V followed by a decrease. An electro-optical model was devised to describe all measurements simultaneously. The model enabled insights into the mechanisms leading to the observed CE trends. A central outcome was that the emission zone changes with bias, which has manifold consequences. The bias-dependent emission zone causes an increase of the light outcoupling losses due to a reduced light outcoupling factor at high bias. Additionally, this shift of the emission zone significantly reduces the contribution of the triplet-polaron quenching at high bias, because the main emission occurs in a region with lower hole density. Only the combination of the reduced TPQ contribution with the increased light outcoupling losses and TTA contribution could explain the measured CE.

The model further allowed identifying individual contributions from the exciton continuity equation. Because of the dominating role of the exciton generation term, the EL decay is in general not mono-exponential, and the initial decay time is related to the intrinsic emitter lifetime only under special circumstances when the generation term is cancelled by the TPQ term.

This work highlights the benefits of an accurate knowledge of the emission zone and exciton quenching to reveal the details of the mechanism leading to the efficiency roll-off at high biases. An electro-optical model is, thus, a useful tool to identify strategies to further improve OLED efficiency.

Acknowledgements

We thank, S. Jenatsch, B. Blülle, S. Züfle, A. Stous and A. Gentsch from Fluxim AG and F. Nüesch from EPFL for fruitful discussions and valuable comments. Financial support from the Swiss National Science Foundation under grant no. 162230 is gratefully appreciated.

References

1. Kim, K.-H. *et al.* Crystal Organic Light-Emitting Diodes with Perfectly Oriented Non-Doped Pt-Based Emitting Layer. *Advanced Materials* **28**, 2526–2532 (Apr. 1, 2016).
2. Kim, K.-H., Ahn, E. S., Huh, J.-S., Kim, Y.-H. & Kim, J.-J. Design of Heteroleptic Ir Complexes with Horizontal Emitting Dipoles for Highly Efficient Organic Light-Emitting Diodes with an External Quantum Efficiency of 38%. *Chemistry of Materials* **28**, 7505–7510 (Oct. 25, 2016).
3. Kim, K.-H. *et al.* Phosphorescent dye-based supramolecules for high-efficiency organic light-emitting diodes. *Nature Communications* **5**, 4769. <http://www.nature.com/ncomms/2014/140910/ncomms5769/full/ncomms5769.html> (Sept. 10, 2014).
4. Kaji, H. *et al.* Purely organic electroluminescent material realizing 100% conversion from electricity to light. *Nature Communications* **6**. 00003, 8476. <http://www.nature.com/ncomms/2015/151019/ncomms9476/full/ncomms9476.html> (Oct. 19, 2015).
5. Komino, T. *et al.* Electroluminescence from completely horizontally oriented dye molecules. *Applied Physics Letters* **108**, 241106 (June 13, 2016).
6. Lin, T.-A. *et al.* Sky-Blue Organic Light Emitting Diode with 37% External Quantum Efficiency Using Thermally Activated Delayed Fluorescence from Spiroacridine-Triazine Hybrid. *Advanced Materials (Deerfield Beach, Fla.)* **28**, 6976–6983 (Aug. 2016).
7. Moon, C.-K. *et al.* Combined Inter- and Intramolecular Charge-Transfer Processes for Highly Efficient Fluorescent Organic Light-Emitting Diodes with Reduced Triplet Exciton Quenching. *Advanced Materials* **29**, 1606448 (2017).
8. Jeon, S. K. & Lee, J. Y. Direct monitoring of recombination zone shift during lifetime measurement of phosphorescent organic light-emitting diodes. *Journal of Industrial and Engineering Chemistry* **32**, 332–335. <http://www.sciencedirect.com/science/article/pii/S1226086X15004207> (Dec. 25, 2015).
9. Lee, J. *et al.* Synergetic electrode architecture for efficient graphene-based flexible organic light-emitting diodes. *Nature Communications* **7**, 11791. <https://www.nature.com/articles/ncomms11791> (June 2, 2016).
10. Song, J. *et al.* Lensfree OLEDs with over 50% external quantum efficiency via external scattering and horizontally oriented emitters. *Nature Communications* **9**, 3207. <https://www.nature.com/articles/s41467-018-05671-x> (Aug. 10, 2018).
11. Giebink, N. C. *et al.* Intrinsic luminance loss in phosphorescent small-molecule organic light emitting devices due to bimolecular annihilation reactions. *Journal of Applied Physics* **103**. 00060, 044509 (Feb. 15, 2008).
12. Murawski, C., Leo, K. & Gather, M. C. Efficiency Roll-Off in Organic Light-Emitting Diodes. *Advanced Materials* **25**. 00088, 6801–6827 (Dec. 1, 2013).
13. Forrest, S. R., Bradley, D. D. C. & Thompson, M. E. Measuring the Efficiency of Organic Light-Emitting Devices. *Advanced Materials* **15**, 1043–1048 (July 4, 2003).

14. Geffroy, B., Roy, P. I. & Prat, C. Organic light-emitting diode (OLED) technology: materials, devices and display technologies. *Polymer International* **55**, 572–582 (June 1, 2006).
15. Tsutsui, T. & Takada, N. Progress in Emission Efficiency of Organic Light-Emitting Diodes: Basic Understanding and Its Technical Application. *Japanese Journal of Applied Physics* **52**. 00009, 110001. <http://iopscience.iop.org/1347-4065/52/11R/110001> (Nov. 1, 2013).
16. Regnat, M., Pernstich, K. P., Züfle, S. & Ruhstaller, B. Analysis of the Bias-Dependent Split Emission Zone in Phosphorescent OLEDs. en. *ACS Applied Materials & Interfaces* **10**, 31552–31559. ISSN: 1944-8244, 1944-8252. <http://pubs.acs.org/doi/10.1021/acsami.8b09595> (2018) (Sept. 2018).
17. *Paivos, Platform for All-In-One Characterization of Solar Cells and OLEDs, Characterization Suite Software version 4.12*, Fluxim Fluxim. 00000. <https://www.fluxim.com/paivos/>.
18. *Characterization Suite* Fluxim. <https://www.fluxim.com/news/2018/5/4/characterization-suite-41-released> (2019).
19. *Setfos 5.0*, Fluxim Fluxim. 00000. <https://www.fluxim.com/setfos-intro/>.
20. Perucco, B. *et al.* On the exciton profile in OLEDs-seamless optical and electrical modeling. *Organic Electronics* **13**, 1827–1835. <http://www.sciencedirect.com/science/article/pii/S1566119912002534> (Oct. 1, 2012).
21. Ruhstaller, B. *et al.* in *Optoelectronic Devices and Properties*, edited by Oleg Sergiyenko, ISBN 978-953-307-204-3, DOI: 10.5772/14626 00009 (2011). (2017).
22. Perucco, B., Reinke, N. A., Müller, F., Rezzonico, D. & Ruhstaller, B. *The influence of the optical environment on the shape of the emission profile and methods of its determination* in *Organic Photonics IV* (eds Heremans, P. L., Coehoorn, R. & Adachi, C.) **7722**. 00002 (Proc. of SPIE, Apr. 2010), 77220F1. (2016).
23. Adachi, C., Baldo, M. A., Thompson, M. E. & Forrest, S. R. Nearly 100% internal phosphorescence efficiency in an organic light-emitting device. *Journal of Applied Physics* **90**, 5048–5051 (Oct. 31, 2001).
24. Baek, H.-I., Lee, C. & Chin, B. D. Comparison of the carrier mobility, unipolar conduction, and light emitting characteristics of phosphorescent host–dopant system. *Synthetic Metals* **162**, 2355–2360. <http://www.sciencedirect.com/science/article/pii/S0379677912003992> (Dec. 31, 2012).
25. Lee, S.-B., Yasuda, T., Yang, M.-J., Fujita, K. & Tsutsui, T. Charge Carrier Mobility in Vacuum-Sublimed Dye Films for Light-Emitting Diodes Studied by the Time-of-Flight Technique. *Molecular Crystals and Liquid Crystals* **405**, 67–73 (Jan. 1, 2003).
26. Naka, S., Okada, H., Onnagawa, H. & Tsutsui, T. High electron mobility in bathophenanthroline. *Applied Physics Letters* **76**, 197–199 (Jan. 1, 2000).
27. Noh, S., Suman, C. K., Hong, Y. & Lee, C. Carrier conduction mechanism for phosphorescent material doped organic semiconductor. *Journal of Applied Physics* **105**, 033709 (Feb. 1, 2009).
28. Oyama, S., Sakai, H. & Murata, H. Rate constant of exciton quenching of Ir(ppy)₃ with hole measured by time-resolved luminescence spectroscopy. *Japanese Journal of Applied*

- Physics* **55**, 03DD13. <http://stacks.iop.org/1347-4065/55/i=3S2/a=03DD13?key=crossref.47d4fa0d1c44a4968a0f340115551c77> (Mar. 1, 2016).
29. Parshin, M. A., Ollevier, J. & der Auweraer, M. V. *Charge carrier mobility in CBP films doped with Ir(ppy) 3 in Organic Optoelectronics and Photonics II* (eds Heremans, P. L., Muccini, M. & Meulenkamp, E. A.) **6192** (Proc. of SPIE, Apr. 21, 2006), 61922A1. <http://proceedings.spiedigitallibrary.org/proceeding.aspx?doi=10.1117/12.663553> (2017).
 30. Yamazaki, S. & Tsutsui, T. *Physics and Technology of Crystalline Oxide Semiconductor CAAC-IGZO: Application to Displays* Google-Books-ID: 11B7DQAAQBAJ. 444 pp. ISBN: 978-1-119-24745-6. <https://www.amazon.com/Physics-Technology-Crystalline-Semiconductor-CAAC-IGZO/dp/1119247454?SubscriptionId=AKIAIOBINVZYXZQZ2U3A&tag=chimbori05-20&linkCode=xm2&camp=2025&creative=165953&creativeASIN=1119247454> (John Wiley & Sons, Feb. 6, 2017).
 31. Yoo, S.-J. *et al.* A new electron transporting material for effective hole-blocking and improved charge balance in highly efficient phosphorescent organic light emitting diodes. *Journal of Materials Chemistry C* **1**, 2217–2223. <https://pubs.rsc.org/en/content/articlelanding/2013/tc/c3tc00801k> (Feb. 21, 2013).
 32. Neukom, M. T., Züfle, S. & Ruhstaller, B. Reliable extraction of organic solar cell parameters by combining steady-state and transient techniques. *Organic Electronics* **13**, 2910–2916. <http://www.sciencedirect.com/science/article/pii/S1566119912004223> (Dec. 1, 2012).
 33. Knapp, E. & Ruhstaller, B. Analysis of negative capacitance and self-heating in organic semiconductor devices. *Journal of Applied Physics* **117**. 00001, 135501 (Apr. 7, 2015).
 34. Chen, C.-P. *et al.* High efficiency blue phosphorescent organic light-emitting diode using tetraphenylsilane core molecule as host material in 2016 23rd International Workshop on Active-Matrix Flatpanel Displays and Devices (AM-FPD) 2016 23rd International Workshop on Active-Matrix Flatpanel Displays and Devices (AM-FPD) (IEEE, July 2016), 113–114.
 35. Chopra, N., Lee, J., Xue, J. & So, F. High-Efficiency Blue Emitting Phosphorescent OLEDs. *IEEE Transactions on Electron Devices* **57**, 101–107 (Jan. 2010).
 36. Li, W., Li, J., Wang, F., Gao, Z. & Zhang, S. Universal Host Materials for High-Efficiency Phosphorescent and Delayed-Fluorescence OLEDs. *ACS Applied Materials & Interfaces* **7**, 26206–26216 (Dec. 2, 2015).
 37. Wehrmeister, S. *et al.* Combined Electrical and Optical Analysis of the Efficiency Roll-Off in Phosphorescent Organic Light-Emitting Diodes. *Physical Review Applied* **3**. 00002, 024008 (Feb. 19, 2015).
 38. Liehm, P. *et al.* Comparing the emissive dipole orientation of two similar phosphorescent green emitter molecules in highly efficient organic light-emitting diodes. *Applied Physics Letters* **101**. 00052, 253304 (Dec. 17, 2012).
 39. Sim, B., Moon, C.-K., Kim, K.-H. & Kim, J.-J. Quantitative Analysis of the Efficiency of OLEDs. *ACS Applied Materials & Interfaces* **8**. 00000, 33010–33018 (Dec. 7, 2016).

40. Baldo, M. A. *et al.* Highly efficient phosphorescent emission from organic electroluminescent devices. *Nature* **395**, 151–154. <https://www.nature.com/articles/25954> (Sept. 1998).
41. Lamansky, S. *et al.* Synthesis and Characterization of Phosphorescent Cyclometalated Iridium Complexes. *Inorganic Chemistry* **40**, 1704–1711 (Mar. 1, 2001).

3.1 Appendix

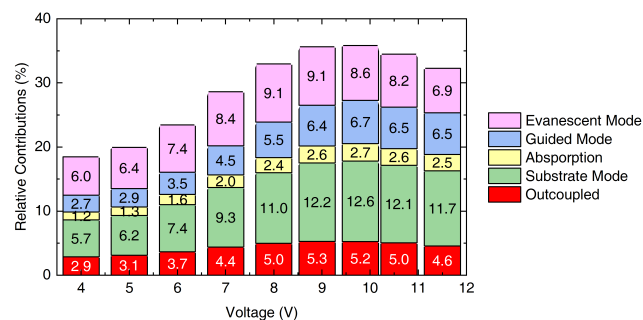


Figure S3.1 – Relative contributions of photons emitted into air and dissipated in the OLED stack where 100% corresponds to the total number of generated excitons (cf. Fig 3.4).

Table S3.1 – Optimized model parameters used in the electro-optical simulations.

	Optimized Paramters
PEDOT:PSS	
Work function (eV)	5.14
[†] Thickness (nm)	30
TCTA	
LUMO (eV)	2.3
HOMO (eV)	5.65
^{†,‡} Mobility μ_e (m ² /Vs)	$\mu_0 = 3.3\text{e-}14, \gamma = 0.9\text{e-}3^*$
[‡] Mobility μ_h (m ² /Vs)	$\mu_0 = 1.8\text{e-}7, \gamma = 7.1\text{e-}7$
[†] Thickness (nm)	46
CBP	
LUMO (eV)	2.56
HOMO (eV)	5.71
[‡] Mobility μ_e (m ² /Vs)	$\mu_0 = 3.1\text{e-}16, \gamma = 1.4\text{e-}3$
[‡] Mobility μ_h (m ² /Vs)	$\mu_0 = 6.0\text{e-}11, \gamma = 4.5\text{e-}9$
[†] Thickness (nm)	35
NBPhen	
LUMO (eV)	2.8
HOMO (eV)	6.4
[‡] Mobility μ_e (m ² /Vs)	$\mu_0 = 5.0\text{e-}8, \gamma = 1.5\text{e-}4$
^{†,‡} Mobility μ_h (m ² /Vs)	$\mu_0 = 1.0\text{e-}12, \gamma = 1.0\text{e-}8$
[†] Thickness (nm)	52
Ca	
Work function (eV)	2.93
[†] Thickness (nm)	15
Excitonic Parameters in CBP	
Exciton formation ratio G (1)	1
Diffusion constant (nm ² /μs)	51.7
Radiative rate k_{rad} (μs ⁻¹)	0.61
Non-radiative rate k_{nonrad} (μs ⁻¹)	0.08
Annihilation rate k_{ann} (cm ³ /s)	3.6e-12
TPQ e- rate k_{TPQe} (cm ³ /s)	9.5e-14
TPQ h+ rate k_{TPQh} (cm ³ /s)	3.5e-12
[†] Dipole orientation (1)	0.24
Electric parameters	
[†] Series resistance R_s (Ohm)	10
[†] Parallel resistance R_p (MOhm)	15

[†] fixed model parameters; [‡] $\mu = \mu_0 \cdot e^{\gamma_{n,p}\sqrt{E}}$ with μ_0 zero field mobility, $\gamma_{n,p}$ field coefficient and E electric field, *the large field-coefficient is a result of the optimization and could also be chosen much smaller without influencing the results.

4 Prediction of Efficiency Enhancement in TADF OLEDs

Routes for Efficiency Enhancement in Fluorescent TADF Exciplex Host OLEDs gained from an Electro-Optical Device Model

Markus Regnat, Kurt P. Pernstich, Kwon-Hyeon Kim, Jang-Joo Kim, Frank Nüesch and Beat Ruhstaller

M. Regnat, Dr. K. P. Pernstich, Prof. B. Ruhstaller
Institute of Computational Physics, Zurich University of Applied Sciences ZHAW, 8401 Winterthur, Switzerland Email: markus.regnat@zhaw.ch

Dr. Kwon-Hyeon Kim, Prof. Jang-Joo Kim
Department of Materials Science and Engineering, Seoul National University, Seoul 151-742, South Korea

M. Regnat, Prof. F. Nüesch
Institut des Matériaux, Ecole Polytechnique Fédérale de Lausanne, EPFL, Station 12, 1015 Lausanne, Switzerland

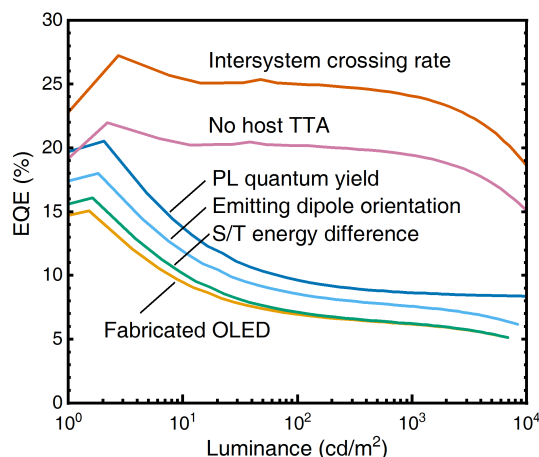
Prof. B. Ruhstaller
FLUXIM AG, Technoparkstrasse 2, 8406 Winterthur, Switzerland

A manuscript based on this chapter is submitted to Advanced Electronic Materials Journal.

Declaration of Contribution : Markus Regnat carried out the device characterization, did the optoelectronic simulation, analysed the data and contributed to manuscript preparation.

Abstract

A comprehensive device model describes the electro-optical characteristics of a TADF OLED with a fluorescent emitter and identifies promising routes for efficiency enhancement. Results show that e.g. by increasing the intersystem crossing rate or by reducing the triplet-triplet annihilation on the host, the external quantum efficiency can be raised by more than 200% at a luminance of 1000 cd/m^2 .



Introduction

The recent discovery of thermally activated delayed fluorescence (TADF) by the Adachi group^{1–4} attracted a lot of attention in research and industry. It was found that an organic light emitting diode (OLED) with a fluorescent emitter material having a very small energy difference between the triplet and singlet states facilitates reverse intersystem crossing of triplets to singlets at room temperature, resulting in an increased efficiency. This discovery opened the possibility to fabricate highly efficient fluorescence-based OLEDs with external quantum efficiencies (EQEs) similar to phosphorescence-based OLEDs, but with the advantages of a broader variety of emitter materials (no Iridium and Platinum complexes), higher color purity and higher operational stability.⁵

Different TADF approaches are presently employed to increase the efficiency of fluorescent OLEDs including TADF emitter molecules, TADF assistant dopant molecules, TADF exciplex hosts and different combination of them. With TADF emitters in a conventional host⁶, an exciplex host⁷, or in a TADF exciplex host⁸ external quantum efficiencies of up to 37% were obtained without light outcoupling structures, which is similar to the values obtained with the best phosphorescent OLEDs.⁹ By adding TADF assistant dopants to fluorescent emitters in conventional hosts^{5,10,11} or in a TADF exciplex host¹², EQEs of up to 24% were reported. The third class uses TADF exciplex hosts with conventional fluorescent emitters, and EQEs of $>10\%$ ^{10,13} are currently reached. The OLEDs investigated in this study are of this type.

While many different approaches to fabricate TADF OLEDs are pursued, modelling of TADF OLEDs have received only little attention.^{8,14,15} In this study we present, to the best of our knowledge, the first electro-optical device model which accounts for charge carriers, excitons and photons, to describe the electro-optical characteristics of an OLED with a fluorescent dye in a TADF exciplex host.¹³ The model reproduces the current-voltage-luminance (I-V-L) characteristics, the angle-dependent electroluminescence (EL) spectra and the EL decay. From

the angle-dependent measurements, the emission zone (EMZ) profile is determined.^{16–19} The knowledge of the EMZ profile is, among others, important to set the exciton diffusion constant. Surprisingly, a split emission zone is found, where large exciton densities are present at both interfaces of the emitting layer. The model also reveals the strongly bias-dependent triplet harvesting contribution to the EQE. From a model parameter study, several routes are proposed for further optimization of the OLED stack and the increase of the EQE. The simulations identify that increasing the intersystem crossing rate or reducing the triplet-triplet annihilation rate results in the largest improvement of the EQE. In the best case scenario, efficiencies up to 42% are predicted.

Modelling and model parameters

To establish the electro-optical OLED device model, a preview version of the simulation software Setfos version 5.0 from Fluxim Inc. with the drift-diffusion and emission module was used.²⁰ For further details on the charge carrier drift-diffusion and recombination, exciton migration as well as radiative dipole emission model implemented in Setfos refer to References^{21–23}. Initial input parameters for the electro-optical model, such as layer thicknesses, (birefringent) refractive indices, discrete highest and lowest molecular orbital (HOMO/LUMO) energy levels^{24–26}, field-dependent electron and hole mobilities^{27–29}, as well as excitonic parameters in the emission layer (EML)^{13,25,30} were either directly measured or taken from literature. The model parameters were manually adjusted in a way that the simulation results agree with the measurements described below, i.e. I-V-L characteristics and angle-dependent EL spectra. The optimized model parameters are given in **Figure 4.1**, **Figure S4.1** and in **Table S4.1**.

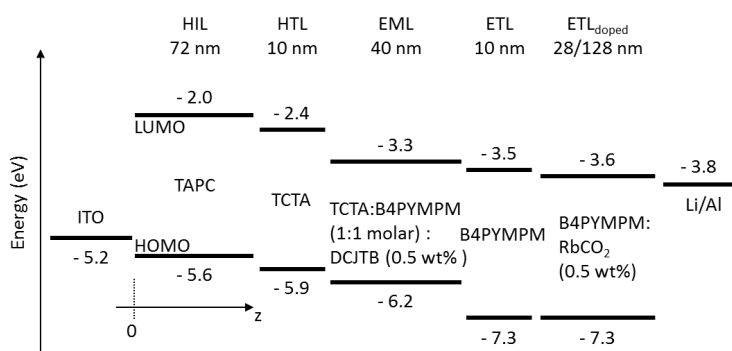


Figure 4.1 – Layer stack of the TADF exciplex host OLED with the layer thicknesses and the HOMO/LUMO energy levels used in the simulations. In the optically detuned OLED, the thickness of the doped ETL was increased from 28 nm to 128 nm.

Figure 4.1 shows the OLED layer stack with layer thicknesses and the frontier orbital energy levels of each layer used in the simulation. The OLEDs were fabricated as described in detail in Reference¹³, and the details of the model are described in Reference¹⁷ and³¹. The emissive

layer comprises co-evaporated Tris(4-carbazoyl-9-ylphenyl)amine (TCTA) and 4,6-Bis(3,5-di(pyridin-4-yl)phenyl)-2-methylpyrimidine (B4PYMPM) (1:1 molar ratio), doped with 0.5 wt% 4-(Dicyanomethylene)-2-tert-butyl-6-(1,1,7,7-tetramethyljulolidin-4-yl-vinyl)-4H-pyran (DCJTB). The EML was modelled with a hole mobility and HOMO energy level similar to TCTA and an electron mobility and LUMO energy level similar to B4PYMPM in order to reproduce the measured current-voltage characteristics. We like to note that the HOMO/LUMO levels of the co-evaporated exciplex host are often assumed to be identical to the respective energy levels of the pure constituent materials, but we did not find a parameter set with such identical energy levels that gave a good agreement to the measurements. That the energy levels can change upon co-evaporation has been reported before^{Jankus_2014} and, thus, the reported HOMO/LUMO energy levels for the exciplex host appear feasible.

To determine the emission zone profile from combined measurements and simulations, optically detuned OLEDs had to be fabricated.^{16,17,19} This was achieved by increasing the thickness of the doped electron transport layer (ETL) layer from 28 nm for the optically tuned OLED which maximizes EQE/light output to 128 nm for the detuned OLED. The doped ETL layer was modelled by introducing an electron donor doping concentration of $2.4 \times 10^{25} \text{ m}^{-3}$ and removing the field dependence of the electron mobility. This concentration was chosen in order to reproduce the measured current-voltage characteristics for optically tuned and detuned OLEDs.

To accurately simulate the luminance, current efficiency, EQE and angle-dependent EL spectra, multiple excitonic processes had to be considered in the emission layer as illustrated in **Figure 4.2**. Singlet and triplet exciplex generation on the exciplex host is modelled via Langevin recombination of electrons and holes, where a singlet to triplet ratio of 1:3 is considered by the exciplex generation factors $g_s = 0.25$ and $g_t = 0.75$. Host triplets are converted to host singlets with a reverse intersystem crossing rate

$$k_{RISC} = k_{ISC} e^{-\frac{\Delta E_{S/T}}{k_B T}} \quad (4.1)$$

where k_{ISC} is the intersystem crossing rate from host singlets to triplets and $\Delta E_{S/T}$ is the energy difference between those states. As illustrated in Figure 4.2, host triplets can recombine only non-radiatively as reported in²⁵, while host singlets can recombine radiatively and non-radiatively. The host singlets can also transfer their energy to the fluorescent DCJTB emitter via Förster resonance and Dexter energy transfer with a rate constant $k_{FRET/DEX} = 1 \text{ ns}^{-1}$. In the model, this rate constant was estimated to reproduce the weak light emission originating from the host singlets that was observed in the measurements. The guest emitter is modelled as having a singlet state that can recombine radiatively and non-radiatively. The dipole orientation of the emitter molecules is set to be 86% horizontal¹³, and the PL spectra of the host and guest emitters are taken from¹³ and are reproduced in Figure S2. Annihilation of both, host triplet exciplexes and guest singlet excitons had to be included in the model with the rate constants of $k_{TTA} = 9 \times 10^{-10} \text{ cm}^3/\text{s}$ and $k_{SSA} = 5 \times 10^{-9} \text{ cm}^3/\text{s}$ to accurately reproduce the measurement data. The three continuity rate equations for the exciton and the exciplexes are

given in the supplementary information.

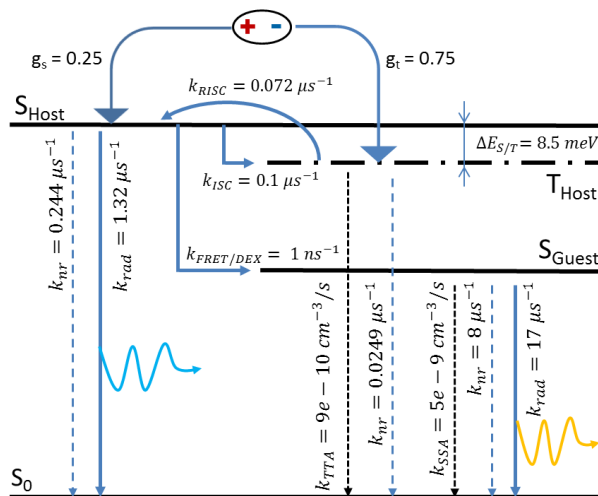


Figure 4.2 – Illustration of the excitonic processes in the emission layer of the TADF exciplex host OLED with fluorescent emitter. See text for details.

To model the spatial extent of the emission zone as determined from the optically detuned OLED measurements, exciton diffusion was enabled only for the guest singlet excitons with a diffusion constant of $900 \text{ nm}^2/\mu\text{s}$. Exciton diffusion is often described to occur via Förster resonance or Dexter energy transfer, in which a spectral overlap between the emission and absorption spectra is required. From the absorption and emission spectra in Reference¹³ (reproduced in Figure S4.2) we conclude that the spectral overlap integral between two TCTA:B4PYMPM host complexes essentially vanishes, while it is non-zero for the DCJTb guest molecules. From this we derived the assumption of exciton diffusion occurring only between guest molecules, even though the distance between guest molecules is much larger than those between host molecules. If only the host exciplexes would diffuse, the exciplex density profile changes significantly as shown in **Figure S4.4** but with slightly modified model parameters, especially an increased triplet-triplet annihilation rate, the same agreement between measurement and simulation can be obtained.

Electro-optical characterization

Figure 4.3a shows the excellent agreement between the simulated and the measured current density-voltage-luminance characteristics for the optically tuned and detuned OLEDs. The J-V characteristics for the tuned and detuned OLEDs is essentially identical due to the doped ETL layer, and only the light emission differs significantly as expected from the inset to Figure 4.3a. The electro-optical model parameter set was optimized to reproduce the measured data of the tuned OLED, and only the $\text{ETL}_{\text{doped}}$ thickness was changed to simulate the detuned OLED.

The minor deviations between simulated and measured JVL characteristics are attributed to variations during device manufacturing, while the minor deviations in current density at very low bias (< 1.5 V) are caused by solver settings.

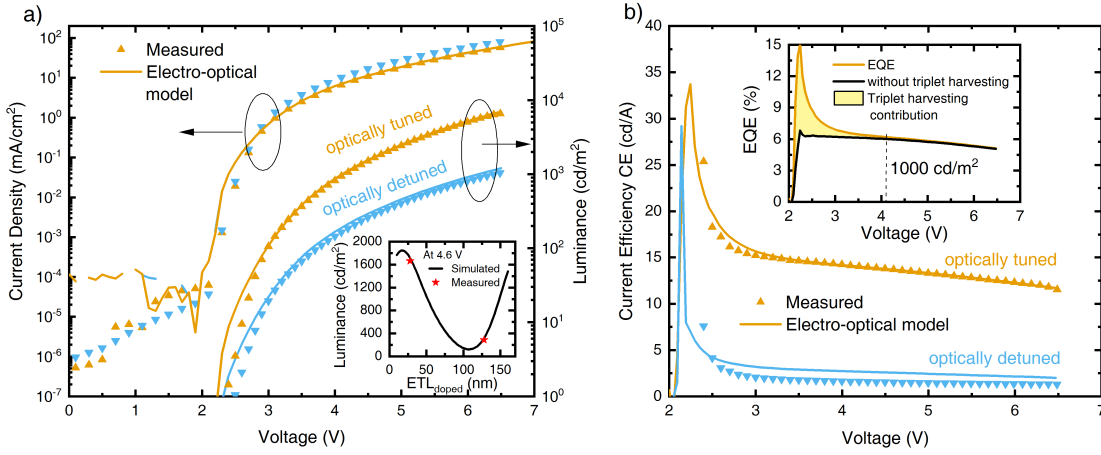


Figure 4.3 – Measured and simulated current density-voltage-luminance curves (a) and current efficiency (b) for optically tuned ($ETL_{doped} = 28$ nm) and detuned ($ETL_{doped} = 128$ nm) OLEDs. The inset to (a) shows the dependence of the luminance on the ETL_{doped} layer thickness and the inset to (b) shows the simulated EQE for the optically tuned OLED together with the contribution of triplet harvesting to the EQE.

Figure 4.3b shows the measured and simulated current efficiencies which were calculated from the luminance and current density data in Figure 4.3a. The current efficiency is highest right after turn-on of the OLED at ≈ 2.2 V and decreases rapidly up to ≈ 2.9 V and less pronounced at higher biases. To model these two regimes, triplet-triplet annihilation on the host and singlet-singlet annihilation on the guest had to be considered as discussed in detail below. The inset to Figure 4.3b shows the bias-dependence of the EQE for the optically tuned OLED (orange line) together with the contribution of triplet harvesting (shaded area). At low biases, very high efficiencies of up to 15% are obtained due to triplet harvesting. These EQEs are much higher than the theoretical limits for fluorescence based OLEDs using only singlet excitons for light emission as shown with the black line in the inset to Figure 4.3b, where the triplet harvesting process was switched off by deactivating reverse intersystem crossing in the model. Surprisingly, the simulations suggest that the triplet harvesting is only significant at low biases where the luminance is well below ≈ 100 cd/m^2 (cf. Figure 4.8).

Emission zone characterization

The knowledge of the emission zone profile and its bias-dependence can have a significant influence on the OLED efficiency.³¹ Therefore, the emission zone profile was determined in the optically detuned OLED from angle-dependent, s-polarized EL spectra measurements using a purely optical model as described earlier.³² The optical model nicely reproduces the measured

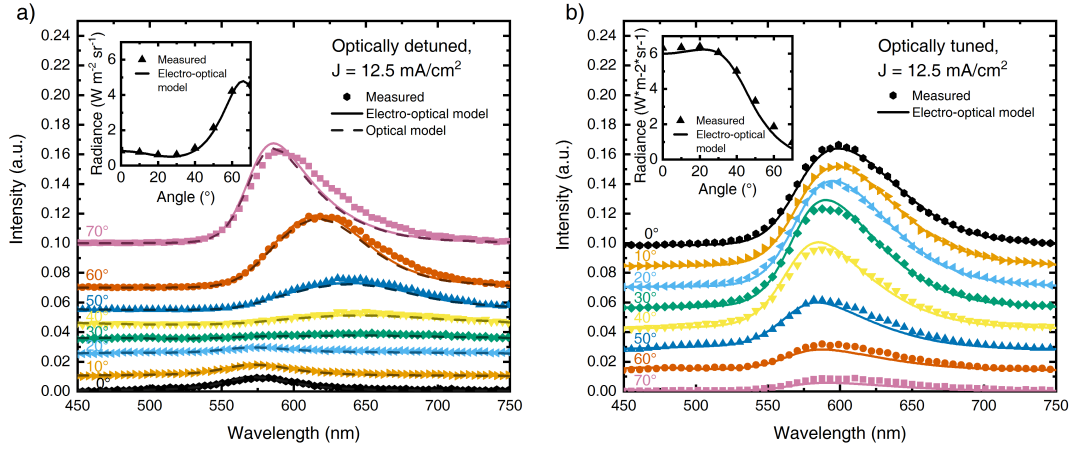


Figure 4.4 – Angle-dependent *s*-polarized EL spectra at 12.5 mA/cm^2 for optically detuned (a) and tuned (b) OLEDs obtained from measurements (symbols), the optical model (dashed lines) and the electro-optical model (solid lines). The insets show the measured and simulated integrated intensity (radiance) over the emission angle.

angle-dependent EL spectra shown in **Figure 4.4a**, and yields the EMZ profile shown in **Figure 4.5**. Determining the emission zone at a larger current density revealed essentially the same emission zone as for the lower current density (cf. Figure S4.3). The bias independent EMZ implies that the field dependence of the electron and the hole mobility is similar, otherwise a significant shift of the EMZ is expected as reported on in a previous study on a phosphorescent OLED.¹⁹

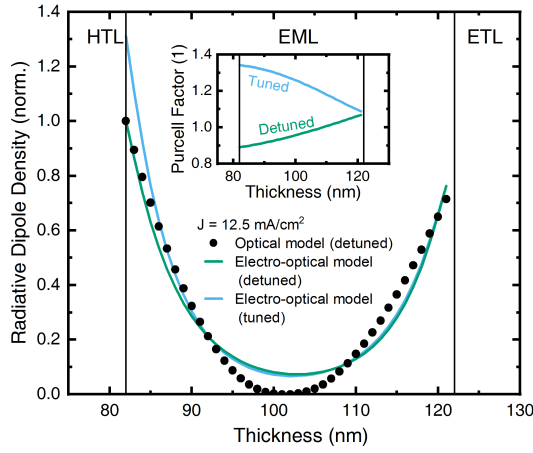


Figure 4.5 – Radiative dipole density (emission zone) in the detuned and the tuned OLED obtained from the optical model (symbols) and the electro-optical model (lines).

The angle-dependent EL spectra and the EMZ profile can also be obtained from the electro-optical model. Figure 4.4 shows the excellent agreement of the simulated EL spectra with the measurements for the detuned and tuned OLEDs, and the insets to Figure 4.4 show the

measured and simulated angle-dependent radiance illustrating the strong influence of the optical detuning on the radiation pattern. The agreement between the EMZ profile in the detuned OLED obtained from the purely optical model and the one obtained from the electro-optical model (cf. Figure 4.5) highlights the validity of the electro-optical model. The width of the measured EMZ was used to estimate the exciton diffusion constant, thus the measurements in the detuned OLED were essential to set this important model parameter. The inset to Figure 4.5 shows the Purcell factor, which is significantly larger at the HTL/EML interface in the tuned OLED, which causes the increased radiative dipole density at the HTL/EML interface in the tuned OLED compared to the detuned OLED.

Interestingly, a split emission zone was obtained, where large exciton densities are present at both interfaces of the EML^{19,33,34}. This is explained by the good charge injection into the EML from the transport layers and the good charge blocking at the opposite EML interface, which leads to an accumulation of electrons and holes at the respective interfaces and an increased exciton density via Langevin recombination. The presence of a split emission zone is substantiated by the occurrence of an EL turn-off peak as discussed next. We note that in very similar systems^{26,35}, no such turn-off peak and a homogeneous emission zone were observed, thus the emission zone profile appears to depend sensitively on the OLED stack.

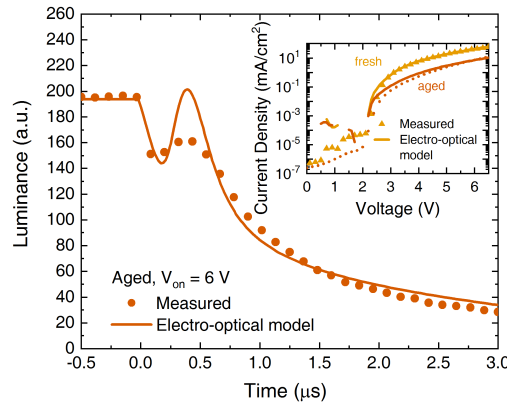


Figure 4.6 – Measured and simulated EL decay for an on-voltage of 6 V of the aged, optically tuned OLED. The peak at 0.4 μ s after turn-off signifies the presence of a split emission zone. The inset shows the measured and simulated current density-voltage curves for the fresh and the degraded OLED.

In a recent study¹⁹ we have shown that the occurrence of a peak in the EL decay after the OLED is turned off³⁶ is a hallmark of a split emission zone. Therefore, **Figure 4.6** shows the measured and simulated EL decay of the tuned OLED. Unfortunately, the EL decay was measured in an aged device with significantly reduced current at a given voltage as shown in the inset to Figure 4.6. To model the degradation, we included hole traps in the HTL and reduced the (non-)radiative rates of the fluorescent emitter. The simulation of the EL decay agrees only qualitatively with the measurements because the EL decay was not included as a fit target during optimization of the model parameters. Nevertheless, these measurements

strongly support the findings of a split emission zone in our TADF OLEDs and suggest that split emission zones occur in phosphorescent[17] and TADF OLEDs alike.

Efficiency enhancement routes

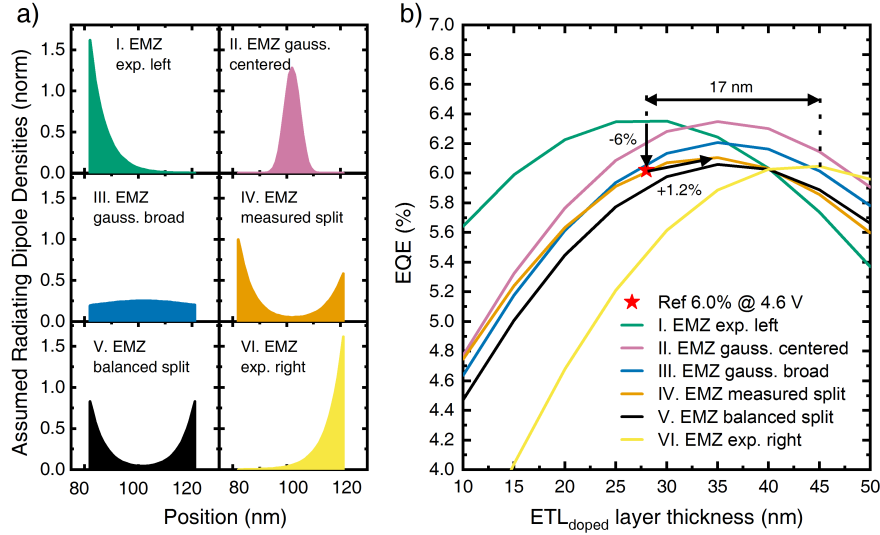


Figure 4.7 – Influence of emission zone profiles (a) on the EQE (b) as obtained from optical simulations. Depending on the EMZ profile, the optimum thickness can vary up to 17 nm resulting in a 6% change of the EQE. The marker indicates the tuned OLED described in this study.

Assuming an exponentially decaying EMZ with a maximum at the HTL/EML interface (profile I in **Figure 4.7a**), an optimum thickness of 28 nm is obtained (green line in **Figure 4.7b**). The measurements on the detuned OLED, as well as the electro-optical model, revealed a split emission zone (profile IV in **Figure 4.7a**), which results in a reduction of 6% in EQE for this layer thickness. Using the correct profile, an optimal thickness of 35 nm is obtained, which increases the EQE by 1.2% with respect to the fabricated OLED as indicated in **Figure 4.7b**.

If the EMZ would have a maximum at the EML/ETL interface (profile VI in **Figure 4.7a**), the thickness would need to be increased by 17 nm to achieve the highest EQE. The other profiles shown in **Figure 4.7a** result in a similar EQE variation, where the maximum EQE can be obtained from EMZ with a maximum emission in the center of the EML (profile II) or at the HTL/EML interface (profile I). Tuning the charge carrier mobilities in the host, respectively their field dependence, together with the energy barriers at the EML interfaces can, thus, provide a means to optimize the EQE. These simulations emphasize the importance of knowing the exact emission zone profile when optimizing the layer stack. We like to point out that the EMZ profile not only influences the light outcoupling as simulated in **Figure 4.7**, but also exciton quenching. The influence of exciton quenching was not included in the simulations leading to **Figure 4.7b**, but will be discussed next.

In **Figure 4.8**, the influence of various model parameters on the EQE are shown, where the orange line in all panels indicates the baseline simulations discussed above reproducing the experimental OLED data. Both non-radiative pathways on the host are sufficiently slow so that their influence on improving the EQE is negligible and are, thus, not shown. When varying the degree of horizontal orientation of the emitting dipoles (EDO) as shown in Figure 4.8a, the EQE is increased by essentially the same amount at all luminance levels. At 1000 cd/m^2 this increase amounts to 22% which motivates further optimization of the dipole orientation.

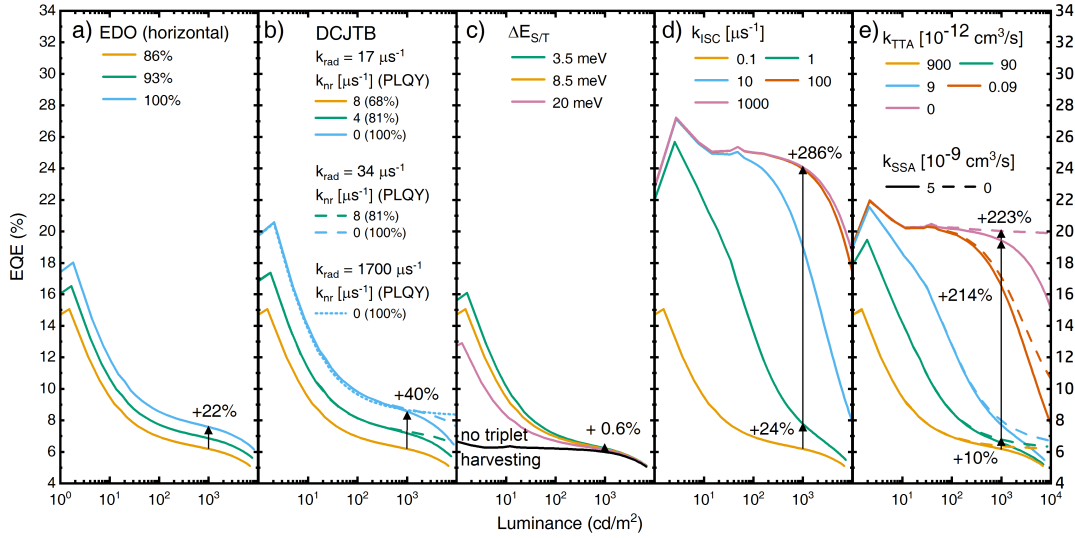


Figure 4.8 – Influence of selected model parameters on EQE. The largest improvements can be realized by increasing the intersystem crossing rate k_{ISC} and by reducing the triplet-triplet annihilation rate.

A larger increase in EQE can be obtained when the photoluminescence quantum yield (PLQY) of the DCJTb emitter is increased. The change of PLQY was modeled by either decreasing the non-radiative decay rate k_{nr} in the emitter (solid lines in Figure 4.8b) or by increasing the radiative decay rate k_{rad} (broken lines in Figure 4.8b). In both cases, the EQE increases essentially by the same value at all luminance values up to $\approx 1000 \text{ cd/m}^2$ with increasing PLQY. To increase the EQE at even higher luminance levels, the radiative decay rate needs to be larger. A twofold increase of k_{rad} is already sufficient to increase the EQE at high luminance levels (dashed line in Figure 4.8b), and a further increase to very high values (dotted line in Figure 4.8b) does not bring a significant benefit.

In Figure 4.8c, the influence of the energy barrier $\Delta E_{S/T}$ is shown. In the chosen exciplex host, this value of 8.5 meV is already very low, and a further reduction to 3.5 meV only marginally increases the EQE by 0.6% at 1000 cd/m^2 . At room temperature, energy barriers of 20 meV are already very effective in harvesting triplets at low luminance levels.

Another parameter describing the triplet harvesting process is the intersystem-crossing rate

k_{ISC} , which influences the reverse intersystem-crossing rate k_{RISC} according to equation 4.1. Figure 4.8d shows a pronounced drop in EQE at low luminance levels in the fabricated OLED. A tenfold increase in k_{ISC} strongly influences the EQE at lower luminance values, and at 1000 cd m^{-2} this increase amounts to 24%. Increasing the intersystem crossing rate further extends the high EQE range to larger luminance values. Increasing k_{ISC} beyond $100\text{ }\mu\text{s}^{-1}$ has no significant effect on the EQE. The rationale for this increase is that the host singlet density is rather low due to the very efficient transition of host singlets to guest singlets ($k_{FRET/DEX}$ in Figure 4.2). Thus, the increased intersystem crossing has a minor influence on the triplet density, and the increased triplet harvesting through reverse intersystem crossing dominates the effect on EQE.

Two additional influential model parameters are the triplet-triplet exciplex annihilation rate k_{TTA} on the host and the singlet-singlet exciton annihilation rate k_{SSA} on the guest as illustrated in Figure 4.8e. A tenfold decrease in k_{TTA} increases the EQE by 10% at 1000 cd m^{-2} . Lowering the value of k_{TTA} reveals a plateau in EQE with a drop-off at high luminance values, even if triplet-triplet annihilation on the host is completely turned-off. Reducing k_{SSA} on the other hand, influences the EQE at high luminance values (dashed lines in Figure 4.8e). If both mechanisms are turned-off, no EQE roll-off at high luminance is observed. A low triplet density on the host is, thus, critical for device efficiency. To realize a high efficiency, a fast intersystem crossing rate and a reduced host TTA are essential. Besides reducing the TTA rate itself, tailoring the charge carrier mobilities to obtain a broad emission zone might also provide a pathway to enhanced efficiencies. In a best case scenario, where all efficiency enhancements predicted in Figure 4.8 can be realized, the model predicts an EQE of $\approx 42\%$ even at high brightness of 1000 cd/m^2 (cf. Figure S4.5).

Conclusion

In conclusion, a comprehensive electro-optical model of an OLED with a TADF exciplex host and a fluorescent emitter was presented. The model considers charge transport, accounts for the full exciton dynamics including the triplet harvesting effect and light out-coupling. The investigated state-of-the-art OLEDs show EQEs $>10\%$ at low bias. Measurements reveal a split emission zone with high radiating dipole densities at both interfaces of the emission layer, which is nicely reproduced by the model. With the knowledge of the emission zone profile, the layer stack can be more accurately optimized for maximum efficiency. A parameter study showcases the effects of various model parameters on the efficiency. The most influential parameters are the (reverse) intersystem crossing rates between the singlet and triplet states on the host, and the triplet-triplet annihilation rate on the host. This work shows that electro-optical device modelling is a powerful tool to elucidate the details of charge carrier and exciton dynamics in TADF OLEDs and to guide future materials and device development.

Experimental Section

The fabrication details of the investigated optically tuned and detuned OLEDs are described in detail in Reference¹³.

All electro-optical measurements were taken with the all-in-one measurement system Paios and the Characterization Suite 4.2 from Fluxim.³⁷ For measuring the transient EL decay, a gated photomultiplier (H11526 Series) from Hamamatsu was used. The angle-dependent EL spectra were measured with a home-built goniometer add-on to Paios.¹⁹ The goniometer used a cylindrical lens to prevent light trapping due to total internal reflection in the glass substrate. The current efficiency was calculated from the steady-state luminance and the current density.

Acknowledgements

We thank S. Jenatsch, B. Blülle, S. Züfle, A. Stous and A. Gentsch from Fluxim AG and J. Dunst and C. Kirsch from ZHAW for fruitful discussions and valuable comments. Financial support from the Swiss National Science Foundation under grant no. 162230 as well as from Korean National Research Foundation (KNRF) is gratefully appreciated.

References

1. Endo, A. *et al.* Efficient up-conversion of triplet excitons into a singlet state and its application for organic light emitting diodes. *Applied Physics Letters* **98**, 083302 (Feb. 21, 2011).
2. Hirata, S. *et al.* Highly efficient blue electroluminescence based on thermally activated delayed fluorescence. *Nature Materials* **14**. 00021, 330–336 (Dec. 8, 2014).
3. Uoyama, H., Goushi, K., Shizu, K., Nomura, H. & Adachi, C. Highly efficient organic light-emitting diodes from delayed fluorescence. *Nature* **492**. 00452, 234–238. <http://www.nature.com/nature/journal/v492/n7428/abs/nature11687.html> (Dec. 13, 2012).
4. Zhang, Q. *et al.* Efficient blue organic light-emitting diodes employing thermally activated delayed fluorescence. *Nature Photonics* **8**. 00137, 326–332 (Mar. 2, 2014).
5. Nakanotani, H. *et al.* High-efficiency organic light-emitting diodes with fluorescent emitters. *Nature Communications* **5**. 00053. <http://www.nature.com/ncomms/2014/140530/ncomms5016/full/ncomms5016.html> (May 30, 2014).
6. Lin, T.-A. *et al.* Sky-Blue Organic Light Emitting Diode with 37% External Quantum Efficiency Using Thermally Activated Delayed Fluorescence from Spiroacridine-Triazine Hybrid. *Advanced Materials (Deerfield Beach, Fla.)* **28**, 6976–6983 (Aug. 2016).
7. Sun, J. W. *et al.* A Fluorescent Organic Light-Emitting Diode with 30% External Quantum Efficiency. *Advanced Materials* **26**. 00045, 5684–5688 (Aug. 1, 2014).

8. Moon, C.-K. *et al.* Combined Inter- and Intramolecular Charge-Transfer Processes for Highly Efficient Fluorescent Organic Light-Emitting Diodes with Reduced Triplet Exciton Quenching. *Advanced Materials* **29**, 1606448 (2017).
9. Kim, K.-H. & Kim, J.-J. Origin and Control of Orientation of Phosphorescent and TADF Dyes for High-Efficiency OLEDs. *Advanced Materials* **30** (Oct. 1, 2018).
10. Byeon, S. Y., Lee, D. R., Yook, K. S. & Lee, J. Y. Recent Progress of Singlet-Exciton-Harvesting Fluorescent Organic Light-Emitting Diodes by Energy Transfer Processes. *Advanced Materials*, 1803714 (Feb. 13, 2019).
11. Furukawa, T., Nakanotani, H., Inoue, M. & Adachi, C. Dual enhancement of electroluminescence efficiency and operational stability by rapid upconversion of triplet excitons in OLEDs. *Scientific Reports* **5**. 00006. http://www.nature.com/srep/2015/150212/srep08429/full/srep08429.html?WT.ec_id=SREP-639-20150217 (Feb. 12, 2015).
12. Li, D., Hu, Y. & Liao, L.-S. Triplet exciton harvesting by multi-process energy transfer in fluorescent organic light-emitting diodes. *Journal of Materials Chemistry C* **7**, 977–985. <https://pubs.rsc.org/en/content/articlelanding/2019/tc/c8tc05141k> (2019).
13. Kim, K.-H., Moon, C.-K., Sun, J. W., Sim, B. & Kim, J.-J. Triplet Harvesting by a Conventional Fluorescent Emitter Using Reverse Intersystem Crossing of Host Triplet Exciplex. *Advanced Optical Materials* **3**. 00000, 895–899 (July 1, 2015).
14. Gottardi, S., Barbry, M., Coehoorn, R. & van Eersel, H. Efficiency loss processes in hyperfluorescent OLEDs: A kinetic Monte Carlo study. *Applied Physics Letters* **114**, 073301 (Feb. 18, 2019).
15. Mayr, C., Schmidt, T. D. & Brütting, W. High-efficiency fluorescent organic light-emitting diodes enabled by triplet-triplet annihilation and horizontal emitter orientation. *Applied Physics Letters* **105**. 00002, 183304 (Nov. 3, 2014).
16. Flämmich, M., Michaelis, D. & Danz, N. *In situ measurement of spectrum, emission zone, and dipole emitter orientation in OLEDs in Light-Emitting Diodes: Materials, Devices, and Applications for Solid State Lighting XV* (eds Streubel, K. P., Jeon, H., Tu, L.-W. & Linder, N.) **7954** (Proc. of SPIE, Feb. 2011), 7954101. (2016).
17. Perucco, B. *et al.* On the exciton profile in OLEDs-seamless optical and electrical modeling. *Organic Electronics* **13**, 1827–1835. <http://www.sciencedirect.com/science/article/pii/S1566119912002534> (Oct. 1, 2012).
18. Perucco, B., Reinke, N. A., Müller, F., Rezzonico, D. & Ruhstaller, B. *The influence of the optical environment on the shape of the emission profile and methods of its determination in Organic Photonics IV* (eds Heremans, P. L., Coehoorn, R. & Adachi, C.) **7722**. 00002 (Proc. of SPIE, Apr. 2010), 77220F1. (2016).
19. Regnat, M., Pernstich, K. P., Züfle, S. & Ruhstaller, B. Analysis of the Bias-Dependent Split Emission Zone in Phosphorescent OLEDs. *en. ACS Applied Materials & Interfaces* **10**, 31552–31559. ISSN: 1944-8244, 1944-8252. <http://pubs.acs.org/doi/10.1021/acsami.8b09595> (2018) (Sept. 2018).
20. *Setfos 5.0, Fluxim Fluxim*. 00000. <https://www.fluxim.com/setfos-intro/>.

21. Ruhstaller, B. *et al.* in *Optoelectronic Devices and Properties*, edited by Oleg Sergiyenko, ISBN 978-953-307-204-3, DOI: 10.5772/14626 00009 (2011). (2017).
22. Ruhstaller, B. *et al.* Simulating electronic and optical processes in multilayer organic light-emitting devices. *IEEE Journal of Selected Topics in Quantum Electronics* **9**, 723–731 (May 2003).
23. Ruhstaller, B. *et al.* Transient and steady-state behavior of space charges in multilayer organic light-emitting diodes. *Journal of Applied Physics* **89**. 00224, 4575–4586 (Apr. 15, 2001).
24. Wu, S.-F. *et al.* White Organic LED with a Luminous Efficacy Exceeding 100 lm W⁻¹ without Light Out-Coupling Enhancement Techniques. *Advanced Functional Materials* **27**, 1701314 (Aug. 1, 2017).
25. Kim, K.-H., Yoo, S.-J. & Kim, J.-J. Boosting Triplet Harvest by Reducing Nonradiative Transition of Exciplex toward Fluorescent Organic Light-Emitting Diodes with 100% Internal Quantum Efficiency. *Chemistry of Materials* **28**, 1936–1941 (Mar. 22, 2016).
26. Park, Y.-S. *et al.* Exciplex-Forming Co-host for Organic Light-Emitting Diodes with Ultimate Efficiency. *Advanced Functional Materials* **23**. 00067, 4914–4920 (2013).
27. Borsenberger, P. M., Pautmeier, L., Richert, R. & Bässler, H. Hole transport in 1,1-bis(di-4-tolylaminophenyl)cyclohexane. *The Journal of Chemical Physics* **94**, 8276–8281 (June 15, 1991).
28. Noh, S., Suman, C. K., Hong, Y. & Lee, C. Carrier conduction mechanism for phosphorescent material doped organic semiconductor. *Journal of Applied Physics* **105**, 033709 (Feb. 1, 2009).
29. Yokoyama, D., Sasabe, H., Furukawa, Y., Adachi, C. & Kido, J. Molecular Stacking Induced by Intermolecular C–H···N Hydrogen Bonds Leading to High Carrier Mobility in Vacuum-Deposited Organic Films. *Advanced Functional Materials* **21**, 1375–1382 (2011).
30. Zhao, B. *et al.* Highly efficient red OLEDs using DCJTb as the dopant and delayed fluorescent exciplex as the host. *Scientific Reports* **5**, srep10697. <https://www.nature.com/articles/srep10697> (May 29, 2015).
31. Regnat, M., Pernstich, K. P. & Ruhstaller, B. Influence of the bias-dependent emission zone on exciton quenching and OLED efficiency. *Organic Electronics* **70**, 219–226. <http://www.sciencedirect.com/science/article/pii/S1566119919301922> (July 1, 2019).
32. Perucco, B., Reinke, N. A., Rezzonico, D., Moos, M. & Ruhstaller, B. Analysis of the emission profile in organic light-emitting devices. *Optical Society of America* **18**. 00013, A246. http://www.opticsinfobase.org/view_article.cfm?gotourl=http%3A%2F%2Fwww%2Eopticsinfobase%2Eorg%2FDirectPDFAccess%2FBD2DC44F%2DDC94%2DF2EE%2D639CB01A65261B00%5F202487%2Foe%2D18%2DS2%2DA246%2Epdf%3Fda%3D1%26id%3D202487%26seq%3D0%26mobile%3Dno&org= (S2 June 21, 2010).
33. Berner, D. *et al.* Splitting of the recombination zone in organic light emitting diodes by dye doping. *Journal of Applied Physics* **95**, 3749 (Mar. 18, 2004).

34. Eersel, H. v., Bobbert, P. A., Janssen, R. a. J. & Coehoorn, R. Effect of Förster-mediated triplet-polaron quenching and triplet-triplet annihilation on the efficiency roll-off of organic light-emitting diodes. *Journal of Applied Physics* **119**, 163102 (Apr. 28, 2016).
35. Sim, B., Moon, C.-K., Kim, K.-H. & Kim, J.-J. Quantitative Analysis of the Efficiency of OLEDs. *ACS Applied Materials & Interfaces* **8**. 00000, 33010–33018 (Dec. 7, 2016).
36. Reineke, S. *et al.* Measuring carrier mobility in conventional multilayer organic light emitting devices by delayed exciton generation. *physica status solidi (b)* **245**, 804–809 (May 1, 2008).
37. *Characterization Suite* Fluxim. <https://www.fluxim.com/news/2018/5/4/characterization-suite-41-released> (2019).

4.1 Supporting Information

Routes for Efficiency Enhancement in Fluorescent TADF Exciplex Host OLEDs gained from an Electro-Optical Device Model

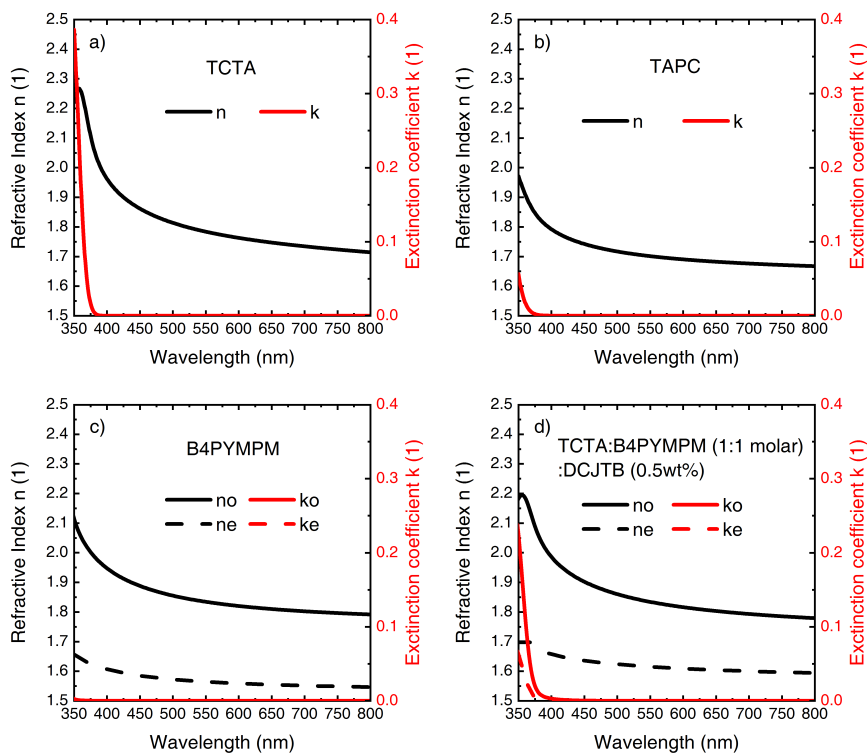


Figure S4.1 – Refractive indices used in the electro-optical model for the different organic layers. For the birefringent ETL material B4PYMPM (c) and also for the emitting layer TCTA:B4PYMPM:DCJTB (d) ordinary and extraordinary refractive indices (n or n_o , n_e) and absorption (k or k_o , k_e) are used. Data were taken from¹

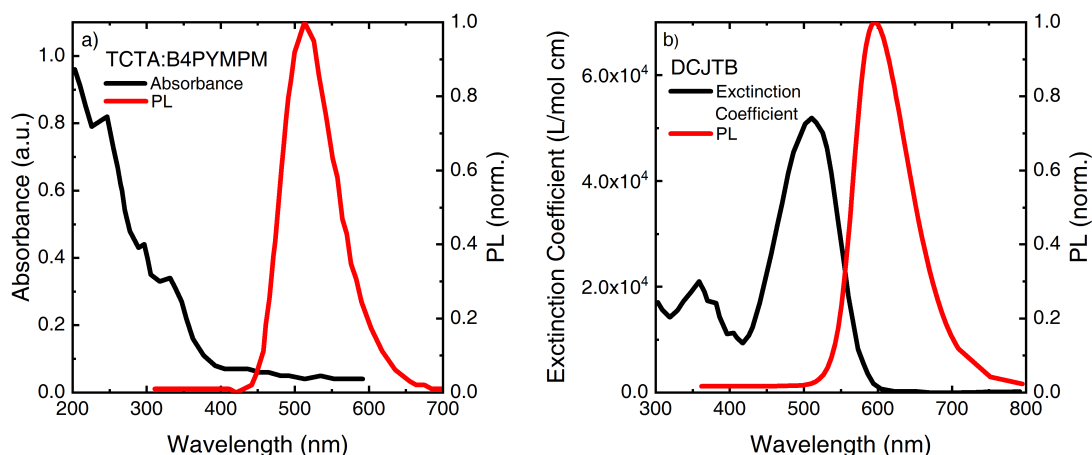


Figure S4.2 – Absorbance and PL spectrum of TCTA:B4PYMPM TADF exciplex host film (a) showing no significant spectral overlap of absorption and emission. DCJTb extinction coefficient spectra measured in solution (b) together with the PL spectrum of DCJTb doped in TCTA:B4PYMPM film indicating a significant spectral overlap of absorption and emission. Data were taken from Reference², where the DCJTb PL spectrum was extracted from the DCJTb:Exciplex PL spectrum and corrected for the minute host emission.

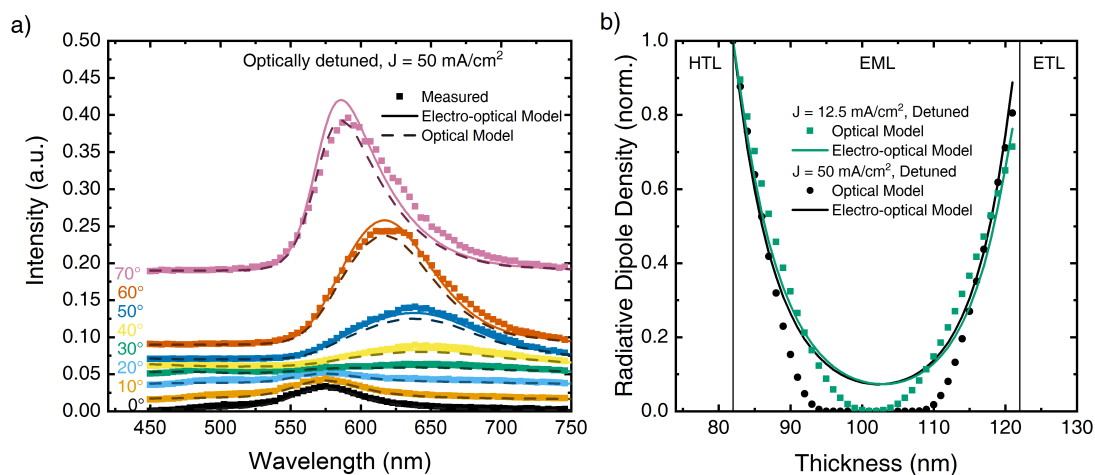


Figure S4.3 – Angle-dependent s-polarized EL spectra (a) at 50 mA/cm² for the tuned OLEDs obtained from measurements (symbols), the optical model (dashed lines) and the electro-optical model (solid lines). Radiative dipole densities (b) in the detuned and the tuned OLED obtained from measurements (dots), the optical model (symbols), and the electro-optical model (lines) at 12.5 and 50 mA/cm².

Exciplex/exciton dynamics modelling

In the electro-optical model the exciplex and exciton dynamics are modelled using the exciplex continuity equations for host singlet states S_h (equation S4.1), host triplet states T_h (equation S4.2), and the exciton continuity equation for guest singlet states S_g (equation S4.3).

$$\begin{aligned} \frac{dS_h(t, z)}{dt} = & g_S \cdot R(t, z) - k_{ISC} \cdot S_h(t, z) + k_{RISC} \cdot \exp\left(\frac{-\Delta E_{S/T}}{k_B T}\right) \cdot T_h(t, z) \\ & - k_{FRET/DEX} \cdot S_h(t, z) - (F(z) \cdot k_{rad, Sh} + k_{nr, Sh}) \cdot S_h(t, z) \end{aligned} \quad (S4.1)$$

$$\begin{aligned} \frac{dT_h(t, z)}{dt} = & g_T \cdot R(t, z) + k_{ISC} \cdot S_h(t, z) - k_{RISC} \cdot \exp\left(\frac{-\Delta E_{S/T}}{k_B T}\right) \cdot T_h(t, z) \\ & - k_{nr, Th} \cdot T_h(t, z) - k_{TTA} \cdot T_h(t, z)^2 \end{aligned} \quad (S4.2)$$

$$\begin{aligned} \frac{dS_g(t, z)}{dt} = & \vec{\nabla} (D_{Sg} \vec{\nabla} S_g(t, z)) + k_{FRET/DEX} \cdot S_h(t, z) \\ & - (F(z) \cdot k_{rad, Sg} + k_{nr, Sg}) \cdot S_g(t, z) - k_{SSA} \cdot S_g(t, z)^2 \end{aligned} \quad (S4.3)$$

Exciton/exciple formation was only allowed on the host and modelled with the generation terms $g_S \cdot R(t, z)$ and $g_T \cdot R(t, z)$. The factors g_S and g_T account for the spin statistics ratio of singlet/triplet formation and R represents the Langevin recombination rate, which is proportional to the time- (t) and position- (z) dependent electron and hole density in the EML ($R \propto n(t, z) \cdot p(t, z)$).³ The (reverse) intersystem crossing between host singlet and triplet states is modeled with the terms $k_{ISC} \cdot S_h(t, z)$ and $k_{RISC} \cdot \exp\left(\frac{-\Delta E_{S/T}}{k_B T}\right) \cdot T_h(t, z)$, where k_{ISC} and k_{RISC} are the intersystem crossing and reverse intersystem crossing rate constants and $\Delta E_{S/T}$ is the energy difference between those states. The transfer from host singlets to guest singlets is described with the terms $k_{FRET/DEX} \cdot S_h(t, z)$, where $k_{FRET/DEX}$ is the rate constant representing Förster resonance or Dexter energy transfer mechanism. Exciton diffusion was only allowed for the guest singlet excitons inside the EML and modelled with the diffusion constant D_{Sg} . Fig. S4.4 shows the exciton and exciplex densities at 1000 cd/m^2 . These densities are orders of magnitude below the molecular density of 10^{27} m^{-3} in the host and of 10^{25} m^{-3} in the guest, hence, there was no need to include saturation effects.

The radiative recombination of singlet exciplexes on the host and singlet excitons on the guest are described with the rate constants $k_{rad, Sh}$ and $k_{rad, Sg}$, which are modified by the position-dependent Purcell factor $F(z)$. The triplet exciplexes on the host were not allowed to radiatively recombine as suggested in⁴. The non-radiative recombination of the host exciplexes and the guest exciton are modeled with the rate constants $k_{nr, Sh}$, $k_{nr, Th}$ and $k_{nr, Sg}$.

The exciplex and the exciton quenching in the OLED are modeled as triplet-triplet annihilation for the host triplets with a rate constant k_{TTA} and as singlet-singlet annihilation for the guest singlet with a rate constant k_{SSA} .

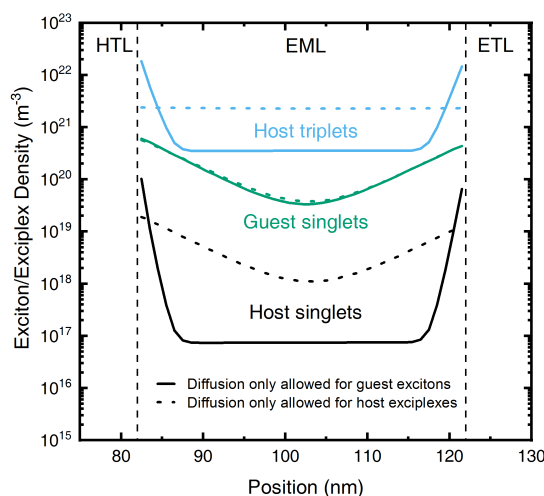


Figure S4.4 – Singlet and triplet exciplex densities in the host and singlet exciton density in the guest at 1000 cd/m^2 with a molecular density of 10^{27} m^{-3} in the host and of 10^{25} m^{-3} in the guest. Diffusion was only allowed for guest excitons (solid lines). The same EQE could be obtained when diffusion was enabled only for host exciplexes (dashed lines) with slightly modified model parameters, especially the triplet-triplet annihilation rate on the host.

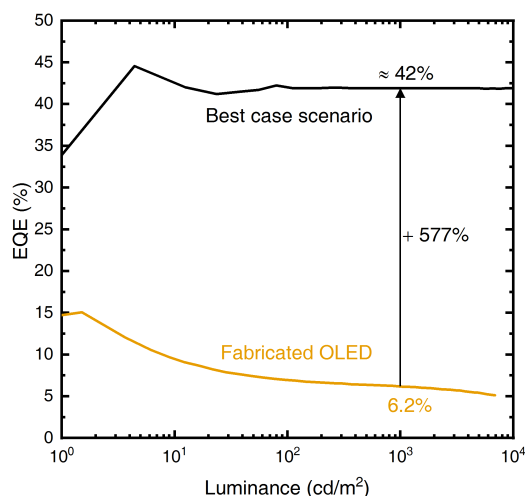


Figure S4.5 – Simulated EQE for fabricated OLED and best case scenario, where all maximum efficiency enhancements from Figure 4.8 are used in the model.

Chapter 4. Prediction of Efficiency Enhancement in TADF OLEDs

Table S4.1 – Mobility parameters for electrons (*e*) and holes (*h*) used in the electro-optical model.

Layer	Zero-field mobility μ_0^\dagger [cm ² /Vs]	Field coefficient γ^\dagger [cm ^{0.5} /V ^{0.5}]	Reference
TAPC	$\mu_{0_e} = 1\text{e-}15$ $\mu_{0_h} = 6.19\text{e-}3$	$\gamma_e = 1\text{e-}8$ $\gamma_h = 3.03\text{e-}4$	⁵
TCTA	$\mu_{0_e} = 1\text{e-}15$ $\mu_{0_h} = 2\text{e-}4$	$\gamma_e = 1\text{e-}8$ $\gamma_h = 1.15\text{e-}3$	⁶
TCTA:B4PYMPM:DCJTB	$\mu_{0_e} = 1.05\text{e-}5$ $\mu_{0_h} = 1.2\text{e-}4$	$\gamma_e = 1.12\text{e-}3$ $\gamma_h = 1\text{e-}3$	Adjusted to experiment Adjusted to experiment
B4PYMPM	$\mu_{0_e} = 1.5\text{e-}5$ $\mu_{0_h} = 1\text{e-}15$	$\gamma_e = 1.12\text{e-}3$ $\gamma_h = 1\text{e-}8$	¹
B4PYMPM _{doped}	$\mu_{0_e} = 1\text{e-}4$ $\mu_{0_h} = 1\text{e-}15$	$\gamma_e = 0$ $\gamma_h = 0$	Adjusted to experiment

[†] $\mu = \mu_0 \cdot e^{\gamma\sqrt{E}}$ with μ_0 zero field mobility, γ field-dependence coefficient and E electric field.

5 Conclusion

In this thesis phosphorescence-based OLEDs and fluorescent TADF exciplex host OLEDs were electro-optically characterized with various measurement techniques. In combination with electro-optical simulations the emission zone and the dynamics of exciton energy transfer were analyzed to elucidate the physical operating mechanisms in these OLEDs. Based on these findings a comprehensive OLED device model was established that accurately reproduced the electro-optical characteristics of the investigated OLEDs and thus allowed the identification of possible efficiency enhancement routes. The highlights of the three studies in this thesis are summarized in section 5.1 and topics for future research discussed in section 5.2.

5.1 Achieved results and impact

In the first study (chapter 2), the emission zone profile in the phosphorescence-based OLED type was determined by s-polarized angle-dependent EL spectra that were measured with a self-built goniometer and analyzed with optical simulations for an optically detuned OLED stack configuration. One highlight of the study was the identification of a bias-dependent split emission zone with high radiative dipole densities at both sides in the 35 nm thin emission layer. At low bias the emission was mainly originating from the cathode side, whereas at high bias the maximum emission was originating from the anode side of the emission layer. At intermediate biases a balanced split emission zone was obtained. Another highlight was the fact that the observation of an EL peak after turn-off the OLED with a negative bias in transient EL measurements could be verified as a hallmark for the determined split emission zone by means of a qualitative electro-optical model.

In the following second study (chapter 3), the influence of the bias-dependent split emission zone on the exciton quenching and on the OLED current efficiency was analyzed in detail. Through a model parameter optimization algorithm the current-voltage-luminance and current efficiency curves as well as transient EL data could be quantitatively reproduced. The electro-optical device model revealed that the measured, surprising initial increase of the current efficiency for increasing bias is caused by a reduction of the triplet polaron quenching due to the evolution of the emission zone. Furthermore the device model revealed that the

efficiency roll-off for increasing biases is not only caused by the often reported triplet-triplet annihilation, but also by a reduction of the light outcoupling efficiency due to the shift of the emission zone maximum from the cathode side to the anode side of the emission layer. The final highlight of this study was that the analysis of the transient EL decay after turn-off in regard to exciton quenching should be carried out with caution due to a possible hidden contribution of the emission zone shift or of delayed formation of excitons due to residual carriers in the device.

In the third study (chapter 4), fluorescent TADF exciplex host OLEDs with EQEs greater than 10% provided from our Korean project partner were investigated. To this purpose the previously built electro-optical device model was extended to include the triplet harvesting mechanism in the exciplex host and the subsequent energy transfer from the host singlet state to the guest singlet state. With this comprehensive device model, the current-voltage-luminance, current efficiency, transient EL decay measurements, as well as angle-dependent EL spectra were accurately reproduced for optically tuned and detuned OLED devices. As indicated by an EL turn-off peak in the transient EL decay measurements, the emission zone analysis again revealed a split emission zone in these TADF OLEDs. For this kind of OLED high EQE values can only be achieved at low current density and low brightness levels. An additionally performed model parameter study identified several promising routes to a further increase of the EQE for these OLEDs. A main focus should be put on a better harvesting of the triplet exciplexes on the host. The model showed EQE improvements of more than 200% at high luminance values for either strongly increased reverse intersystem crossing rate from triplet state to singlet state or strongly reduced triplet-triplet annihilation on the exciplex host.

The novelty of this work lies in the detailed analysis of exciton dynamics in OLED emission layers with spatial resolution and its impact on device efficiency. Previously, electrical modeling of OLEDs was carried out with charge drift-diffusion already but the dynamics of excitons was mostly characterized with rate equations in zero dimension. Moreover, previous studies on OLED device physics have mostly focused on analyzing one or two experimental measurement techniques. In this work we take advantage of various measurement techniques in DC and transient state and additionally exploit the information contained in the angular OLED emission spectra. The latter is used to determine the emission zone or exciton profile inside the emission layer, thus enabling a validation of the electrical model. Thereby we achieve a comprehensive analysis of OLED operation mechanisms in a non-invasive way. If these analysis methods would be repeated periodically during ongoing degradation one could likely identify the origin of limited OLED stability especially for emerging high-efficiency OLED materials with limited device lifetime.

5.2 Outlook

From the third study in chapter 4, the main result is that the triplex exciplexes formed in the host should be harvested more efficiently for further EQE enhancement. A recent study¹

from our Korean project partner applying a TADF assistant dopant in the same OLED stack for improved triplet harvesting showed an increase of the OLED efficiency by 21%. Thus the introduction of an assistant dopant to the comprehensive device model, followed by a comparison of the simulation results to experimental data could verify the predictions made in chapter 4.

Moreover, the conduction of temperature dependent measurements and the implementation of temperature- and field-dependent mobilities could allow for a determination of the singlet-triplet energy split and an accurate description of temperature-dependent transient EL decay, which can then be used for a better understanding of triplet harvesting process. This is especially critical if two TADF mechanisms (TADF exciplex host and TADF assistant dopant) are involved in the OLED device operation. Including also the turn-on behavior of the transient EL signal further insights on the exciton and charge carrier dynamics could be gained.

It is known that the distance and thus the orientation of the molecules to each other influences the intermolecular transition rates. With Phelos, the further developed, commercial version of the goniometer built in this work, where PL measurements can be performed, additional dipole orientation studies on the TADF assistant dopant in the TADF exciplex host could be carried out for a more thorough analysis of the TADF mechanisms and light outcoupling efficiency in these OLEDs. In that context one may also consider to model the exciton energy transfer dynamics in 3D in conjunction with a 1D model for charge transport and recombination.

In this work we have performed the characterization of bottom-emission OLEDs with a limited number of devices and variations thereof. Particularly, only the electron transport layer was varied to study both optically tuned and detuned OLEDs, as recommended for accurate determination of the emission zone. The material parameters of the comprehensive electro-optical model were established by a global fit with various measured data sets of a single OLED. In future work it would be interesting to fabricate additional, simplified devices e.g. to analyze single-carrier transport in critical layers of the OLEDs² or investigate the excitonic parameters in photoluminescence experiments with OLED films with or without simultaneous current flow. This may allow to further confirm the material parameters obtained with the methods of this work and arrive at a recipe for determination of the key model parameters step by step. Moreover, the inclusion of frequency-domain data in the analysis, in particular capacitance-frequency and capacitance-voltage data, would certainly provide further insight³⁻⁸. Further research will hopefully tell whether more non-invasive experiments with a single or few OLEDs rather than few, dedicated experiments with a variety of device structures allow for a more reliable and fast determination of the OLED model parameters.

Another major research topic, besides the efficiency enhancement, is the operational stability in today's OLEDs, which is typically investigated with stress test experiments combined with electro-optical characterization. Having a comprehensive device model at hand that can describe the initial fresh devices one could determine possible degradation mechanisms by adjusting the model parameter set to describe the final degraded OLED devices. Currently, stress test measurements are carried out for similar TADF OLEDs as described in chapter 4.

References

1. Li, D., Hu, Y. & Liao, L.-S. Triplet exciton harvesting by multi-process energy transfer in fluorescent organic light-emitting diodes. *Journal of Materials Chemistry C* **7**, 977–985. <https://pubs.rsc.org/en/content/articlelanding/2019/tc/c8tc05141k> (2019).
2. Jenatsch, S. *et al.* Time-Dependent p–i–n Structure and Emission Zone in Sandwich-Type Light-Emitting Electrochemical Cells. *ACS Photonics* **5**, 1591–1598. <https://doi.org/10.1021/acsp Photonics.8b00047> (2018) (Apr. 2018).
3. Knapp, E. & Ruhstaller, B. Numerical impedance analysis for organic semiconductors with exponential distribution of localized states. *Applied Physics Letters* **99**, 093304. ISSN: 0003-6951. <https://aip.scitation.org/doi/abs/10.1063/1.3633109> (2019) (Aug. 2011).
4. Knapp, E. & Ruhstaller, B. The role of shallow traps in dynamic characterization of organic semiconductor devices. *Journal of Applied Physics* **112**, 024519. ISSN: 0021-8979. <https://aip.scitation.org/doi/abs/10.1063/1.4739303> (2019) (July 2012).
5. Knapp, E. & Ruhstaller, B. Analysis of negative capacitance and self-heating in organic semiconductor devices. *Journal of Applied Physics* **117**, 00001, 135501 (Apr. 7, 2015).
6. Züfle, S. *et al.* Determination of charge transport activation energy and injection barrier in organic semiconductor devices. *Journal of Applied Physics* **122**, 115502. ISSN: 0021-8979. <https://aip.scitation.org/doi/abs/10.1063/1.4992041> (2018) (Sept. 2017).
7. Züfle, S. *et al.* The use of charge extraction by linearly increasing voltage in polar organic light-emitting diodes. *Journal of Applied Physics* **121**, 175501. ISSN: 0021-8979. <https://aip.scitation.org/doi/abs/10.1063/1.4982903> (2018) (May 2017).
8. Altazin, S. *et al.* Simulation of OLEDs with a polar electron transport layer. *Organic Electronics* **39**, 244–249. ISSN: 1566-1199. <http://www.sciencedirect.com/science/article/pii/S1566119916304414> (2018) (Dec. 2016).

Markus Regnat

Telephone: +41 (0)79 694 1803

Nationality: German

E-mail: markus.regnat@gmx.de

Personal status: Married

Born: 21.09.84 / Neumarkt i.d. Opf



Work Experience

02/14 – now

Zurich University of Applied Sciences ZHAW, Winterthur, Switzerland

Research assistant at Institute of Computational Physics

- Investigation of light out-coupling, degradation mechanism in OLEDs
- Fabrication, characterization and simulation of OLEDs
- General laboratory work

11/12 – 09/13

Max Planck Institute of Colloids and Interfaces, Golm - Potsdam, Germany

Master Thesis: "Solution Processed Small Molecule Organic Solar Cells"

- Fabrication of Organic Solar Cells via spin coating
- Structure investigation of absorber nanostructures with AFM
- Performance characterization

Presentation of poster at DPG spring meeting 2013 in Regensburg

Grade Master Thesis: 1,5

02/10 - 08/10

Fraunhofer Institute for Solar Energy Systems ISE, Freiburg im Breisgau, Germany

Research assistant at OSC group

- Continuing of diploma thesis work

Co-Autor conference paper:

„ITO-free transparent electrodes for organic solar cells and OLEDs"

09/09 – 01/10

Fraunhofer Institute for Solar Energy Systems ISE, Freiburg im Breisgau, Germany

Diploma Thesis: „Untersuchung neuer Elektrodenmaterialien für Organische Solarzellen"

- Fabrication of Polymer Organic Solar Cells via spin coating
- Investigation of new electrode and buffer materials

Grade Diploma Thesis: 1,0

- 03/08 – 08/08 **OSRAM OS Sdn Bhd, Penang, Malaysia**
2nd praxis semester: R&D Department OLED
- Set up an in-situ measurement for OLEDs
- 09/06 – 01/07 **OSRAM OS GmbH, Regensburg, Germany**
1st praxis semester: APL Department Product technology
- Fabrication of micro-optical components

Education

- 03/15 – now **PhD at École polytechnique fédérale de Lausanne EPFL, Lausanne, Switzerland**
- Doctoral school: Material science and engineering EDMX
- Thesis title: “Characterization and Modelling of the Emission Zone and Exciton Dynamics in Doped Organic Light-Emitting Diodes”
- Doctoral supervisor: Prof. Frank Nüesch
Doctoral co-supervisor: Prof. Beat Ruhstaller
- 04/11 – 09/13 **Joint Master Program (English) of Humboldt -, Free - and Technical University of Berlin and Potsdam University, Germany**
- Study: Polymer Science
- Specialization in Organic Solar Cells
- Degree: Master of Science
Grade Master Thesis: 1,5
- Final grade average: 1,4**
- 09/05 – 03/2010 **Diploma Study (Fh) at University of Applied Science Regensburg, Germany**
- Study: Microsystems – Technology
- Degree: Diplom - Ingenieur (FH)
Grade Diploma Thesis: 1,0
- Final grade average: 1,7**
- 07/04 – 07/05 **Compulsory military service in Oberviechtach, Germany**
- Member of the Nato Response Force
- 09/02 – 07/04 **Maximilian-Kolbe Technical College in Neumarkt i.d. OPf, Germany**
- Mathematical – natural scientific direction

Skills and Interests

LANGUAGES	<ul style="list-style-type: none"> - German (native) - English (fluent) - Spanish (fluent)
IT	<ul style="list-style-type: none"> - MS-Office, Origin, MATLAB, CATIA - SETFOS (OLED & OSC simulation software)
HOBBIES	<ul style="list-style-type: none"> - Play chess, Traveling, Jogging

Publications

2019	Markus Regnat , Kurt P. Pernstich, Kwon-Hyeon Kim, Jang-Joo Kim, Frank Nüesch and Beat Ruhstaller, Routes for Efficiency Enhancement in Fluorescent TADF Exciplex Host OLEDs gained from an Electro-Optical Device Model, Manuscript submitted to Advanced Electronic Materials Journal
2019	Raphaël Monnard, Markus Regnat , Quentin Jeangros, Tilman Beierlein, Lieven Penninck, Kurt P. Pernstich, Beat Ruhstaller, Christophe Ballif, and Monica Morales-Masis, Mapping the design space of metal oxide/metal/metal oxide electrodes for OLEDs: from simulations to proof-of-concept, Manuscript in preparation
2019	M. Regnat , K.P. Pernstich, B. Ruhstaller, Influence of the bias-dependent emission zone on exciton quenching and OLED efficiency, Organic Electronics. 70 (2019) 219–226. doi:10.1016/j.orgel.2019.04.027.
2018	M. Regnat , K.P. Pernstich, S. Züfle, B. Ruhstaller, Analysis of the bias-dependent split emission zone in phosphorescent OLEDs, ACS Applied Materials & Interfaces. (2018). doi:10.1021/acsami.8b09595.
2018	S. Jenatsch, M. Regnat , R. Hany, M. Diethelm, F. Nüesch, B. Ruhstaller, Time-Dependent p–i–n Structure and Emission Zone in Sandwich-Type Light-Emitting Electrochemical Cells, ACS Photonics. 5 (2018) 1591–1598. doi:10.1021/acsphotonics.8b00047.

Conferences

2018	SIMOEP2018, Presentation: “Modelling the bias-dependent emission zone and its influence on the transient electroluminescence and OLED efficiency”, Winterthur, Switzerland.
2018	ICSM2018, Presentation: “Influence of the bias-dependent Emission Zone on the electroluminescence Decay and the OLED Efficiency”, Busan, South Korea.
2017	IKSS summer school 2017, Poster Presentation: “Correlation of mission Zone Shift and Efficiency Roll-off in OLEDs”, Krutyna, Poland.
2016	SimOEP2016, Poster Presentation: “Linking the OLED efficiency roll-off to the change of the emission zone by electro-optical device modelling”, Winterthur, Switzerland.
2016	IMID2016, Presentation: “Determination of Emission Zone Shifts in OLEDs at high Currents and Correlation with Charge Balance Factor”, Jeju Island, South Korea

